DISSERTATION

Neutron Stars In Numerical Relativity

Author:
Swami Vivekanandji Chaurasia
(M.Sc.)

Supervisor:
Prof. Dr. Bernd Brügmann

A dissertation submitted in fulfillment of the requirements
for the degree of Doctor rerum naturalium (Dr. rer. nat.)

in the

Numerical Relativity Group
Faculty of Physics and Astronomy
Friedrich-Schiller Universität Jena

REVIEWERS:

1.	PROF. DR. BERND BRÜGMANN	(FRIEDRICH-SCHILLER-UNIVERSITÄT JENA)
2.	DR. FRANK OHME	(ALBERT-EINSTEIN-INSTITUT HANNOVER)
3.	PROF. DR. KONSTANTINOS KOKKOTAS	(UNIVERSITÄT TÜBINGEN)

DEFENSE DATE: 09.06.2020

॥ ॐ ॥
को अध्दा वैद क इह प्र वौचत्कुत आजोता कुते इयं विसृएष्टिः ।
अर्वाग्देवा अस्य विसर्जनेनाथा को वैद यते आबभूवे ॥

"But, after all, who knows, and who can say
whence it all came, and how creation happened?
the gods themselves are later than creation,
so who knows truly whence it has emerged?"

इयं विसृएष्टिर्यते आबभूव यदिए वा दधे यदिए वा न ।
यो अस्याध्येक्षः परमे व्यौमन्सो अड्न्गा वैद यदिए वा न वेदे ॥

"Whence all creation had its origin,
he, whether he fashioned it or whether he did not,
he, who surveys it all from highest heaven,
he knows - or maybe even he does not know."

नासदीय सूक्त (ऋग्वेद)

Nasadiya Sukta (Rigveda)

FRIEDRICH-SCHILLER UNIVERSITÄT JENA

Abstract

Faculty of Physics and Astronomy
Institute for Theoretical Physics

Doctor rerum naturalium (Dr. rer. nat.)

Neutron Stars In Numerical Relativity

by Swami Vivekanandji Chaurasia (M.Sc.)

Binary neutron star coalescence lead to extremely violent merger events in the universe. Such events give rise to a variety of observable phenomena in both the gravitational and the electromagnetic channels. In this thesis we study such extreme events in the last milliseconds around the merger. Gravity and its coupling to other physics for such systems is described by Einstein's theory of general relativity. Since these are highly nonlinear coupled set of partial differential equations, no analytical solutions exist for generic and dynamical systems such as binary neutron stars in the strong-field regime. Therefore, the usage of numerical methods is inevitable.

In this thesis we consider configurations of binary neutron stars with varying equation of state, spin, eccentricity and spin orientation. In particular we present the first numerical relativity simulations of highly eccentric binary neutron stars in full (3+1)D using consistent initial data, i.e., setups which are in agreement with the Einstein equations and with the equations of general relativistic hydrodynamics in equilibrium. Additionally, we also study precessing binary neutron star systems using full (3+1)D numerical relativity simulations with consistent initial data.

Further, we investigate a new numerical approach for solving the equations of general relativistic hydrodynamics using the discontinuous Galerkin method. It combines the key aspects of finite volume and traditional finite element methods, for e.g., element locality and $hp-$adaptivity besides the benefit of spectral convergence for smooth solutions. Discontinuous Galerkin methods ease the treatment of complex grid geometries and, allow simple and efficient parallelization.

Contents

Abstract **v**

1 Introduction **1**

2 General Relativity on a Computer **7**

2.1 Numerical Relativity 7

2.1.1 3+1 decomposition: Geometry 9

2.1.2 3+1 decomposition: Einstein's equations 11

2.1.3 The BSSN scheme 13

2.1.4 Conformal Thin Sandwich decomposition 15

2.2 General Relativistic Hydrodynamics 16

3 Numerical Methods **23**

3.1 Method of Lines 23

3.2 Finite-Difference Method 24

3.3 Spectral Element Methods 26

3.4 Conservation Law Discretization 30

3.5 Recovering Primitive Variables 34

3.6 Spectral Expansions & Discontinuities 36

4 Highly Eccentric Binary Neutron Stars **39**

4.1 Initial Data 39

4.2 Evolutions 43

4.3 Dynamics 45

4.4 Gravitational Waves 54

4.5 f-mode Oscillations 57

4.6 Convergence Study 66

5 Precessing Binary Neutron Stars **69**

5.1 Precessing Configurations & Evolution 69

5.2 Orbital Motion & Gravitational Waves 71
5.3 Energetics 75
5.4 Ejecta 78

6 Discontinuous Galerkin Method for GRHD 81
6.1 Flat Spacetime Tests 82
6.2 Isolated Star in Cowling Approximation 89

7 Conclusions 95

A Simulation Analysis 99

B Radiated Energy and Angular Momentum in GWs 107

Bibliography 109

Publications 127

Acknowledgements 129

Additional Material 131

Abbreviations and Notation

Throughout this work geometrized units are employed with $c = G = M_\odot = 1$. In some cases, c, G, $M_\odot$ are given explicitly for better understanding. These units correlate to physical units of time, length, mass and mass density as follows:

$$\Delta t = 1 \equiv 4.9266 \;\; \mu\,\mathrm{s}, \quad \mathrm{m} = 1 \equiv 1.9889 \times 10^{30} \;\; \mathrm{kg}$$
$$\Delta s = 1 \equiv 1.4769 \;\; \mathrm{km}, \quad \rho = 1 \equiv 6.1733 \times 10^{17} \;\; \mathrm{g} \;\; \mathrm{cm}^{-3}$$

We use *greek* letters for four-dimensional indices running from 0 to 3 and *latin* letters for three-dimensional indices running from 1 to 3. The following abbreviations are used throughout the thesis, these abbreviations are also introduced in the text at their first appearance:

ADM	**A**rnowitt **D**eser **M**isner
BAM	**B**i-functional **A**daptive **M**esh (code)
BBH	**B**inary **B**lack **H**ole
BH	**B**lack **H**ole
BNS	**B**inary **N**eutron **S**tar
BSSN	**B**aumgarte-**S**hapiro-**S**hibata-**N**akamura
CFL	**C**ourant-**F**riedrichs-**L**ewy
CRV	**C**onstant **R**otational **V**elocity
CTS	**C**onformal **T**hin-**S**andwich
DG	**D**iscontinuous **G**alerkin
EM	**E**lectro**M**agnetic
EOS	**E**quation **o**f **S**tate
GR	**G**eneral **R**elativity
GRHD	**G**eneral **R**elativistic **H**ydro**D**ynamics
GW	**G**ravitational **W**ave
HMNS	**H**yper**M**assive **N**eutron **S**tar
HRSC	**H**igh **R**esolution **S**hock **C**apturing
ID	**I**nitial **D**ata
LHS	**L**eft **H**and **S**ide
LLF	**L**ocal **L**ax-**F**riedrichs
MNS	**M**assive **N**eutron **S**tar
NR	**N**umerical **R**elativity
NS	**N**eutron **S**tar
PDE	**P**artial **D**ifferential **E**quation
PN	**P**ost-**N**ewtonian

PSD	**P**ower **S**pectral **D**ensity
RHS	**R**ight **H**and **S**ide
RK	**R**unge-**K**utta
TOV	**T**olman-**O**ppenheimer-**V**olkoff
WENO	**W**eighted **E**ssentially **N**on-**O**scillatory

Chapter 1

Introduction

Neutron stars (NS) and astrophysical black holes (BH) are compact objects that are one of the extreme manifestations of matter in the universe known to us. Even our Galaxy has a population estimate of a few hundred million neutron stars and probably a few hundred thousand black holes (Camenzind, 2007). Owing to the richness of phenomena related to compact objects, the topic has attracted attention from a wide range of researchers from the fields of astronomy and astrophysics, nuclear and particle physics, theoretical physics and last but not the least, condensed matter physics. Black holes had been proposed as early as the eighteenth century (Montgomery et al., 2009) and were only later obtained as a mathematical solution to Einstein's gravity in the early twentieth century by Schwarzschild (1916). Neutron stars were also proposed in the early twentieth century by Baade et al. (1934). Hewish et al. (1968) made the first detection of a Pulsar which however was identified as a pulsating neutron star and in less than a decade later Cygnus X-1 was proposed by Shipman (1975) to be a black hole candidate. Ever since then, there has been widespread interest in studying these compact objects.

Neutron stars composed of baryon matter are conjectured to exhibit conditions not reproducible on earthbound laboratories and show many phenomena not observed elsewhere, for e.g., the neutron star core is expected to have densities in excess of the nuclear density, contain deconfined quark matter, show superfluidity and superconductivity with critical temperatures near 10^{10} kelvin, opaqueness to neutrinos, and magnetic fields larger than 10^{13} Gauss. Apart from the extreme physics in the interior, they are also extremely gravitating objects next only to black holes. Their surface gravity is $\sim$ hundred billion times that of Earth's gravity. Black holes on the other hand, devoid of any surrounding matter or accretion disks, are classically purely gravitational objects. The very source of the gravitational field of black holes is a physical curvature singularity which is hidden behind a horizon, a surface from which even light cannot escape. Gravity of compact objects, unlike typical stellar objects describable by Newtonian gravity, relies on the concepts of space and time as described by Einstein (1915) in his famous general theory of relativity.

As a consequence of the extreme properties of compact objects, close interactions among themselves for e.g., a binary of compact objects with one or all the components being neutron stars or black holes is an equivalently extreme scenario. Those extreme interactions lead to the phenomena of gravitational and electromagnetic radiation (Andersson et al., 2011; Baker et al., 2006; Eichler et al., 1989; Rosswog, 2015).

The spectacular observation of both gravitational waves (GWs) and electromagnetic (EM) radiation from a binary neutron star (BNS) merger in August 2017, GW170817 (Abbott et al., 2017c,b; Abbott et al., 2017f), the very recent BNS detection event GW190425 (Abbott et al., 2020) (for which no EM counterpart has been detected), and several detections of GWs from binary black hole (BBH) mergers (Abbott et al., 2019) starting 2015 have initiated the era of multi-messenger and gravitational wave astronomy. The EM signatures from GW170817 showed promising evidence that short gamma-ray bursts (sGRBs) originate from BNS mergers (Abbott et al., 2017b) and also provided evidence that these mergers are the most likely places where heavy elements ($A \gtrsim 140$) are produced from r-process nucleosynthesis that takes place in the matter ejected during the BNS merger. Further, the radioactive decay from the products of the r-process are expected to power transients called the kilonova or macronova (Metzger, 2017; Rosswog, 2013).

With the planned upgrades of the advanced GW detectors LIGO, VIRGO, the recently operational KAGRA detector in Japan and the upcoming IndIGO detector in India, the near future of GW astronomy is bright and multiple detections of compact binaries are expected in the coming years (Abbott et al., 2018; Abbott et al., 2016b). In addition to those improvements, the possibility of a 3$^{\text{rd}}$ generation (3G) of GW detectors, such as the Einstein Telescope (ET) (Ballmer et al., 2015; Hild et al., 2008; Punturo et al., 2010) and the Cosmic Explorer (Abbott et al., 2017e), is exciting, since 3G detectors are expected to be ten times more sensitive than currently operating detectors. 3G observatories would thus not only provide a significantly larger number of detections, but also give the possibility of detecting systems and signals not observable by current interferometers, e.g., the postmerger phase of the remnant formed after the collision of NSs (Abbott et al., 2017d; Clark et al., 2016;

Radice et al., 2017), highly eccentric BNS systems and precessing BNS systems.

In anticipation of an increased number of BNS detections with higher signal-to-noise ratio and the possibility to detect extreme configurations such as precessing BNSs, highly eccentric systems, or high-mass ratio mergers, it becomes even more important to theoretically model compact binary waveforms accurately to allow for a precise measurement of the source parameters. In order to extract information from a measured GW signal, the data are compared with fast-to-evaluate waveform models, which need to cover the entire BNS parameter space to allow for the accurate estimation of the binary parameters for all possible systems.

Over years after the publication of Einstein's general theory of relativity, our theoretical understanding of compact objects have been greatly advanced and refined. These improvements have been possible due to a deeper understanding of the mathematical structure of Einstein's gravity and its coupling to other topics like hydrodynamics and electromagnetism, to name a few. The refined understanding has also led to approximation methods for Einstein equations for e.g., the post-Newtonian (PN) formalism (Blanchet, 2006), gravitational self-force (GSF) formalism (Barack et al., 2003) and the effective one body (EOB) formalism (Buonanno et al., 1999). These approximations allow one to compute gravitational waveforms (i.e., gravitational radiation) from different compact object binaries in the perturbative regime. To understand the dynamics happening in the non-perturbative regime i.e. the strong-field case where the approximation methods are no longer valid, the Einstein equations have to be solved completely i.e., without any weak-field assumptions albeit with discretized form of the equations with additional assumptions for the matter models.

In the very recent decade one method to solve the Einstein's equations, in particular, in the strong-field scenario has emerged popular. This method is based on solving the equations via numerical methods on large scale computers and is known as numerical relativity (NR). Numerical relativity enables the description of compact object mergers and the extraction of important information about it, which otherwise would not be possible. The field picked momentum after the first successful evolution of inspiralling and merging binary black holes, allowing the extraction of gravitational signal and was performed by Pretorius (2005). Interestingly, the investigations of the first fully general relativistic simulations of BNSs had already been started by Shibata (1999) and followed in their subsequent works (Shibata et al., 2000).

Developing infrastructure to perform numerical relativity simulations is an involved task, and requires care to perform successful simulations in a finite amount of time. Einstein's equations have to be recast in a form suitable for numerically stable evolutions. The numerical methods selected to solve the discretized equations must ensure stability, accuracy and efficiency. Additional methods are devised to analyze the simulation data. Since the computational resources required in performing a fully general relativistic simulation in three spatial dimensions is large as compared to conventional computational requirements, the numerical methods must be efficiently parallelized to use large scale computing infrastructures.

Having developed such a stable, accurate and efficient infrastructure for performing long-term numerical simulations, these codes show their true power in shedding light on the dynamics and kinematics of compact object mergers. One such merger that has recently gained attention is a system of BNSs on highly eccentric orbits that are anticipated to be in the detection range of 3$^{\text{rd}}$ generation GW detectors such as the Einstein Telescope and Cosmic Explorer. In NR, most groups have focused on the simulations of quasi-circular BNS systems. This restriction is reasonable since the vast majority of systems are expected to have only a small eccentricity once the system enters the LIGO band due to the decay of eccentricity by the emission of gravitational radiation (Kowalska et al., 2011; Peters, 1964). However, different channels have been suggested for the formation of NS binaries that may retain non-negligible eccentricity when they merge, see details for formation channels and rates, and detection rates in (Chaurasia et al., 2018) and references therein.

As eccentric BNSs merge, they may produce brighter EM emission than quasi-circular mergers, making it important to understand such systems from a multi-messenger perspective. Furthermore, the gravitational waveforms for highly eccentric binaries significantly differ from the classical chirp signal of quasi-circular inspirals with its slowly increasing amplitude and frequency. On highly eccentric orbits, each encounter of the stars leads to a burst of GW radiation. An important result concerning BNS (or BHNS) is that eccentricity leads to tidal interactions that can excite oscillations of the stars, which in turn generate their own characteristic GW signal (Chirenti et al., 2017; Turner, 1977; Yang et al., 2018). Neither the orbital nor stellar GWs have been studied so far for eccentric BNS orbits in general relativity (GR) with consistent initial data (ID), i.e., data which fulfill the Einstein constraint equations and the equations of general relativistic hydrodynamics (GRHD) in equilibrium.

Another promising merger scenario that will be of importance especially for the 3^{rd} generation GW detectors is a system of precessing BNSs. These are systems where the individual NS spin direction is misaligned with respect to the orbital angular momentum direction of the BNS system. Such a spin misaligned system can lead to a precessing or a 'wobbling' motion of the entire orbital plane. In addition to the precession of the orbital plane the individual spins of the stars are expected to show nutation or precession of the spins.

Pulsar observations of BNS systems suggest that most NSs have small spins (Kiziltan et al., 2013; Lattimer, 2012), however, this conclusion is based on a small selected set of observed binaries. Observations of isolated NSs or NSs in binary systems other than BNSs show that NSs can rotate fast, e.g., PSR J1807−2500B has a rotation frequency of 239Hz (Lattimer, 2012; Lorimer, 2008). Similar to the uncertainty in the spin magnitude, the orientation of spins in BNS systems is also highly uncertain and unknown. Misaligned spins can be caused by kicks created during the supernova explosions of the progenitor stars. A possible realignment of the spin caused by accretion is only likely for the more massive NS and not for the secondary star, e.g., PSRJ0737-3039B has a spin misaligned with the orbital angular momentum by $\approx 130^\circ$ (Farr et al., 2011). In addition, for BNS systems formed due to dynamical capture, there will be no reason to have aligned spins. Consequently, detailed studies of the effect of spin precession are required.

For many scenarios numerical simulations provide inputs to tune the analytical models (Ajith et al., 2011; Taracchini et al., 2014) and therefore efficient and accurate general relativistic simulations will play an important role for future gravitational wave astronomy. Since the beginning of the first fully general relativistic simulations of BNS mergers (Shibata, 1999) different numerical codes for GRHD simulations have been developed (Baiotti et al., 2003; Font et al., 2000; Liu et al., 2008; Radice et al., 2012; Thierfelder et al., 2011; Yamamoto et al., 2008). These codes are based on finite volume or finite difference methods and are parallelized by domain decomposition and distribution of grids using shared memory−message passing interface (MPI). The amount of communication needed in such methods increase with the increase in the formal order of the scheme. This limits the efficiency and accuracy of such methods as a balance has to be found between the accuracy and efficiency in the production codes.

In order to tackle these issues, spectral element methods have gained interest in the modern numerical relativity codes (Hilditch et al., 2016; Kidder et al., 2000; Kidder et al., 2017; Tichy, 2006). They have shown to be impressively efficient and high order for the simulations of vacuum spacetimes, e.g. gravitational wave collapse or binary black hole systems. However, such methods show spectral convergence to the true solution only for smooth solutions. For systems that can contain discontinuities or shocks in the solutions, e.g. GRHD system of equations, spectral methods drop in accuracy. This is one reason why production codes investigating NSs still rely on finite volume or finite difference methods for the treatment of hydrodynamical fields. In principle, therefore, using high-order spectral methods to obtain accurate solutions to partial differential equations (PDEs) that can contain discontinuities seems less appealing, it nonetheless is important to understand how such methods apply to those systems, such as the astrophysical scenarios arising in numerical relativity simulations of NSs.

In this thesis work we perform numerical investigations of binary neutron star mergers in full GR using the fully general relativistic finite difference `BAM` code and perform preliminary tests with the `bamps` code in the spirit of developing improved numerical methods for GRHD simulations using spectral element methods. The thesis is organized as follows: In Chapter 2 we review the 3+1 formulation of GR that is useful in obtaining the geometric and matter equations that will be numerically solved. Chapter 3 briefly describes the numerical methods that enable the stable, accurate and efficient numerical evolutions of the geometric and the matter equations. In Chapter 4 we present the results from the first consistent simulations of highly eccentric BNS mergers. Chapter 5 is dedicated to the results from the simulations of precessing BNS systems. Chapter 6 presents the results from the investigations of using discontinuous Galerkin (DG) methods in solving the general relativistic hydrodynamics equations. Finally Chapter 7 concludes the thesis. Additional information is added in Appendices A & B where we include important details for the analysis of our simulations.

Chapter 2

General Relativity on a Computer

The Einstein field equation written out compactly in the covariant form, Eq. (2.1), is the cornerstone of modern cosmology, the physics of neutron stars and black holes, the generation of gravitational radiation, and many more cosmic phenomena where strong-field gravitation plays a dominant role. Its applicability to a wide variety of phenomena occurring in the universe is impeccable. It has passed many tests in the weak-field regime in the past (Asmodelle, 2017) and has only very recently undergone the strong-field test after the first direct detection of the BBH merger GW150914 (Abbott et al., 2016a) in 2015.

$$G_{\mu\nu} = R_{\mu\nu} - \frac{1}{2} R \, g_{\mu\nu} = 8\pi \, T_{\mu\nu} \tag{2.1}$$

In order to solve the Einstein's equations numerically, they need to be recast in a form suitable for using the machinery of solving PDEs numerically. In Sec. 2.1 of this chapter we describe in brief the important equations for numerical relativity simulations. Here we do not discuss the underlying principles of Einstein's general theory of relativity and refer the reader to the excellent textbooks of Misner et al. (1973), Schutz (1985), and Wald (1984). In Sec. 2.2 we describe the equations for general relativistic hydrodynamics as used in the numerical simulations of neutron star mergers.

2.1 Numerical Relativity

Solving Eq. (2.1) means to compute the metric of the spacetime ($g_{\mu\nu}$) given the matter-energy distribution encoded in the energy-momentum tensor ($T_{\mu\nu}$). Additionally, to determine the matter motion in GR, the equations of GRHD are also required to be solved in conjunction with the field equations. This is not a necessary step for BBH spacetimes as the energy-momentum tensor is identically zero. A preliminary step in solving Eq. (2.1) is to cast them in the popular language of PDEs. In literature a few analytic solutions to Eq. (2.1) exist within a high degree of symmetry assumptions (Stephani et al., 2003).

In order to obtain solutions to generic and dynamical settings, for example, the two body problem in GR in the strong-field regime for which no analytic solution exists, the solution has to be obtained numerically. In the following we briefly unwrap the field equation in *3+1 form*, that will be apt for adapting numerical methods to obtain solutions using a computer. In 3+1 form the spacetime manifold (a four-dimensional manifold) is foliated by three-dimensional spacelike hypersurfaces, see e.g. (Alcubierre, 2008; Baumgarte et al., 2010; Gourgoulhon, 2012; Rezzolla et al., 2013) for detailed textbook explanations.

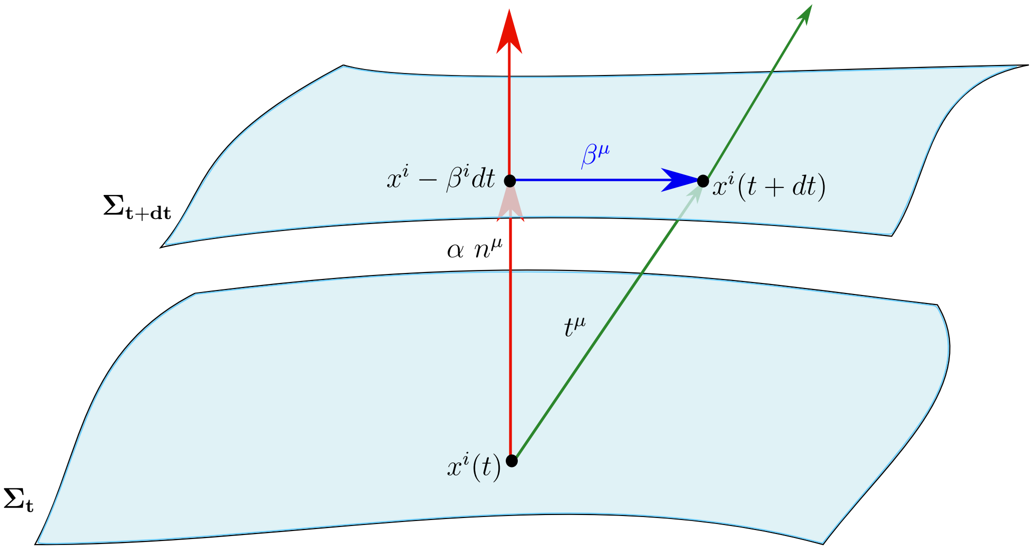

FIGURE 2.1: Schematic of the foliation of the four-dimensional manifold $\mathcal{M}$ by three-dimensional hypersurfaces Σ. On each hypersurface we introduce coordinates x^i. The four-vector t^μ represents the direction of evolution of the time coordinate t and can be split into a timelike component $\alpha \boldsymbol{n}$, where $\boldsymbol{n}$ is a timelike unit normal to the hypersurface, and into spacelike component $\boldsymbol{\beta}$. The lapse α measures the proper time between the adjacent hypersurfaces and the shift β^μ determines the change of the coordinates from Σ_t to Σ_{t+dt}.

2.1.1 3+1 decomposition: Geometry

A spacetime manifold $\mathcal{M}$ is globally hyperbolic i.e., there exists a Cauchy surface Σ such that its topology is necessarily $\Sigma \times \mathbb{R}$ (Gourgoulhon, 2012). Owing to this property it is possible to foliate the four-dimensional spacetime $(\mathcal{M}, g_{\mu\nu})$, where $g_{\mu\nu}$ is the metric on $\mathcal{M}$[1], by three-dimensional hypersurfaces if there exists a smooth and regular scalar field t on $\mathcal{M}$ with a non-zero gradient such that every level surface is a hypersurface Σ_t, cf. Fig. 2.1. The field t can be interpreted as the coordinate time on the hypersurface $\Sigma_t = \Sigma(t)$. The normalized co-vector orthogonal to Σ_t is given by

$$n_\mu = -\alpha \nabla_\mu t. \tag{2.2}$$

From the normalization condition of timelike vectors, one gets $\alpha^2 = -1/g^{tt}$. We restrict $\alpha > 0$ to ensure that n^μ is future directed[2]. The proportionality constant α is typically called the *lapse* function (Wheeler, 1964). Since n^μ is a normalized timelike vector, it can be understood as the four-velocity field of a family of observers i.e., the *Eulerian* observers. Moreover, locally Σ_t can be seen as the set of simultaneous events for this observer (Gourgoulhon, 2012). With the help of the normal vector n^μ, the induced metric on the hypersurface Σ_t is constructed as,

$$\gamma_{\mu\nu} = g_{\mu\nu} + n_\mu n_\nu \tag{2.3}$$

and the corresponding inverse is obtained by raising the indices of $\gamma_{\mu\nu}$ with $g^{\alpha\beta}$,

$$\gamma^{\mu\nu} = g^{\mu\nu} + n^\mu n^\nu. \tag{2.4}$$

Furthermore, to characterize the embedding of the hypersurface Σ in $\mathcal{M}$ the *extrinsic* curvature is defined as,

$$K_{\mu\nu} = -P^\sigma{}_\mu \, \nabla_\sigma n_\nu, \tag{2.5}$$

where $P^\mu{}_\nu = \delta^\mu{}_\nu + n^\mu n_\nu$ is the spatial projection operator projecting the gradient of the normal (co-) vector into the spatial slice Σ_t. In general, all tensors can be split in a purely spatial part i.e., contained completely in Σ_t by the spatial projection operator $P^\mu{}_\nu$ and a purely timelike part orthogonal to Σ_t by the normal projection operator ${N^{\mu}}_{\nu} = -n^{\mu} n_{\nu}$. Likewise, using Eq. (2.3), the metric compatibility condition $\nabla_{\gamma} g_{\mu\nu} = 0$ and $n_{\mu} \nabla_{\nu} n^{\mu} = 0$, it can be shown that,

---

[1] In this thesis we set the signature of the metric to be +2.

[2] Using Taylor expansion it can be shown that n^μ points in a direction of increasing t (since $\alpha > 0$).

$$K_{\mu\nu} = -\frac{1}{2} \mathcal{L}_{\boldsymbol{n}} \gamma_{\mu\nu}, \tag{2.6}$$

where $\mathcal{L}_{\boldsymbol{n}}$ denotes the Lie-derivative along the vector field $\boldsymbol{n}$. The above relation indicates that $K_{\mu\nu}$ encodes information about the temporal change of the induced metric.

Following Fig. 2.1, the coordinates x^i of Σ_t can be generalized to $x^{\mu} = (t, x^i)$ i.e., uplifted to a coordinate system on $\mathcal{M}$. At each point x^{μ} the difference between t^{μ} and αn^{μ} is defined as the shift vector β^{μ} (blue vector in Fig. 2.1) and is tangential to the slice at x^{μ}. Consequently, all the introduced vectors get related by the basic relation,

$$t^{\mu} = \alpha n^{\mu} + \beta^{\mu}. \tag{2.7}$$

Choosing a basis adapted to the coordinates x^{μ} such that $t^{\mu} \equiv (1, 0, 0, 0)$, the normal vector and co-vector are expressed in this basis as functions of the shift β^{μ} and the lapse α as

$$n^{\mu} = \left(\frac{1}{\alpha}, -\frac{\beta^i}{\alpha} \right), \tag{2.8}$$

$$n_{\mu} = (-\alpha, 0, 0, 0)\,. \tag{2.9}$$

Note, since β^{μ} is tangent to Σ_t, $\beta^{\mu} \equiv (0, \beta^i)$. In general, all zeroth components of spatial contravariant and covariant tensors vanish. Lastly, inserting equation (2.9) in (2.3) leads to the four-dimensional line element in 3+1 form:

$$ds^2 = (-\alpha^2 + \beta_i \beta^i)\, dt^2 + 2\beta_i\, dt\, dx^i + \gamma_{ij}\, dx^i\, dx^j. \tag{2.10}$$

In the remainder of this chapter we will use the 3+1 geometric decomposition introduced in this subsection to obtain the 3+1 form of the Einstein's field equations and the equations for general relativistic hydrodynamics.

2.1.2 3+1 decomposition: Einstein's equations

ADM equations

Einstein's equations (2.1) relate the contractions of the four-dimensional Riemann tensor ${}^{(4)}R^{\alpha}{}_{\beta\gamma\delta}$ to the energy-momentum tensor. Since we want to relate four-dimensional objects to their three-dimensional counterparts, in this subsection we start by considering the ADM formalism (Arnowitt et al., 2008) to split the field equations (2.1) in 3+1 form ending up with a system of evolution and constraint equations much like the Maxwell's equations of electrodynamics.

Starting with the relatively straightforward right hand side (RHS) of Einstein's field equations, the energy-momentum tensor is expressed in the 3+1 form with the following projections,

$$S_{\mu\nu} = P^{\sigma}{}_{\mu} P^{\rho}{}_{\nu} T_{\sigma\rho}, \tag{2.11a}$$

$$S_{\mu} = -P^{\sigma}{}_{\mu} n^{\rho} T_{\sigma\rho}, \tag{2.11b}$$

$$E = n^{\mu} n^{\nu} T_{\mu\nu}, \tag{2.11c}$$

where $S_{\mu\nu}$ is the spatial part of $T_{\mu\nu}$, S_{μ} is the momentum density, and E the energy density as measured by the Eulerian or the normal observer with the four-velocity n^{ν}.

Constraint equations

For the left hand side (LHS) of Einstein's equations, we will require the split of the Riemann tensor based on the Gauss-Codazzi Eq. (2.12a) and the Codazzi-Mainardi Eq. (2.12b),

$$P^{\delta}{}_{\alpha} P^{\kappa}{}_{\beta} P^{\lambda}{}_{\mu} P^{\sigma}{}_{\nu} \, {}^{(4)}R_{\delta\kappa\lambda\sigma} = {}^{(3)}R_{\alpha\beta\mu\nu} + K_{\alpha\mu} K_{\beta\nu} - K_{\alpha\nu} K_{\beta\mu}, \tag{2.12a}$$

$$P^{\delta}{}_{\alpha} P^{\kappa}{}_{\beta} P^{\lambda}{}_{\mu} n^{\sigma} \, {}^{(4)}R_{\delta\kappa\lambda\sigma} = D_{\beta} K_{\alpha\mu} - D_{\alpha} K_{\beta\mu}, \tag{2.12b}$$

where ${}^{(3)}R_{\alpha\beta\gamma\delta}$ is the three-dimensional Riemann tensor and D_{α} is the uniquely defined three-dimensional covariant derivative compatible with the three-metric $\gamma_{\mu\nu}$. From the contracted Gauss relation, which follows from Eq. (2.12a), and the energy-momentum contractions introduced above, we obtain,

$$\gamma^{\alpha\gamma} \gamma^{\beta\delta} \, {}^{(4)}R_{\alpha\beta\gamma\delta} = {}^{(3)}R + K^2 - K_{\alpha\beta} K^{\alpha\beta} = 2 n^{\alpha} n^{\beta} G_{\alpha\beta} = 16\pi E, \tag{2.13}$$

and contracting Eq. (2.12b) we get

$$\gamma^{\alpha\mu} n^{\nu}\, {}^{(4)}R_{\mu\nu} = D^{\alpha} K - D_{\mu} K^{\alpha\mu} = \gamma^{\alpha\mu} n^{\nu} G_{\mu\nu} = -8\pi S^{\alpha}. \tag{2.14}$$

The four equations,

$$\begin{aligned} {}^{(3)}R + K^2 - K_{\alpha\beta} K^{\alpha\beta} &= 16\pi E, \\ D_j K^{ij} - D^i K &= 8\pi S^i, \end{aligned} \tag{2.15}$$

are called the *Hamiltonian* and the *Momentum Constraints*, respectively. These equations have to be fulfilled for all time slices. Therefore, they will also be required to be solved to construct the initial data that describe the initial state of the physical system we will be interested in studying.

Evolution equations

To obtain the evolution equation for the induced metric,

$$\partial_t \gamma_{ij} = -2\alpha K_{ij} + D_i \beta_j + D_j \beta_i, \tag{2.16}$$

we recall the definition of the extrinsic curvature Eq. (2.5) and its equivalent form Eq. (2.6),

$$K_{\alpha\beta} = -\frac{1}{2} \mathcal{L}_{\mathbf{n}} \gamma_{\alpha\beta} = -\frac{1}{2\alpha} \left(\mathcal{L}_{\mathbf{t}} - \mathcal{L}_{\boldsymbol{\beta}} \right) \gamma_{\alpha\beta} = -\frac{1}{2\alpha} \left(\partial_t \gamma_{\alpha\beta} - D_{\alpha} \beta_{\beta} - D_{\beta} \beta_{\alpha} \right). \tag{2.17}$$

Noting again that all zeroth components vanish for the spatial tensors, we obtain (2.16).

On the other hand, the evolution equation for the extrinsic curvature,

$$\begin{aligned} \partial_t K_{ij} = &- D_i D_j \alpha + \beta^k D_k K_{ij} + K_{ik} D_j \beta^k + K_{kj} D_i \beta^k \\ &+ \alpha \left({}^{(3)}R_{ij} + K K_{ij} - 2 K_{ik} K^k{}_j \right) + 4\pi\alpha \left(\gamma_{ij} (S - E) - 2 S_{ij} \right), \end{aligned} \tag{2.18}$$

can be derived by contracting the Riemann tensor twice with the normal vector and using Eq. (2.12a), which will yield

$$P^{\mu}{}_{\alpha}P^{\nu}{}_{\beta}n^{\rho}n^{\sigma}\,{}^{(4)}R_{\mu\rho\nu\sigma} = \mathcal{L}_{\mathbf{n}}K_{\alpha\beta} + \frac{1}{\alpha}D_{\alpha}D_{\beta}\alpha + K^{\lambda}{}_{\beta}K_{\alpha\lambda}, \tag{2.19}$$

$$P^{\mu}{}_{\alpha}P^{\nu}{}_{\beta}\left(n^{\rho}n^{\lambda}\,{}^{(4)}R_{\mu\rho\nu\lambda} + {}^{(4)}R_{\mu\nu}\right) = {}^{(3)}R_{\alpha\beta} + KK_{\alpha\beta} - K^{\lambda}{}_{\beta}K_{\alpha\lambda}. \tag{2.20}$$

Finally, inserting Eq. (2.19) in Eq. (2.20) we get,

$$\mathcal{L}_{\mathbf{n}}K_{\alpha\beta} = -\frac{1}{\alpha}D_{\alpha}D_{\beta}\alpha - P^{\mu}{}_{\alpha}P^{\nu}{}_{\beta}\,{}^{(4)}R_{\mu\nu} + {}^{(3)}R_{\alpha\beta} + KK_{\alpha\beta} - 2K^{\lambda}{}_{\beta}K_{\alpha\lambda}, \tag{2.21}$$

which can be transformed to the evolution equations (2.18) with further reductions.

The equations (2.15,2.16,2.18) are called the ADM-equations named after Arnowitt, Deser, and Misner. The actual representation used in this thesis and in the numerical relativity community, was derived by York (1979), as it is better suited for numerical simulations than the original ADM approach.

2.1.3 The BSSN scheme

The BSSN approach and also the initial data construction at their foundation follow the philosophy of separating the radiative degrees of freedom from the nonradiative ones. The ADM equations presented so far combined with common slicing conditions[3] are, unfortunately, only weakly hyperbolic (Kidder et al., 2001). Therefore, they will not possess the necessary well-posedness and requirement for long term numerical simulations. To counter this, in 1987 Nakamura, Oohara and Kojima (Nakamura et al., 1987) reformulated the ADM equations that led to a more stable evolution scheme. Later, Baumgarte, Shapiro (Baumgarte et al., 1998) and Shibata, Nakamura (Shibata et al., 1995) improved this formulation in 1998. This new, numerically stable, evolution system has become the NR workhorse for many years now and is called the BSSNOK or just the BSSN formulation.

In the following, we write-down the particular formulation of the BSSN equations as used in the `BAM` code.

---

[3] Slicing condition defines the particular foliation of the spacetime. Choosing the right condition is crucial for a successful numerical simulation, cf. (Bona et al., 1995).

Constraint equations:- As a starting step, we consider a conformal rescaling of the spatial metric,

$$\bar{\gamma}_{ij} = \psi^{-4}\gamma_{ij}. \tag{2.22}$$

Here ψ is the conformal function (a scalar function). Further, since the number of degrees of freedom must remain the same, one is allowed to impose $\bar{\gamma} = 1$ or equivalently $\psi = (\det(\gamma))^{\frac{1}{12}}$. The extrinsic curvature K_{ij} is moreover split in a trace-free part A_{ij} and the trace K as

$$K_{ij} = A_{ij} + \frac{1}{3}\gamma_{ij}K. \tag{2.23}$$

The trace-free (or the traceless) part is additionally rescaled conformally as,

$$\bar{A}_{ij} = \psi^{2}A_{ij}. \tag{2.24}$$

Equations (2.22) - (2.24) now applied on the constraint equations give,

$$\begin{aligned} \bar{D}^i\bar{D}_i\psi - \frac{1}{12}\psi^5K^2 + \frac{1}{8}\psi^{-7}\bar{A}_{ij}\bar{A}^{ij} - \frac{1}{8}\psi\,{}^{(3)}\bar{R} &= -2\pi\psi^5E, \\ \bar{D}_j\bar{A}^{ij} - \frac{2}{3}\psi^6\bar{\gamma}^{ij}\bar{D}_jK &= 8\pi\psi^{10}S^i. \end{aligned} \tag{2.25}$$

We find that the operator in the Hamiltonian constraint has a Laplacian on the left-hand-side. In the following subsection, we will further modify the Momentum constraint equation in order to obtain elliptic form of the equations that are solved to obtain initial data for the evolution system. This additional modification will follow the *Conformal Thin Sandwich* (CTS) decomposition to obtain the elliptic equations.

Evolution equations:- For the evolution equations we use $\tilde{A}_{ij} = \psi^{-6}\bar{A}_{ij}$, $\tilde{\gamma}_{ij} = \bar{\gamma}_{ij}$, the conformal connection functions defined as,

$$\tilde{\Gamma}^i \equiv \tilde{\gamma}^{jk}\tilde{\Gamma}^i{}_{jk} = -\partial_j\tilde{\gamma}^{ij}, \tag{2.26}$$

where the last equality holds in Cartesian coordinates when $\tilde{\gamma} = 1$ and the conformal factor $\chi = \psi^{-4}$. For the conformal factor we obtain

$$\left(\partial_t - \mathcal{L}_\beta\right)\chi = \frac{2}{3}\chi\left(\alpha K - D_i\beta^i\right). \tag{2.27}$$

For obtaining the other evolution equations we use the ADM equations determined in the previous subsection and add multiples of the constraint equations i.e.,

$$\left(\partial_t - \mathcal{L}_\beta\right)\tilde{\gamma}_{ij} = -2\alpha\tilde{A}_{ij}, \tag{2.28a}$$

$$\left(\partial_t - \mathcal{L}_\beta\right)\tilde{A}_{ij} = \chi\left(-D_iD_j\alpha + \alpha\,{}^{(3)}R_{ij} - 8\pi\alpha S_{ij}\right)^{\mathrm{TF}} + \alpha\left(K\tilde{A}_{ij} - 2\tilde{A}_{ik}\tilde{A}^k_j\right), \tag{2.28b}$$

$$\left(\partial_t - \mathcal{L}_\beta\right)K = -D^iD_i\alpha + \alpha\left(\tilde{A}_{ij}\tilde{A}^{ij} + \frac{1}{3}K^2\right) + 4\pi\alpha(E+S), \tag{2.28c}$$

$$\begin{aligned}\partial_t\tilde{\Gamma}^i &= \tilde{\gamma}^{jk}\partial_j\partial_k\beta^i + \frac{1}{3}\tilde{\gamma}^{ij}\partial_j\partial_k\beta^k - 2\tilde{A}^{ij}\partial_j\alpha + \beta^j\partial_j\tilde{\Gamma}^i + \frac{2}{3}\tilde{\Gamma}^i\partial_j\beta^j \\ &\quad - \tilde{\Gamma}^j\partial_j\beta^i + 2\alpha\left(\tilde{\Gamma}^i{}_{jk}\tilde{A}^{jk} - \frac{3}{2}\tilde{A}^{ij}\partial_j\ln(\chi) - \frac{2}{3}\tilde{\gamma}^{ij}\partial_jK - 8\pi\tilde{\gamma}^{ij}S_j\right).\end{aligned} \tag{2.28d}$$

Here 'TF' indicates the trace-free part. Notice that $\tilde{\Gamma}^i$ are treated as an independent function that satisfy their own evolution equations and the definition of Eq. (2.26) serves as an additional constraint equation.

2.1.4 Conformal Thin Sandwich decomposition

Since the constraint equations (2.25) are specified only on a single hypersurface, nothing can be said about the gauge variables α and β^i. A very frequent issue arising due to this is the ambiguity in choosing the freely specifiable data and its influence on the resulting physical solutions. To circumvent this issue , the CTS decomposition was proposed in (Wilson et al., 1995, 1996; York Jr., 1999). Here we only sketch the modifications to the constrain equations (2.25) that gives the equations required to be solved to obtain quasi-equilibrium initial data.

As a first step, the conformal traceless part of the extrinsic curvature $\bar{A}_{ij}$ is written in terms of the shift β^i,

$$\bar{A}^{ij} = -\frac{\psi^6}{2\alpha}\left(\bar{u}^{ij} - (\bar{L}\beta)^{ij}\right), \tag{2.29}$$

where $\bar{u}^{ij} := \partial_t\bar{\gamma}_{ij}$, $\bar{\gamma}^{ij}\bar{u}_{ij} = 0$ and $(\bar{L}\beta)^{ij} = \bar{D}^i\beta^j + \bar{D}^j\beta^i - \frac{2}{3}\delta^{ij}\bar{D}_k\beta^k$ ($\bar{L}$ is the vector gradient operator). Using this in the Momentum constraint equation of (2.25), we get,

$$(\bar{\Delta}_L\beta)^i - (\bar{L}\beta)^{ij}\bar{D}_j \ln(\alpha\psi^{-6}) = \alpha\psi^{-6}\bar{D}_j\left(\frac{\bar{u}^{ij}\psi^6}{\alpha}\right) + \frac{4}{3}\alpha\bar{D}^iK + 16\pi\alpha\psi^4S^i, \tag{2.30}$$

where $\bar{\Delta}_L$ denotes the vector Laplacian.

Though, all the necessary ingredients are there to construct a solution of the initial value problem for the given background data, it nevertheless would be useful to have more freedom in choosing the metric $\bar{\gamma}_{ij}$ and the mean curvature K, as well as their time derivatives. This was again proposed by York Jr. (1999) and is known as the *extended conformal thin sandwich* (XCTS) decomposition. This requires the consideration of an additional equation,

$$\begin{aligned}\bar{D}^i\bar{D}_i(\alpha\psi) =& \alpha\psi\left(\frac{7}{8}\psi^{-8}\bar{A}_{ij}\bar{A}^{ij} + \frac{5}{12}\psi^4K^2 + \frac{1}{8}\,{}^{(3)}\bar{R} + 2\pi\psi^4(E+2S)\right)\\ &- \psi^5\partial_tK + \psi^5\beta^i\bar{D}_iK,\end{aligned} \tag{2.31}$$

which is a combination of the once contracted evolution equation for the extrinsic curvature (2.18) and the Hamiltonian constraint. Therefore, now we need to solve five instead of four equations, but we are allowed to choose $\bar{\gamma}_{ij}$, $\bar{u}^{ij}$, K and ∂_tK freely. Furthermore, for spacetimes containing matter, in order to obtain initial data which are also in hydrodynamical equilibrium i.e., overall a *consistent* set of initial data, we have to solve the derived constraint equations together with the matter equations as will be described in Sec. 4.1.

2.2 General Relativistic Hydrodynamics

In this section we will describe the equations of motion for matter fields in general relativity. The schemes so far derived are mostly applicable for understanding the kinematics and dynamics of the spacetime geometry. For the purpose of writing the matter motion equations in 3+1 form we follow the "Valencia formulation" of relativistic hydrodynamics; see (Banyuls et al., 1997; Font, 2007; Rezzolla et al., 2013; Shibata, 2016) for references and detailed explanations. The fundamental equations governing the matter fields arise from the energy-momentum conservation law,

$$\nabla_\nu T^{\mu\nu} = 0, \tag{2.32}$$

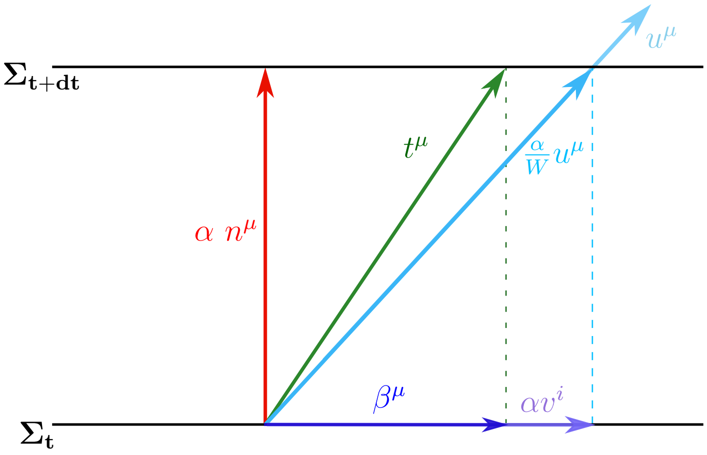

FIGURE 2.2: 3+1 decomposition of the fluid four-velocity field u^μ into its spatial projection as the three-velocity field v^i are illustrated. Additionally, already introduced 3+1 quantities are shown for clarity.

and the conservation of the rest-mass,

$$\nabla_\mu j^\mu = 0. \tag{2.33}$$

Moreover, the energy-momentum tensor of a perfect fluid and the rest-mass four-current are assumed respectively as,

$$T^{\mu\nu} = \rho\, h\, u^\mu u^\nu + p\, g^{\mu\nu}, \tag{2.34}$$

$$j^\mu = \rho u^\mu. \tag{2.35}$$

Here u^μ is the fluid four-velocity field, ρ is the fluid rest-mass density, p is the pressure, $h = 1 + \epsilon + \frac{p}{\rho}$ is the specific enthalpy of the fluid and ϵ is the specific internal energy.

As illustrated in Fig. 2.2, u^μ can be scaled by a factor $\frac{\alpha}{W}$, $W = -u^\mu n_\mu$, such that it maps points from Σ_t to Σ_{t+dt}. By comparing the proper times elapsing for the Eulerian observer $-\delta\tau^2 = g_{\mu\nu}(\alpha n^\mu dt)(\alpha n^\nu dt)$ and the Lagrangian observer i.e., an observer moving with the fluid, $-\delta\tau_0^2 = g_{\mu\nu}(\frac{\alpha}{W}u^\mu dt)(\frac{\alpha}{W}u^\nu dt)$ in between the two slices Σ_t and Σ_{t+dt}, one finds

$$\delta\tau = W\delta\tau_0 = \alpha dt. \tag{2.36}$$

Owing to this relation, W is called the Lorentz factor in reference to special relativity. Consequently, it also explains the name of the lapse as α relates the lapse of proper time measured by the Eulerian observer and the coordinate time difference dt. It can also be seen from Fig. 2.2, that the fluid displacement relative to this observer is given by the projection $P^{\mu}{}_{\nu}\frac{\alpha}{W}u^{\nu}dt$. The observer dependent three-velocity of the fluid v^{μ} is given by this displacement divided by the elapsed proper time, so that by means of (2.36),

$$v^{\mu} = P^{\mu}{}_{\nu}\frac{1}{W}u^{\nu}. \tag{2.37}$$

Starting with the 3+1 decomposition of the fluid four-velocity, see Fig. 2.2, it can be written as,

$$u^{\mu} = W\left(n^{\mu} + v^{\mu}\right). \tag{2.38}$$

where $W = 1/\sqrt{1-\gamma_{kl}v^k v^l}$ is the same Lorentz factor as previously defined. This enables us to reformulate the rest-mass conservation law (2.33) using the projection relations and the 3+1 definitions from subsection 2.1.1,

$$\begin{aligned}\alpha\nabla_{\mu}j^{\mu} &= \alpha\left(P^{\nu}{}_{\mu} - n_{\mu}n^{\nu}\right)\nabla_{\nu}\left(\rho W\left(n^{\mu}+v^{\mu}\right)\right)\\ &= \partial_t\left(\rho W\right) + D_i\left(\rho W\left[\alpha v^i - \beta^i\right]\right) + \rho W\left(D_i\beta^i - \alpha K\right) = 0.\end{aligned} \tag{2.39}$$

Note that though this is already in 3+1 decomposed version of the equation, it will be more insightful to re-write it such that its conservation properties are apparent again. With $\partial_t\gamma_{ij} = \mathcal{L}_{\mathbf{t}}\gamma_{ij}$ and (2.6) we can write,

$$D_i\beta^i - \alpha K = \frac{1}{2}\gamma^{ij}\partial_t\gamma_{ij}. \tag{2.40}$$

Additionally, the following two standard relations can be derived by expanding the determinant and expanding the 3-Covariant derivative 'D' in terms of the 3-Christoffel symbol i.e.,

$$\frac{1}{\sqrt{\gamma}}\partial_t\sqrt{\gamma} = \frac{1}{2}\gamma^{ij}\partial_t\gamma_{ij}, \tag{2.41}$$

$$D_i v^i = \partial_i v^i + \frac{1}{2}v^i\gamma^{kl}\partial_i\gamma_{kl} = \frac{1}{\sqrt{\gamma}}\partial_i\left(\sqrt{\gamma}v^i\right). \tag{2.42}$$

With the help of these relations in (2.39) we obtain its conservation law form,

$$\partial_t\left(\sqrt{\gamma}\rho W\right) + \partial_i\left(\sqrt{\gamma}\rho W\left[\alpha v^i - \beta^i\right]\right) = \alpha\sqrt{\gamma}\nabla_\mu j^\mu = 0. \tag{2.43}$$

Similarly, we can 3+1 decompose the energy-momentum conservation equation (2.32). For this we express Eqs. (2.11a–2.11c) in terms of the perfect fluid energy-momentum tensor (2.34) which gives,

$$\begin{aligned} S_{\mu\nu} &= P^\alpha{}_\mu P^\beta{}_\nu T_{\alpha\beta} = \rho h W^2 v_\mu v_\nu + p\gamma_{\mu\nu}, \\ S_\mu &= -P^\alpha{}_\mu n^\beta T_{\alpha\beta} = \rho h W^2 v_\mu, \\ E &= n^\mu n^\nu T_{\mu\nu} = \rho h W^2 - p. \end{aligned} \tag{2.44}$$

Further, one can express the energy-momentum tensor in terms of these decompositions as,

$$T_{\mu\nu} = E n_\mu n_\nu + S_\mu n_\nu + n_\mu S_\nu + S_{\mu\nu}. \tag{2.45}$$

As already mentioned, S_μ, $S_{\mu\nu}$, and E are the momentum density, the the stress tensor and the energy density as measured by the Eulerian observer, respectively. Following Banyuls et al. (1997), we introduce the *primitive* variables as $\mathbf{w} = \{\rho, v_i, \epsilon\}$ (the proper rest-mass density, the fluid velocity, and the internal energy density measured by a Lagrangian observer) and the corresponding *conservative* variables $\mathbf{q} = \{D, S_i, E\}$ (the conserved rest-mass, momentum, and internal energy density measure by the Eulerian observer):

$$\begin{aligned} D &= \rho W, \\ S_i &= \rho h W^2 v_i, \\ E &= \rho h W^2 - p, \\ \tau &= E - D, \end{aligned} \tag{2.46}$$

Note that for evolution purpose, instead of E we use τ as a conserved variable similar to Banyuls et al. (1997).

The free index in Eq. (2.32) can now be projected along and orthogonal to Σ_t. The former projection leads to momentum conservation, whereas the latter results in energy conservation. Projecting onto Σ_t and using again the projection relations from subsection 2.1.1 and Eqs. (2.44)–(2.45) gives,

$$\alpha P^{\nu}{}_{i} \nabla_{\mu} T^{\mu}{}_{\nu} = \partial_t S_i + D_j \left(\alpha S^j{}_i - S_i \beta^j \right) + S_i \left(D_j \beta^j - \alpha K \right) - S_j D_i \beta^j + E D_i \alpha = 0. \tag{2.47}$$

Similar to the decomposition of the rest-mass conservation law, using again Eq. (2.40) and the standard relation (after expanding the 3-Covariant derivative 'D' in terms of the 3-Christoffel symbol),

$$D_j S^j{}_i = \partial_j S^j{}_i + \frac{1}{\sqrt{\gamma}} \partial_j \sqrt{\gamma} S^j{}_i - \Gamma^k{}_{ij} S^j{}_k, \tag{2.48}$$

we find find the balance law result for momentum conservation,

$$\alpha \sqrt{\gamma} P^{\nu}{}_{i} \nabla_{\mu} T^{\mu}{}_{\nu} = \partial_t \left(\sqrt{\gamma} S_i \right) + \partial_j \left(\sqrt{\gamma} \left[\alpha S^j{}_i - S_i \beta^j \right] \right) - \frac{1}{2} S^{jk} \partial_i \gamma_{jk} - S_j \partial_i \beta^j + E \partial_i \alpha = 0. \tag{2.49}$$

Lastly, projecting Eq. (2.32) onto n^{μ} and with the same tricks as before, we obtain,

$$\alpha \sqrt{\gamma} n^{\nu} \nabla_{\mu} T^{\mu}{}_{\nu} = \partial_t \left(\sqrt{\gamma} E \right) + \partial_i \left(\sqrt{\gamma} \left[\alpha S^i - E \beta^i \right] \right) + \sqrt{\gamma} S^i \partial_i \alpha + \alpha \sqrt{\gamma} S^{ij} K_{ij} = 0. \tag{2.50}$$

Overall, we obtained a system of five equations (2.43), (2.49), (2.50) for the matter variables in GRHD. Though not included in this thesis work, additional equations will arise when magnetic fields and micro-physics are included in the model.

We can summarize the system of equations so far obtained for GRHD as a fundamental balance law as in Banyuls et al. (1997). The first-order, flux conservative, hyperbolic system written in terms of the conserved variables is,

$$\frac{1}{\sqrt{-g}} \left(\frac{\partial (\sqrt{\gamma}\, \mathbf{q})}{\partial x^0} + \frac{\partial (\sqrt{-g}\, \mathbf{F}^i)}{\partial x^i} \right) = \mathbf{S}, \tag{2.51}$$

where

$$
\begin{aligned}
\mathbf{q} &= \mathbf{q}(\mathbf{w}) \equiv \{D, S_i, \tau\} \\
\mathbf{F}^i &= \mathbf{F}^i(\mathbf{w}) \equiv \left\{ D\left(v^i - \frac{\beta^i}{\alpha}\right), S_j\left(v^i - \frac{\beta^i}{\alpha}\right) + p\delta^i_j, \tau\left(v^i - \frac{\beta^i}{\alpha}\right) + pv^i \right\} \\
\mathbf{S} &= \mathbf{S}(\mathbf{w}) \equiv \left\{ 0, T^{\mu\nu}\left(\partial_\mu g_{\nu j} - {\Gamma^\sigma}_{\nu\mu} g_{\sigma j}\right), \alpha\left(T^{\mu 0}\partial_\mu(\ln\alpha) - T^{\mu\nu}{\Gamma^0}_{\nu\mu}\right) \right\}.
\end{aligned}
\tag{2.52}
$$

Since these are hyperbolic equations, the dynamics of the corresponding quasi-linear system can be decomposed in advective transport processes with characteristic speeds. These provide very useful information, e.g. the maximum propagation speed of the fields along a given direction. These information will later be used to construct numerical fluxes for our numerical schemes, see Sec. 3.4. The characteristic speeds are the eigenvalues of the matrix $\frac{\partial(s_i F^i)}{\partial q}$ where the vector s^i specifies the direction of propagation. These eigenvalues are given by Banyuls et al. (1997) and are,

$$
\begin{aligned}
\lambda_0 &= \alpha s_i v^i - s_i \beta^i \quad \text{(triple)}, \\
\lambda_\pm &= \frac{\alpha}{1 - v^2 c_s^2}\left[s_i v^i (1 - c_s^2) \pm c_s \sqrt{(1 - v^2)[s^2(1 - v^2 c_s^2) - (s_i v^i)^2 (1 - c_s^2)]} \right] - s_i \beta^i.
\end{aligned}
\tag{2.53}
$$

Here, c_s denotes the speed of sound defined by $c_s^2 = \left(\frac{\partial p}{\partial \rho} + \frac{p}{\rho^2}\frac{\partial p}{\partial \epsilon}\right)$. The first set of speeds in (2.53) corresponds to matter waves whereas the second set corresponds to the speed of acoustic waves.

It is insightful to see that upon integrating equation (2.51) over a certain spatial volume $\mathcal{V}$, the average of $\mathbf{q}$ in $\mathcal{V}$ changes in time only due to inflow-outflow through $\partial\mathcal{V}$ and due to sources and sinks in $\mathcal{V}$. Although $\mathbf{q}$ is only conserved if $\mathbf{S} = 0$, the components of $\mathbf{q}$ are usually called conserved variables. As already described earlier, the conserved variables are expressed in terms of the primitive variables, see Eq. (2.46). Since there is no analytic inversion of this mapping, the primitives are usually recovered by a Newton-Raphson root-finding procedure as will be discussed in Sec. 3.5.

Equation of State

One last piece is still missing that would close the system of GRHD evolution equations so far obtained, and that encodes very important information about the microscopic nature of the matter model is the equation of state (EOS). The EOS used is of the form $p = P(\rho, \epsilon)$ and we use one among the following possibilities for different parts in this thesis,

$$\text{(i) polytropic EOS} \qquad P(\rho) = \kappa \rho^{\Gamma}, \tag{2.54a}$$

$$\text{(ii) ideal gas} \qquad P(\rho, \epsilon) = (\Gamma - 1)\rho\epsilon, \tag{2.54b}$$

$$\text{(iii) piecewise-polytropic EOS} \qquad P(\rho) = \kappa_i \rho^{\Gamma_i},\ \rho \in (\rho_i, \rho_{i+1}) \tag{2.54c}$$

$$\begin{aligned} \text{(iv) piecewise-polytropic EOS} \qquad & P(\rho) = \kappa_i \rho^{\Gamma_i} \\ \text{+ thermal contribution} \qquad & \qquad + (\Gamma_{th} - 1)\rho\epsilon_{th},\ \rho \in (\rho_i, \rho_{i+1}). \end{aligned} \tag{2.54d}$$

Here $\epsilon_{th} = \epsilon - \epsilon_{cold}$ and ϵ_{cold} is computed from the barotropic (polytropic) EOS. As outlined by Read et al. (2009a), many barotropic zero-temperature EOSs developed to describe neutron star matter, can be fitted with piecewise-polytropes. Additionally, it is possible to extend the barotropic EOSs with an additional thermal pressure (Bauswein et al., 2010; Shibata et al., 2005).

Chapter 3

Numerical Methods

In the previous chapter we obtained the well-posed[1] equations for the spacetime variables and the matter variables in general relativity. In order for the discretized form of those equations to yield a unique and a convergent solution, the numerical methods employed to solve the PDEs must be consistent[2]. In this chapter an overview of the numerical methods employed in this thesis is presented . In particular we will focus on the different spatial discretization methods as implemented in the two codes, `BAM` (Sec. 3.2) and `bamps` (Sec. 3.3), used in this thesis. In Sec. 3.4 a derivation of the balance law form of the DG GRHD scheme is presented. Section 3.5 will briefly describe the method adopted for transforming the conservative to primitive variables and finally we will conclude this chapter with Sec. 3.6 where a brief discussion about the influence of discontinuities on spectral methods is presented.

3.1 Method of Lines

The evolution equations presented in Sec. 2.1 together with the equation of motion for the matter fields in Sec. 2.2 describe a nonlinear system of hyperbolic PDEs. In this thesis, we follow the method-of-lines approach such that time and space can be treated separately to solve the PDE system. As a starting point to this approach, the spatial dimensions are discretized while the time dimension is still continuous. The RHS, which contains spatial derivatives of the evolved variables (by writing the system of equations such that only temporal-derivative term is on the LHS), can be evaluated in different ways. In this thesis, we used finite differencing scheme as implemented in `BAM` and employed spectral methods a.k.a discontinuous Galerkin method for GRHD part in `bamps`[3]. Once the spatial dimensions are discretized we obtain a set of ordinary differential equations at each grid point viz. the semi-discrete equations. The obtained semi-discrete system can be solved with any stable ordinary differential equation solver. In this thesis we use an explicit third and fourth order Runge-Kutta (RK) method and an appropriate Courant-Friedrichs-Lewy (CFL) condition is employed for stable and accurate numerical evolutions.

---

[1] Note that it is also required that the differential operator is not ill-conditioned, meaning, a small error in the initial data should not result in much larger errors in the solutions.

[2] An approximation is consistent if, $\lim_{\Delta t,h\to 0} ||L(u) - L_{\Delta t,h}(u)|| = 0$, here L and $L_{\Delta t,h}$ represent the differential operator in the continuum limit and the discretized versions, respectively.

3.2 Finite-Difference Method

A relatively straightforward and much celebrated approach computing numerical derivatives is the usage of finite differencing stencil on an uniform grid, cf. (Sundqvist et al., 1970) for a non-uniform grid example. `BAM` follows this approach for the discretization of the RHS i.e., the discretization of the spatial derivatives and in essence is a finite difference code.

In the discretized domain, considering that at every grid point x_j any function $f(x)$ can be expressed as a Taylor series,

$$f(x) = f(x_j) + (x - x_j)f'(x_j) + \frac{(x - x_j)^2}{2} f''(x_j) + \mathcal{O}[(x - x_j)^3], \tag{3.1}$$

where $'$ denotes the first order spatial derivative, $''$ denotes the second order spatial derivative and so on. In order to evaluate the derivative $f'(x_j)$, we use the Taylor expansions, as in Eq. (3.1), at the neighboring grid points x_{j-1}, x_{j+1}. Thereafter combining the resulting two equations we come up with a simple second order approximation to $f'(x)$ at $x = x_j$,

$$f'(x_j) = \frac{f(x_{j+1}) - f(x_{j-1})}{x_{j+1} - x_{j-1}} + \mathcal{O}[(x_{j+1} - x_{j-1})^2]. \tag{3.2}$$

Similarly, higher order approximations with smaller truncation errors and higher degree derivative stencils can be derived using the information of more grid points,

---

[3] Note that in `bamps`, the spacetime evolution equations are written in the generalized harmonic gauge (GHG) formulation and pseudospectral methods are used for its numerical evolution, cf. (Hilditch et al., 2016).

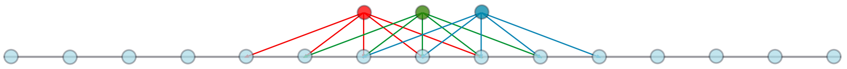

(a.) Uniform finite difference grid

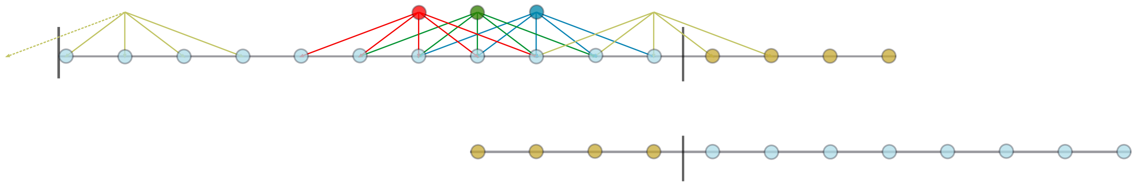

(b.) Grid distributed on different processors

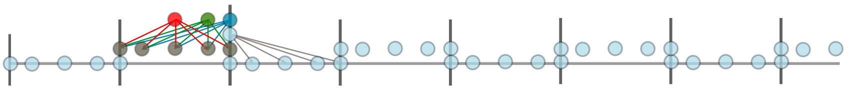

(c.) Spectral element grid

FIGURE 3.1: Schematic of the domain decomposition for the finite difference scheme, Figs. (a,b) and spectral element method, Fig. (c). In Fig. (b), the ‘`yellow`’ circles mark the (buffer) region that is required to be communicated (in a parallel code) from the neighboring processor in order to compute the finite difference approximation on each processor. Communication size for such a scheme increases with the increase in the formal order of the scheme and the dimensionality of the PDE being approximated. For spectral element methods an integer number of elements are distributed across each processor. Therefore, only the boundary data on each processor is required to be communicated. This is the glory of spectral methods viz., exceptionally high-order and highly scalable schemes, see (Hilditch et al., 2016, Fig. 9) for a strong scaling test in the context of NR, although without matter fields, for the `bamps` code.

see Fig. 3.1. In the current `BAM` version finite differencing stencils of up to tenth-order for the geometrical variables and fourth-order for the matter variables are implemented, see (Thierfelder et al., 2011) and references therein. Such an approach for the spatial discretization has been the workhorse in the numerical relativity community and in general for solving PDEs.

Though being very robust in their application to solving a variety of PDEs, the bottleneck of such methods is their scaling on large compute clusters. As the order of the finite difference stencils is increased, the number of neighboring grid data required increases. This increases the amount of information needed to be communicated in parallel codes such as used for numerical relativity evolutions, see

Fig. 3.1. Owing importantly to this bottleneck, there is a considerable effort in transitioning from finite difference methods to spectral element methods as they can be formulated as local schemes that are anticipated to be better scalable than the finite difference schemes. Spectral element methods combine the geometric flexibility of finite elements and the exceptional accuracy of spectral methods.

3.3 Spectral Element Methods

In a relatively recent progress in solving the Einstein's equations numerically there is a widespread interest in using an alternate approach for the discretization of the spatial derivatives based on *spectral element methods* due to their superior accuracy and scaling properties, see (Bugner et al., 2016; Grandclément et al., 2009; Haas et al., 2016; Hilditch et al., 2016; Szilagyi et al., 2009). Spectral or hp element methods give geometric flexibility of the classical $h-$type finite element schemes in addition to the desirable numerical properties of spectral methods, employing high-degree piecewise polynomial basis functions on coarse finite element type meshes.

In the following, we construct the spectral discretization scheme for hyperbolic PDEs that are applicable to the type of evolution equations that we obtained in chapter 2.

Polynomial spectral methods or spectral methods e.g., Pseudospectral, Galerkin, Tau, are based on the same underlying principle (Hesthaven et al., 2007; Kopriva, 2009) i.e., given a PDE system of the form,

$$\partial_t u = Lu, \tag{3.3}$$

where L is a differential operator acting on the coordinates ξ, the solution is approximated as a series expansion in orthogonal polynomials ϕ_i,

$$u(\xi, t) \approx u_n(\xi, t) = \sum_{k=0}^{N} a_k(t)\phi_k(\xi). \tag{3.4}$$

For numerical purposes the infinite series is truncated within finite terms. This is the so called *modal* form of the expansion since the fundamental unknowns are the coefficients of the orthogonal expansion functions or modes. However, note that later it will be useful to represent the modal form of the polynomials as a Lagrange or Newton form interpolant through a set of grid points or node values and this would be called the *nodal* expansion. Furthermore, the residual defined as

$$R_n = \partial_t u_n - L u_n, \tag{3.5}$$

should vanish in the continuum limit. The specific numerical implementation of this condition for R_n is what differentiates between different spectral methods.

Pseudospectral Methods

For the case of a pseudospectral method, the residual (i.e., the strong form) is enforced to vanish exactly at certain points in the domain,

$$\partial_t u_n(\xi_i, t) = L u_n(\xi_i, t), \tag{3.6}$$

where ξ_i are the so called collocation points or nodes. Additionally, to evaluate integrals and retain the essential properties of spectral methods, namely orthogonality and spectral accuracy, the quadrature nodes are chosen appropriately. In `bamps` as used in this thesis, the $N+1$ nodes are given by the Legendre-Gauss-Lobatto (LGL) nodes,

$$\xi_i \in \left\{ \xi \mid (1-\xi^2) \frac{dP_N}{d\xi}(\xi) = 0 \right\}, \tag{3.7}$$

where P_N is the N^{th}-degree Legendre polynomial. Note that the lower index in ξ_i enumerates the nodes and the upper index in ξ^i represents a coordinate index, and the notation should not to be confused. Using these nodes in each dimension spans the cubic interval $[-1,1] \times [-1,1] \times [-1,1]$, which is the fundamental reference grid in `bamps`. From this reference grid, the `bamps` grid is built in global Cartesian coordinates $x^{\underline{i}} \equiv (x, y, z)$, see (Hilditch et al., 2016, Fig. 1) for more details.

Galerkin Methods

Contrary to the pseudospectral method, the residual is enforced in a different way in a Galerkin method. Instead of enforcing the residual R_n to vanish at the nodes, cf. Eq. (3.6), its projection on the space of approximating polynomials is set to zero,

$$\int_{\mathcal{V}} \left[\partial_t u_n(\xi, t) - L u_n(\xi, t)\right] \, \phi_i(\xi) \, d\xi = 0. \tag{3.8}$$

Moreover, $N+1$ collocation points are used in one-dimension to construct equations for the $N+1$ degrees of freedom. It is also to be noted that (3.8) approximates the weak form of the original PDE where ϕ_i is a rather general test function. Further, it is natural to choose the approximation space and therefore also the test function space to be polynomials or at least continuous functions in $\mathcal{V}$. This is the starting of classical finite element or continuous Galerkin methods. However, this ansatz breaks the locality of the scheme i.e., if the domain is subdivided into elements, numerical operators will act globally and not element-wise. This would clearly be a disadvantage regarding domain decomposition and scalable parallelization of the algorithm which is one of the most sought after aspect, apart from high-order accuracy, of the numerical relativity codes.

Discontinuous Galerkin Method

To tackle the disadvantages with the classical finite element methods, in a discontinuous Galerkin method a local scheme is constructed by relaxing the constraints on the test and the basis functions by accepting discontinuities at element interfaces, cf. Fig. 3.1. Consequently, we consider ϕ_i to be piecewise polynomial on $\mathcal{V}$. Although, this increases the degrees of freedom as we now have multiple values at each element boundary but we obtain element local numerical operators and a scheme which is easy to parallelize in principle, see Fig. 3.1. However, connecting the elements that was enforced by the continuity of the basis functions in the classical finite element method now needs special care in a DG method as will be discussed later in this chapter.

Spatial derivatives

To construct a numerical scheme from (3.6) or (3.8) in order to find the coefficients of the solution expansion (3.4), an approximation for the spatial derivatives of $u(t,x)$ (the solution) is required. This can be derived simply by exploiting the properties of the *Lagrange* polynomials,

$$\ell_k(\xi) = \prod_{\substack{l=0 \\ l\neq k}}^{N} \frac{\xi - \xi_l}{\xi_k - \xi_l}. \tag{3.9}$$

As already noted earlier, instead of using the modal form (3.4) of the orthogonal polynomial ϕ_i's, the Lagrange form of the polynomials are used in the expansion (3.4), i.e. $\phi_k = \ell_k$. At each node ξ_i , a corresponding Lagrange polynomial ℓ_i is defined with the properties $\ell_i(\xi_i) = 1$ and $\ell_i(\xi_j) = 0$ for $i \neq j$. This simply implies that the expansion coefficients a_k in (3.4) are identical with the values at the nodes i.e.,

$$u_n(\xi, t) = \sum_{k=0}^{N} u_n(\xi_k, t)\ell_k(\xi). \tag{3.10}$$

Consequently, to find the derivate of (3.10) one only needs the derivate of ℓ_k since the operator only acts on the Lagrange polynomials,

$$D_{ik} := \frac{\partial \ell_k}{\partial \xi}(\xi_i) = \begin{cases} \sum_{\substack{m=0 \\ m\neq i}} (\xi_i - \xi_m)^{-1}, & \text{for } i = k \\ \left(\prod_{\substack{j=0 \\ j\neq k}}^{N} (\xi_k - \xi_j) \right)^{-1} \prod_{\substack{m=0 \\ m\neq k \\ m\neq i}}^{N} (\xi_i - \xi_m), & \text{for } i \neq k. \end{cases} \tag{3.11}$$

Here D_{ik} is a derivative matrix that maps function values of the approximation at the nodes to its spatial derivative at the same nodes[4] i.e.,

$$\frac{\partial u_n}{\partial \xi}(\xi_i) = \sum_{k=0}^{N} u_n(\xi_k, t)\frac{\partial \ell_k}{\partial \xi}(\xi_i) = \sum_{k=0}^{N} D_{ik} u_n(\xi_k, t). \tag{3.12}$$

Therefore, the numerical differentiation of a function is only a matrix multiplication in a DG method and this can be performed by well maintained and efficient libraries such as BLAS and LAPACK. To obtain the derivatives in the multidimensional case, the derivative matrix is applied to each direction i.e.,

$$\frac{\partial u_n}{\partial \xi^3}(\xi_i^1, \xi_j^2, \xi_k^3, t) = \sum_{l=0}^{N} D_{kl} u_n(\xi_i^1, \xi_j^2, \xi_l^3, t), \tag{3.13}$$

for derivatives with respect to ξ^3.

In `bamps`, the computational domain is divided into grid or elements, E. Each element is a simple linear mapping of the fundamental reference grid, B. Moreover, piecewise polynomials are chosen as basis functions on the reference grid,

---

[4] Note that instead of using D_{ii} from (3.11), it is constructed as negative sum of the off-diagonal elements (Kopriva, 2006) such that the derivative of a constant function is numerically exactly zero.

$$\phi_{k_1}(\xi^1)\phi_{k_2}(\xi^2)\phi_{k_3}(\xi^3) \equiv \phi_k(\xi^1,\xi^2,\xi^3) = \ell_{k_1}(\xi^1)\ell_{k_2}(\xi^2)\ell_{k_3}(\xi^3), \tag{3.14}$$

where $k \equiv (k_1, k_2, k_3)$ is a notation index. Furthermore, the pseudospectral scheme as well as the DG scheme will finally map the nodal values of the solution to its time derivative because of this choice of basis polynomials. Therefore, the method employed for solving the GRHD equations (2.51−2.52), is categorized as a nodal DG scheme. Moreover, in `bamps` the collocation points chosen for the pseudospectral scheme for solving the GHG form of the field equations are also the collocation points for the DG scheme. Hence, interpolation between different sets of quadrature nodes is not necessary.

3.4 Conservation Law Discretization

In the following we derive the DG scheme for the balance law (or conservation law), cf. Eqs. (2.51−2.52). Starting from,

$$\partial_t u + \partial_{\underline{i}} f^{\underline{i}}(u) = s(u), \tag{3.15}$$

and integrating element-wise against the test functions for a weak formulation, we obtain,

$$\partial_t \int_E \phi_k u \, d^3x + \int_E \phi_k \partial_{\underline{i}} f^{\underline{i}} \, d^3x = \int_E \phi_k s \, d^3x. \tag{3.16}$$

In order to evaluate the integrals using quadratures in the above, a transformation to the reference grid (B) is needed,

$$\partial_t \int_B \phi_k \; u \; \det J \, d^3\xi + \int_B \phi_k \; \partial_j((J^{-1})^j{}_{\underline{i}} f^{\underline{i}} \det J) \, d^3\xi = \int_B \phi_k \; s \; \det J \, d^3\xi. \tag{3.17}$$

The Jacobian (J) here corresponds to the transformation from the reference grid to the Cartesian grids. Due to the choice of the curvilinear grid layout (which is static) of `bamps`, the Jacobian is not a simple rescaling of Cartesian grids, see (Hilditch et al., 2016, Fig. 1). Additionally, we use the *metric identities* of Kopriva (2006), where $\partial_j((J^{-1})^j{}_{\underline{i}} \det J) = 0$, to obtain the form of the flux term in the above equation.

Discretizing integrals

In order to evaluate the integrals in (3.17), all spatial variables are expanded in terms of the polynomial basis $\phi_l = \ell_{l_1}\ell_{l_2}\ell_{l_3}$,

$$\begin{aligned}\partial_t \int_B \phi_k\, u\, \det J\, d^3\xi &\approx \partial_t (u\, \det J)^l_n \int_B \phi_k \phi_l\, d^3\xi \\ &= \partial_t (u\, \det J)^{l_1 l_2 l_3}_n M_{l_1 k_1} M_{l_2 k_2} M_{l_3 k_3}, \end{aligned} \tag{3.18}$$

where the *mass matrix* is defined as,

$$M_{ab} = \int_{-1}^{1} \ell_a(\xi)\, \ell_b(\xi)\, d\xi. \tag{3.19}$$

Similarly, the source integral in (3.17) is expanded,

$$\int_B \phi_k\, s\, \det J\, d^3\xi \approx (s\, \det J)^{l_1 l_2 l_3}_n M_{l_1 k_1} M_{l_2 k_2} M_{l_3 k_3}. \tag{3.20}$$

Note that here the product of the solution u and the Jacobian determinant is expanded rather than expanding only u and computing the integral including the analytic Jacobian determinant. Going the other way round would make the mass matrix element dependent, whereas currently a single mass matrix is valid for all elements with the same order of approximation.

Finally, we consider the integral of the flux term in (3.17) which requires special care in its evaluation. Expanding the flux term along the surface normal co-vector in the j-direction defined as $s^j_{\underline{i}} = (J^{-1})^j_{\underline{i}} \det J$ and evaluating the integral by parts in each direction we can write,

$$\begin{aligned}\int_B \phi_k\, \partial_j((J^{-1})^j{}_{\underline{i}} f^{\underline{i}} \det J)\, d^3\xi &= \iiint_{-1}^{1} \phi_{k_1}\phi_{k_2}\phi_{k_3} \left(\partial_1(s^1_{\underline{i}} f^{\underline{i}}) + \partial_2(s^2_{\underline{i}} f^{\underline{i}}) + \partial_3(s^3_{\underline{i}} f^{\underline{i}})\right) d\xi^1 d\xi^2 d\xi^3 \\ &= \iint_{-1}^{1} \left(\left[\phi_{k_1} s^1_{\underline{i}} f^{\underline{i}}\right]_{-1}^{1} - \int_{-1}^{1} s^1_{\underline{i}} f^{\underline{i}}\, \partial_1 \phi_{k_1}\, d\xi^1 \right) \phi_{k_2}\phi_{k_3} d\xi^2 d\xi^3 + \\ &\quad \iint_{-1}^{1} \left(\left[\phi_{k_2} s^2_{\underline{i}} f^{\underline{i}}\right]_{-1}^{1} - \int_{-1}^{1} s^2_{\underline{i}} f^{\underline{i}}\, \partial_2 \phi_{k_2}\, d\xi^2 \right) \phi_{k_1}\phi_{k_3} d\xi^1 d\xi^3 + \\ &\quad \iint_{-1}^{1} \left(\left[\phi_{k_3} s^3_{\underline{i}} f^{\underline{i}}\right]_{-1}^{1} - \int_{-1}^{1} s^3_{\underline{i}} f^{\underline{i}}\, \partial_3 \phi_{k_3}\, d\xi^3 \right) \phi_{k_1}\phi_{k_2} d\xi^1 d\xi^2. \end{aligned} \tag{3.21}$$

The first terms in the integration by parts in each direction produces surface integrals over the elements boundary surface. These boundary integrals will allow us to exchange information to the neighboring elements thereby providing a natural way to connect the sub-domains and is a key aspect of DG methods.

The remaining integrals in (3.21) are again approximated following the expansion of spatial variables i.e., $s^{j}_{\underline{i}} f^{\underline{i}} \approx (s^{j}_{\underline{i}} f^{\underline{i}})^{l}_{n} \phi_l$ ('n' represents that it is a numerical approximation). With this expansion, the final expressions for our DG scheme is obtained, representing the flux term of the balance law,

$$
\begin{aligned}
&\int_B \phi_k \, \partial_j((J^{-1})^{j}{}_{\underline{i}} f^{\underline{i}} \det J) \, d^3\xi \\
\approx &\left(\left[\delta_{k_1 N} (s^{1}_{\underline{i}} f^{*\underline{i}})^{N l_2 l_3}_{n} - \delta_{k_1 0} (s^{1}_{\underline{i}} f^{*\underline{i}})^{0 l_2 l_3}_{n} \right] - (s^{1}_{\underline{i}} f^{\underline{i}})^{l_1 l_2 l_3}_{n} \, S_{k_1 l_1} \right) M_{k_2 l_2} M_{k_3 l_3} + \\
&\left(\left[\delta_{k_2 N} (s^{2}_{\underline{i}} f^{*\underline{i}})^{N l_1 l_3}_{n} - \delta_{k_2 0} (s^{2}_{\underline{i}} f^{*\underline{i}})^{0 l_1 l_3}_{n} \right] - (s^{2}_{\underline{i}} f^{\underline{i}})^{l_1 l_2 l_3}_{n} \, S_{k_2 l_2} \right) M_{k_1 l_1} M_{k_3 l_3} + \\
&\left(\left[\delta_{k_3 N} (s^{3}_{\underline{i}} f^{*\underline{i}})^{N l_1 l_2}_{n} - \delta_{k_3 0} (s^{3}_{\underline{i}} f^{*\underline{i}})^{0 l_1 l_2}_{n} \right] - (s^{3}_{\underline{i}} f^{\underline{i}})^{l_1 l_2 l_3}_{n} \, S_{k_3 l_3} \right) M_{k_1 l_1} M_{k_2 l_2},
\end{aligned}
\tag{3.22}
$$

where $f^{*\underline{i}}$ is the numerical flux that will be described in the next subsection and the *stiffness matrix* is defined as,

$$
S_{ab} = \int_{-1}^{1} \ell_b(\xi) \, \partial_\xi \ell_a(\xi) \, d\xi. \tag{3.23}
$$

In the current implementation in `bamps`, the same number of collocation points i.e., the same polynomial approximation order is assumed in each direction. However, this is not a restriction for the DG scheme since the mass and stiffness matrix are calculated for each direction independently. Using Gauss-Legendre-Lobatto quadrature the stiffness matrix can be written as,

$$
S_{ab} = \int_{-1}^{1} \ell_b(\xi) \, \partial_\xi \ell_a(\xi) \, d\xi = \sum_{k=1}^{N} \ell_b(\xi_k) \, \partial_\xi \ell_a(\xi_k) \omega_k = \partial_\xi \ell_a(\xi_b) \omega_b \equiv D_{ba} \omega_b. \tag{3.24}
$$

Note that the highest order of quadrature approximation for the integral with $N+1$ Legendre-Gauss-Lobatto points and the integrand in the above are of order $2N-1$. Therefore, in the above relation the second equality is exact. For the same reason, the mass matrix can not be determined exactly (here the integrand is of the order $2N$ and the highest quadrature approximation is only $2N-1$ order) in the same simple manner (Teukolsky, 2015). However, the mass lumped approximation,

$$M_{ab} = \int_{-1}^{1} \ell_a(\xi)\, \ell_b(\xi)\, d\xi \approx \sum_{k=1}^{N} \ell_a(\xi_k)\, \ell_b(\xi_k)\omega_k = \delta_{ab}\omega_a. \tag{3.25}$$

is often used in practice. The effect of using this approximation is modal filtering i.e., decreasing the highest mode by a factor $\frac{N}{2N+1}$, see (Gassner et al., 2011). Furthermore, this enables the mass matrix to be represented in a diagonal form which greatly simplifies the DG scheme such that all numerical flux terms only enter the right hand sides, that correspond to boundary points.

Numerical Flux

The discretization of the integrals achieved until Eq. (3.22) leads to a DG scheme on each element with ambiguity at the element boundaries where multiple values are assigned to the same interface, see Fig. 3.1. As already mentioned, the numerical solution is allowed to be discontinuous at element interfaces in a DG method and therefore the value of u_n is not uniquely defined on the element surfaces and neither is $f^{\underline{i}}$. The idea to connect the elements in the domain decomposition unambiguously as borrowed from finite volume methods, is then to introduce a numerical flux. The numerical flux maps the two solutions u_L , u_R on either sides of the interface to a unique value $f^{*\underline{i}}(u_L, u_R)$ that is used as the surface flux for both the elements. A necessary requirement on f^* is its reduction to the physical flux for the continuous solution case i.e., $f^{*\underline{i}}(u,u) = f^{\underline{i}}(u)$. In general, knowledge of the dynamics of the system enters the construction of the numerical flux.

Though there are several widely used options for $f^{*\underline{i}}$ (Harten et al., 1983; Roe, 1981; Shu et al., 1989), we use the HLL (Harten et al., 1983) flux,

$$s_{\underline{i}} f^{*\underline{i}}(u_L, u_R) = \frac{\lambda_+ s_{\underline{i}} f^{\underline{i}}(u_L) - \lambda_- s_{\underline{i}} f^{\underline{i}}(u_R) + \lambda_+\lambda_-(u_R - u_L)}{\lambda_+ - \lambda_-}, \tag{3.26}$$

where λ_+, λ_- are the two characteristic speeds. Furthermore, λ_+, λ_- are chosen to be the maximum propagation speeds in positive and negative s_i direction, constructed from the characteristic eigenvalues of the GRHD system Eqs. (2.51–2.52),

$$\lambda_\pm = \max(0, \pm\lambda_\pm(u_R), \pm\lambda_\pm(u_L)). \tag{3.27}$$

The DG Scheme

The discretized integrals in Eqs. (3.18), (3.20) and (3.22) in combination with Eq. (3.17) gives the final DG scheme as implemented in `bamps`,

$$
\begin{aligned}
&(\partial_t u)_n^{l_1 l_2 l_3} = (s)_n^{l_1 l_2 l_3} + \\
&\frac{1}{(\det J)_n^{l_1 l_2 l_3}} \Big\{ \left(M^{-1}\right)^{0 l_1} \left(s^1_{\underline{i}} f^{*\underline{i}}\right)_n^{0 l_2 l_3} - \left(M^{-1}\right)^{N l_1} \left(s^1_{\underline{i}} f^{*\underline{i}}\right)_n^{N l_2 l_3} + \left(M^{-1}\right)^{m l_1} S_{m k_1} \left(s^1_{\underline{i}} f^{\underline{i}}\right)_n^{k_1 l_2 l_3} \\
&\quad + \left(M^{-1}\right)^{0 l_2} \left(s^2_{\underline{i}} f^{*\underline{i}}\right)_n^{l_1 0 l_3} - \left(M^{-1}\right)^{N l_2} \left(s^2_{\underline{i}} f^{*\underline{i}}\right)_n^{l_1 N l_3} + \left(M^{-1}\right)^{m l_2} S_{m k_2} \left(s^2_{\underline{i}} f^{\underline{i}}\right)_n^{l_1 k_2 l_3} \\
&\quad + \left(M^{-1}\right)^{0 l_3} \left(s^3_{\underline{i}} f^{*\underline{i}}\right)_n^{l_1 l_2 0} - \left(M^{-1}\right)^{N l_3} \left(s^3_{\underline{i}} f^{*\underline{i}}\right)_n^{l_1 l_2 N} + \left(M^{-1}\right)^{m l_3} S_{m k_3} \left(s^3_{\underline{i}} f^{\underline{i}}\right)_n^{l_1 l_2 k_3} \Big\} .
\end{aligned}
\tag{3.28}
$$

As mentioned previously, since the curvilinear grid structure of `bamps` is static, quantities $\det J$ and $s^j_{\underline{i}}$ are pre-evaluated. Moreover, the state dependent fluxes $f^{\underline{i}}(u)$, $f^{*\underline{i}}(u)$ and sources $s(u)$ are also precomputed. The time derivatives of u are supplied to the Runge-Kutta time integrator, in conjunction with the space-time evolution variables from the pseudospectral scheme. An important point to note is that Eq. (3.28) only describes an evolution scheme for the conserved variables, see Eqs. (2.51–2.52). However, for the computation of the flux the primitive variables are also needed. Therefore, a transformation to primitive variables ($\mathbf{w} = \{\rho, v_i, \epsilon\}$) from the conservative variables ($\mathbf{q} = \{D, S_i, E\}$) has to be performed after each Runge-Kutta substep.

3.5 Recovering Primitive Variables

As already encountered, the conserved variables for the matter evolution and the primitive variables are mapped through the relations in Eq. (2.46). As evident from those relations, typical nonlinearity is introduced through the mapping, in particular by the relativistic Lorentz factor W. Therefore, an analytic inversion of the mapping is not available to recover the primitive variables. Instead, the recovery is obtained using the following relations (both in `BAM` and `bamps`),

$$S_iS^i = \left(\rho h W^2\right)^2 v^2 = (\tau + D + p)^2 v^2 =: A(p)^2 v^2 \,, \tag{3.29}$$

$$W(p)^2 = \frac{1}{1-v^2} = \frac{A^2}{A^2 - S_iS^i}\,, \quad \frac{dW}{dp} = -\frac{S_iS^i}{(A^2 - S_iS^i)^{3/2}}\,, \tag{3.30}$$

$$\rho(p) = \frac{D}{W}\,, \quad \frac{d\rho}{dp} = \frac{DS_iS^i}{A^2\sqrt{A^2 - S_iS^i}}\,, \tag{3.31}$$

$$\epsilon(p) = h - 1 - \frac{p}{\rho} = \frac{A}{\rho W^2} - 1 - \frac{p}{\rho} = \frac{1}{D}\left(\frac{A}{W} - D - pW\right)\,, \tag{3.32}$$

$$\frac{d\epsilon}{dp} = \frac{1}{D}\frac{pS_iS^i}{(A^2 - S_iS^i)^{3/2}}\,. \tag{3.33}$$

Since ρ and ϵ are now expressed as functions of p and the conserved variables, one can now apply a root finding procedure on

$$f(p) = p_{EOS}(\rho(p), \epsilon(p)) - p, \tag{3.34}$$

to find p. A Newton-Raphson algorithm is employed,

$$p^{(i+1)} = p^{(i)} - \frac{f(p)}{f'(p)}\,, \tag{3.35}$$

$$f'(p) = \frac{dp_{EOS}}{d\rho}\frac{d\rho}{dp} + \frac{dp_{EOS}}{d\epsilon}\frac{d\epsilon}{dp} - 1\,, \tag{3.36}$$

and for $p^{(0)}$ either the pressure value of the previous timestep, or a value such that $A^2 - S_iS^i$ is positive is used. One can then obtain ρ and ϵ from p using the above relations and furthermore obtain,

$$v^i = \frac{S^i}{A}\,. \tag{3.37}$$

During the transformation from the conservative variables to the primitive ones we have to divide by the density ρ. Therefore, we can not set the density outside the neutron stars to zero i.e., the matter-vacuum interface, which we will see later is categorized as contact discontinuity, is problematic to say the least. To tackle this issue we have to introduce an artificial atmosphere. The atmosphere is set as a low-density, static, and barotropic fluid (simply called atmosphere), where, if ρ is smaller than some freely specifiable threshold ρ_{thr} at some point in the primitive

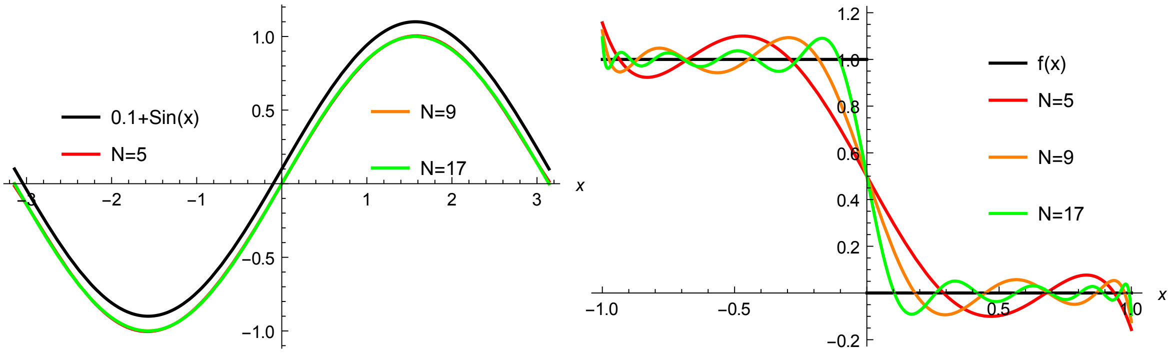

(A) (B)

FIGURE 3.2: **(A)** an infinitely smooth function sin (x) and **(B)** a step function $f(x)$, along with their Fourier-Legendre interpolants for increasing values of N. For the smooth function even the low order interpolant ($N = 5$) reconstructs the original function to a very good accuracy. For the step function, the reconstruction is taken over by high-frequency oscillations of non-decreasing amplitude in the vicinity of the discontinuity. This happens irrespective of the N number of modes used. Note that in **(A)** the original function is translated for better presentation and all the interpolants lie on top of each other.

recovery, we set $\rho = \rho_{\rm atm}$ to avoid unphysical values in the density. However, it is to be noted that the implementation of the artificial atmosphere is unphysical in principle and leads to additional numerical errors. Therefore, $\rho_{\rm atm}$ should be chosen as small as possible. It is furthermore important to note that (a.) all hydrodynamical simulations of BNSs in full general relativity use an atmosphere and (b.) the atmosphere treatment violates mass conservation.

3.6 Spectral Expansions & Discontinuities

It is known that the spectral expansion converges extraordinarily accurate only for smooth functions. For example, in the case of Legendre polynomials the L_2-norm of the difference between any C^m function f and its spectral interpolant $I_N f$, cf. Eq. (3.4), is approximately given by

$$||u - I_N f||_2 \leq \frac{C}{N^{m-1/2}} \sum_{k=0}^{m} ||f^{(k)}||_2, \tag{3.38}$$

where C is a positive constant, see (Grandclément et al., 2009). Similar norms can be estimated for other sets of orthogonal basis functions. For any C^∞ function it is interesting to see that the norm in the above decays much faster than any power of

N, cf. Fig. 3.2a. This is the known spectral convergence. However, it is important to note that this does not mean that the error decays exponentially. Exponential convergence is only obtained for analytic functions.

For systems showing discontinuities, Eq. (3.38) does not even confirm convergence. The local behavior in the vicinity of the function's discontinuity spoils the global approximation within the domain cf. Fig. 3.2b. This is known as the Gibbs phenomenon (Gibbs, 1898).

In the proximity of the discontinuity, the reconstruction is taken over by high-frequency oscillations of non-decreasing amplitude. It happens irrespective of the N number of modes used. This behavior prevents the recovery of true solution, making the method unsuitable for discontinuous problems of interest, such as fluid shocks or stellar surfaces. In chapter 6 we will present the outcome of using the DG method in solving the GRHD equations with first test cases.

Chapter 4

Highly Eccentric Binary Neutron Stars

In this chapter we review our work on the first detailed study of highly eccentric BNS systems as studied in Chaurasia et al. (2018) with full (3+1)D numerical relativity simulations using consistent initial data, i.e., setups which are in agreement with the Einstein equations and with the equations of general relativistic hydrodynamics in equilibrium. The problems with using inconsistent ID are constraint violations, in cases for which the Einstein constraints are not fulfilled for the ID, or spurious matter density oscillations if the fluid is not in equilibrium. Those oscillations potentially spoil the quantitative analysis of matter oscillations which arise due to the encounters in eccentric BNSs.

The chapter is structured as follows: In Sec. 4.1 we present the outline of the strategy followed for constructing consistent ID for the BNS configurations studied in this thesis and summarize the properties of the binaries we simulate. Section 4.2 describes briefly the evolution setup used for the `BAM` simulations of highly eccentric BNS systems. In Secs. 4.3, 4.4 and 4.5 we review the findings of Chaurasia et al. (2018). Finally, in Sec. 4.6 we present a short dicussion on the convergence of the `BAM` simulations of highly eccentric BNSs.

4.1 Initial Data

To construct quasi-equilibrium configurations for BNSs we need to find quasi-stationary solutions[1] to the relativistic equations of hydrodynamics i.e., in addition to solving the constraint Eqs. (2.25), we need to find a rest-mass density (ρ) and a fluid four-velocity (u^μ) that, given an equation of state, satisfy the conservation of energy-momentum (2.32) and the conservation of rest-mass (2.33), to ensure consistency of our data. Furthermore, this requires the existence of a *Killing* vector to ensure that the solution is in equilibrium. Once these configurations are available, they can be used as initial data for dynamical simulations.

---

[1] In stationary equilibrium an observer corotating with the binary would not notice any change in the binary's structure with time. The motion of such a binary is generated by a "helical" Killing vector.

General Strategy

For the work in this thesis, the initial configurations are constructed with the pseudospectral `SGRID` code as described by Dietrich et al. (2015a) and Tichy (2006, 2009a,b). `SGRID` uses the XCTS formalism, see Sec. 2.1.4, in combination with the constant rotational velocity (CRV) approach (Tichy, 2011, 2012) to construct quasi-equilibrium configurations of spinning neutron stars and the methods presented by Moldenhauer et al. (2014) to allow for eccentric BNSs. The details of the eccentric BNS configurations studied in this thesis are given in Table. 4.1. All but two simulations presented in this thesis were made publicly available in the CoRe database of binary neutron star merger waveforms; see (CoRe, 2018; Dietrich et al., 2018a). The remaining waveforms will be made available in the near future.

Here we do not go into the details of the method obtaining the initial data but only give an outline for the strategy followed. Note that a similar strategy is followed in obtaining consistent initial data for BNSs on quasi-circular orbits.

In addition to the the XCTS approach outlined in Sec. 2.1.4, `SGRID` uses additional assumptions to construct consistent ID as outlined in the following:

Assumptions for the metric fields:- With the available freedom in choosing $\bar{\gamma}_{ij}$, $\bar{u}^{ij}$, K and $\partial_t K$ for the Hamiltonian constraint Eq. (2.25) and the XCTS Eqs. (2.30,2.31), one assumes conformal flatness, $\bar{\gamma}_{ij} = f_{ij}$, where f_{ij} describes the flat metric (δ_{ij} in Cartesian coordinates), which leads to ${}^{(3)}\bar{R} = 0$, and maximal slicing, $K = 0$. Moreover, these conditions are preserved infinitesimally in time, i.e. $\partial_t \bar{\gamma}_{ij} = \bar{u}_{ij} = 0$ and $\partial_t K = 0$.

These assumptions[2] lead to the following set of elliptic equations that give the five metric quantities (ψ, β^i, α),

$$
\begin{aligned}
\partial^i\partial_i\psi &= -\frac{1}{8}\psi^5(A_{ij}A^{ij} + 16\pi E), \\
\partial^j\partial_j\beta^i + \frac{1}{3}\partial^i\partial_j\beta^j &= 2\psi^{10}A^{ij}\partial_j(\alpha\psi^{-6}) + 16\pi\alpha\psi^4 S^i, \\
\partial^i\partial_i(\alpha\psi) &= \alpha\psi^5\left[\frac{7}{8}A_{ij}A^{ij} + 2\pi(E + 2S)\right].
\end{aligned} \tag{4.1}
$$

Assumptions for the matter fields:- As a prerequisite to obtain quasi-equilibrium configurations, the method requires the existence of an approximate symmetry or Killing vector, k^α, near each star,

$$
k^\alpha_{ecc1,2} = t^\alpha + \Omega\left[(x - x_{c1,2})y^\alpha - yx^\alpha\right]. \tag{4.2}
$$

The symmetry vector or the *helliptical* killing vector k^α as described by Moldenhauer et al. (2014) requires to,

(i) approximately Lie-drag the flow;

(ii) point along the motion of the star center;

(iii) allow each star center to move along a segment of an elliptic orbit at apoapsis; see (Moldenhauer et al., 2014, Fig. 2).

The radii of the inscribed circles are $r_{c1,2} = (1 - e)d_{1,2}$, where e is the input eccentricity parameter and $d_{1,2} = |x_{1,2} - x_{CM}|$ are the distances of the stars from the center of mass assuming that apoapsis occurs on the x-axis for simplicity. The two inscribed circles are centered around $x_{c1,2} = x_{1,2} \mp r_{c1,2} = x_{CM} + e(x_{1,2} - x_{CM})$.

To ensure that the fluid quantities ρ and u^μ describe an equilibrium configuration, we require these quantities to be Lie-dragged along the helliptcal Killing vector, see (Moldenhauer et al., 2014; Tichy, 2011) and references therein i.e.,

$$
\mathcal{L}_{\mathbf{k}}\rho = 0, \quad \mathcal{L}_{\mathbf{k}}u^\mu = 0. \tag{4.3}
$$

---

[2] Note that if one imposes the conditions $K = 0$ and $\bar{\gamma}_{ij} = f_{ij}$ from the beginning and preserves these conditions in time then $\partial_t K = \partial_t\bar{\gamma}_{ij} = 0$ follows, imposing quasi-equilibrium but without assuming Killing symmetry; see (Moldenhauer et al., 2014). A notion of Killing vector is important when there are matter fields but is not necessary while constructing quasi-equilibrium BBH ID.

TABLE 4.1: BNS configurations. The first column gives the configuration name and the second column gives the corresponding CoRe database ID. The next 5 columns provide the physical properties of the single stars: the EOS, the gravitational masses of the individual stars $M^{A,B}$, the baryonic masses of the individual stars $M_b^{A,B}$, the stars' dimensionful and dimensionless spins $S^{A,B}$ and $\chi^{A,B}$. The last 5 columns give the input eccentricity e [Eq. (4.2)], the 3PN eccentricity $\hat{e}_{\rm 3PN}$ [Eq. (4.4)], the initial GW frequency $M\omega_{22}^0$, the ADM mass $M_{\rm ADM}$, and the ADM angular momentum $J_{\rm ADM}$. The configurations evolved with different resolutions (cf. Table 4.2) are marked with asterisks (*). Adapted from (Chaurasia et al., 2018).

Name	CoRe DB ID	EOS	$M^{A,B}$	$M_b^{A,B}$	$S^{A,B}$	$\chi^{A,B}$	e	$\hat{e}_{\rm 3PN}$	$M\omega_{22}^0$	$M_{\rm ADM}$	$J_{\rm ADM}$
SLy$-e0.40^{00}$	BAM:0112	SLy	1.357558	1.504	0.0000	0.0000	0.40	0.52	0.0106	2.702935	8.8086
SLy$-e0.45^{00*}$	BAM:0113	SLy	1.357558	1.504	0.0000	0.0000	0.45	0.55	0.0110	2.702408	8.4514
SLy$-e0.50^{00*}$	BAM:0114	SLy	1.357558	1.504	0.0000	0.0000	0.50	0.60	0.0116	2.701945	8.0487
SLy$-e0.60^{00}$	BAM:0115	SLy	1.357558	1.504	0.0000	0.0000	0.60	0.69	0.0129	2.700947	7.1828
SLy$-e0.40^{\uparrow\uparrow}$	BAM:0116	SLy	1.358097	1.504	0.1767	0.0958	0.40	0.50	0.0107	2.703786	9.2346
SLy$-e0.45^{\uparrow\uparrow *}$	BAM:0117	SLy	1.358097	1.504	0.1767	0.0958	0.45	0.54	0.0111	2.703281	8.8478
SLy$-e0.50^{\uparrow\uparrow}$	BAM:0118	SLy	1.358097	1.504	0.1767	0.0958	0.50	0.59	0.0117	2.702773	8.4440
SLy$-e0.60^{\uparrow\uparrow}$	BAM:0119	SLy	1.358097	1.504	0.1767	0.0958	0.60	0.69	0.0130	2.701827	7.5714
MS1b$-e0.45^{00}$	BAM:0074	MS1b	1.380825	1.504	0.0000	0.0000	0.45	0.47	0.0119	2.748643	9.1766
MS1b$-e0.50^{00}$	BAM:0075	MS1b	1.380825	1.504	0.0000	0.0000	0.50	0.53	0.0125	2.748120	8.7322
MS1b$-e0.60^{00}$	BAM:0076	MS1b	1.380825	1.504	0.0000	0.0000	0.60	0.64	0.0139	2.747100	7.7936
MS1b$-e0.45^{\uparrow\uparrow}$	BAM:0077	MS1b	1.381270	1.504	0.2016	0.1056	0.45	0.48	0.0119	2.749629	9.5789
MS1b$-e0.50^{\uparrow\uparrow}$	BAM:0078	MS1b	1.381270	1.504	0.2016	0.1056	0.50	0.53	0.0125	2.749104	9.1487
MS1b$-e0.60^{\uparrow\uparrow}$	BAM:0079	MS1b	1.381270	1.504	0.2016	0.1056	0.60	0.64	0.0139	2.748047	8.2188

Eccentric Configurations

A total of 14 different physical configurations, as summarized in Table 4.1, are considered. All the setups employed at least the R2 resolutions; see Table 4.2 for more details. A subset of configurations were also simulated with grid setups R1, R3, and R4. Those setups are marked with an asterisk (*) in Table 4.1. The configurations used in this study focus on equal-mass setups with baryonic masses $M_b^A = M_b^B \simeq 1.504 M_\odot$ at a fixed initial separation ($\sim$ 165 km) with two different EOSs. The chosen EOSs, SLy and MS1b, are reasonably representative of soft and stiff EOSs, respectively. The stars are either irrotational or have dimensionless spins of $\chi \simeq 0.1$ oriented parallel to the orbital angular momentum. The name of the simulations refer to: the EOS, the input eccentricity parameter used in Eq. (4.2), and the spin orientations.

In addition to the definition of eccentricity given in Eq. (4.2), the post-Newtonian (PN) eccentricity is also computed from the ADM expressions for the energy and angular momentum. Dietrich et al. (2015a) give an extensive comparison between different order PN eccentricities and the eccentricity measure used in the helliptical symmetry vector in `SGRID`. Following them, we use the 3PN expression for eccentricity, in (Dietrich et al., 2015a, Eq. 4.8), computed following Mora et al. (2004). For completeness the full expression is given below:

$$
\begin{aligned}
\hat{e}^2_{\mathrm{3PN}} = {} & 1 - 2\xi + \left[-4 - 2\nu + (-1+3\nu)\xi\right] E_b \\
& + \left[\frac{20-23\nu}{\xi} - 22 + 60\nu + 3\nu^2 - (31\nu + 4\nu^2)\xi\right] E_b^2 \\
& + \biggl[\frac{-2016 + (5644 - 123\pi^2)\nu - 252\nu^2}{12\xi^2} \\
& + \frac{4848 + (-21128 + 369\pi^2)\nu + 2988\nu^2}{24\xi} \\
& - 20 + 298\nu - 186\nu^2 - 4\nu^3 \\
& + \left(-30\nu + \frac{283}{4}\nu^2 + 5\nu^3\right)\xi\biggr] E_b^3.
\end{aligned}
\tag{4.4}
$$

Here $\xi := -E_b \ell^2$ and $\nu := M^A M^B / M^2$ is the symmetric mass ratio, where $E_b = (M_{\mathrm{ADM}}/M - 1)/\nu$ is the binary's (reduced) binding energy, $\ell = (J_{\mathrm{ADM}} - S^A - S^B)/(M^2\nu)$ is its specific orbital angular momentum, $M^{A,B}$ are the individual gravitational masses of the stars in isolation, $M := M^A + M^B$ is the binary's total mass, M_{ADM} is its ADM mass, J_{ADM} is its ADM angular momentum, and $S^{A,B}$ are the (dimensionful) spins of the stars. The eccentricities input into `SGRID` and the computed 3PN eccentricities are listed in Table 4.1 for all the configurations.

Note that Eq. (4.4) only includes nonspinning point mass contributions to the energy and angular momentum. However, including the leading spin-orbit and tidal contributions gives almost identical results, see (Chaurasia et al., 2018) for details on including these terms. This suggest that a higher-order calculation of the spin-dependent contributions, going beyond the ingredients provided by Mora et al. (2004), will be necessary to make an accurate PN eccentricity estimate for more highly spinning cases.

4.2 Evolutions

Numerical relativity simulations are performed with the `BAM` code; see (Bernuzzi et al., 2016a; Brügmann et al., 2008; Dietrich et al., 2015b; Thierfelder et al., 2011) for details. As discussed in Chapter 2, the Einstein equations are written in 3+1 form

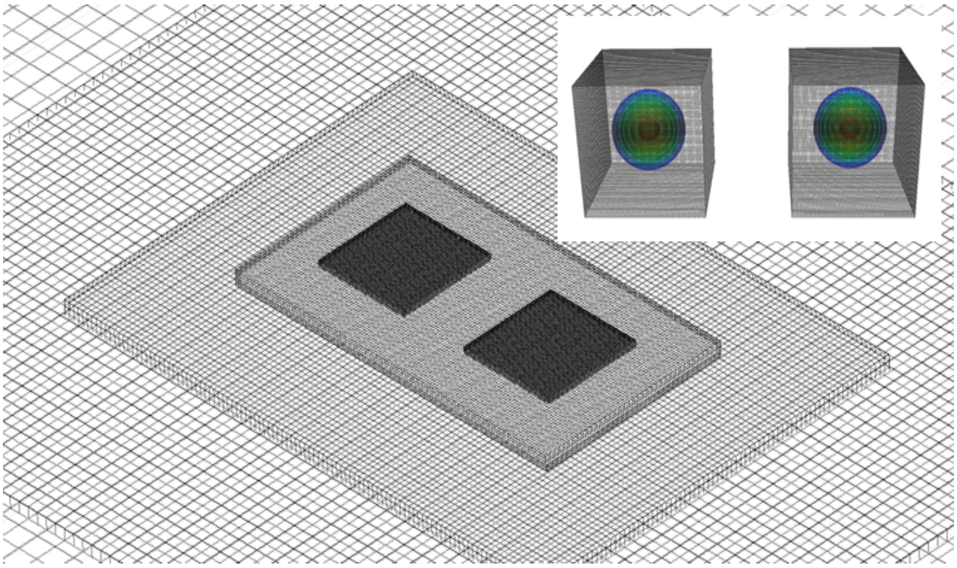

FIGURE 4.1: Mesh refinement implemented in BAM. The computational domain comprises of hierarchically nested Cartesian grids called *levels*. The outermost level or the base level is the coarsest, and the consecutive inner levels refine the domain by a factor of two. Some of the inner boxes can dynamically move, tracking the matter during evolution. Compact objects (NSs or BHs) are covered with the finest resolution box (inset) such that the near-field dynamics can be resolved accurately. Such a refinement strategy is important to study the different scales of dynamics happening, from a few tens-of-meters (as in the interior of NSs) to a few thousand kilometers (where GWs can be extracted unambiguously), cf. Table 4.2 where we report the different grid resolutions used. Picture credit: Dr. Tim Dietrich

using the BSSNOK evolution system. For slicing conditions for the evolution system, the (1+log)-lapse and gamma-driver-shift conditions are employed (Alcubierre et al., 2003; Bona et al., 1996; Meter et al., 2006). General relativistic hydrodynamics equations are solved as discussed in Sec. 2.2. The system is closed by an EOS for which we use piecewise-polytropic fits, cf. Eq. (2.54c), of the SLy and MS1b EOSs; see (Read et al., 2009b). Thermal effects are included by adding an additional thermal pressure of the form $p_{\rm th} = \rho\epsilon(\Gamma_{\rm th} - 1)$ with $\Gamma_{\rm th} = 1.75$; see (Bauswein et al., 2010).

The computational domain is decomposed into a hierarchy of cell centered nested Cartesian grids; see Fig. 4.1. The hierarchy consists of L levels of refinement labeled by $l = 0, \cdots, L-1$. Each refinement level l has one or more Cartesian grids with constant grid spacing h_l and n (or $n^{\rm mv}$) points per direction. The refinement factor is two such that $h_l = h_0/2^l$. The grids are properly nested i.e., the coordinate extent of any grid at level l, $l > 0$, is completely covered by the grids at level $l-1$. Some of the mesh refinement levels $l > l^{\rm mv}$ can be dynamically moved and adapted during

TABLE 4.2: Grid configurations. The columns refer to: the resolution name, the number of points in the non-moving boxes n, the number of points in the moving boxes n^{mv}, the grid spacing in the finest level h_8 covering the NS diameter, the grid spacing in the coarsest level h_0, and the outer boundary position R_0. The grid spacing and the outer boundary position are given in units of $M_\odot$. Adapted from (Chaurasia et al., 2018).

Name	n	n^{mv}	h_8	h_0	R_0
R1	128	64	0.219	56.00	3612.000
R2	192	96	0.146	37.38	3606.784
R3	256	128	0.110	28.03	3602.112
R4	320	160	0.088	22.43	3599.309

the evolution according to the technique of "moving boxes"; for this work we set $l^{\mathrm{mv}} = 5$. The `BAM` grid setup considered in this work consists of nine refinement levels. Details about the different grid configurations employed in this work are given in Table 4.2; the grid configurations are labeled R1, R2, R3, R4, ordered by increasing resolution.

Time integration is performed with the method of lines using explicit fourth-order Runge-Kutta integrators. Derivatives of metric fields are approximated by fourth-order finite differences (Sec. 3.2), while a high-resolution-shock-capturing (HRSC) scheme based on primitive reconstruction (i.e. reconstruction or limiting is performed on the primitive variables as compared to the conserved variable) and the local Lax-Friedrichs (LLF) central scheme for the numerical fluxes is adopted for the matter (Thierfelder et al., 2011). Primitive reconstruction is performed with the fifth order WENOZ scheme of Borges et al. (2008). In order to recover the primitives from the conservative variables, the strategy as described in Sec. 3.5 is followed.

4.3 Dynamics

Orbital motion

One finds that although the initial distance is the same for all configurations, the number of orbits until merger varies significantly as visible in Fig. 4.2. In particular, for an increasing eccentricity, one finds the number of orbits to be $\sim 15.5, 10.5, 5.5$, and 0.5 as computed from Fig. 4.3. The orbits are seen to undergo apsidal (orbital) precession, where the orbit of the NSs rotates in the plane of motion. The reduction of eccentricity due to the emission of GWs (Peters, 1964) is clearly visible from the evolution of the proper distance between the neutron stars as in Fig. 4.3.

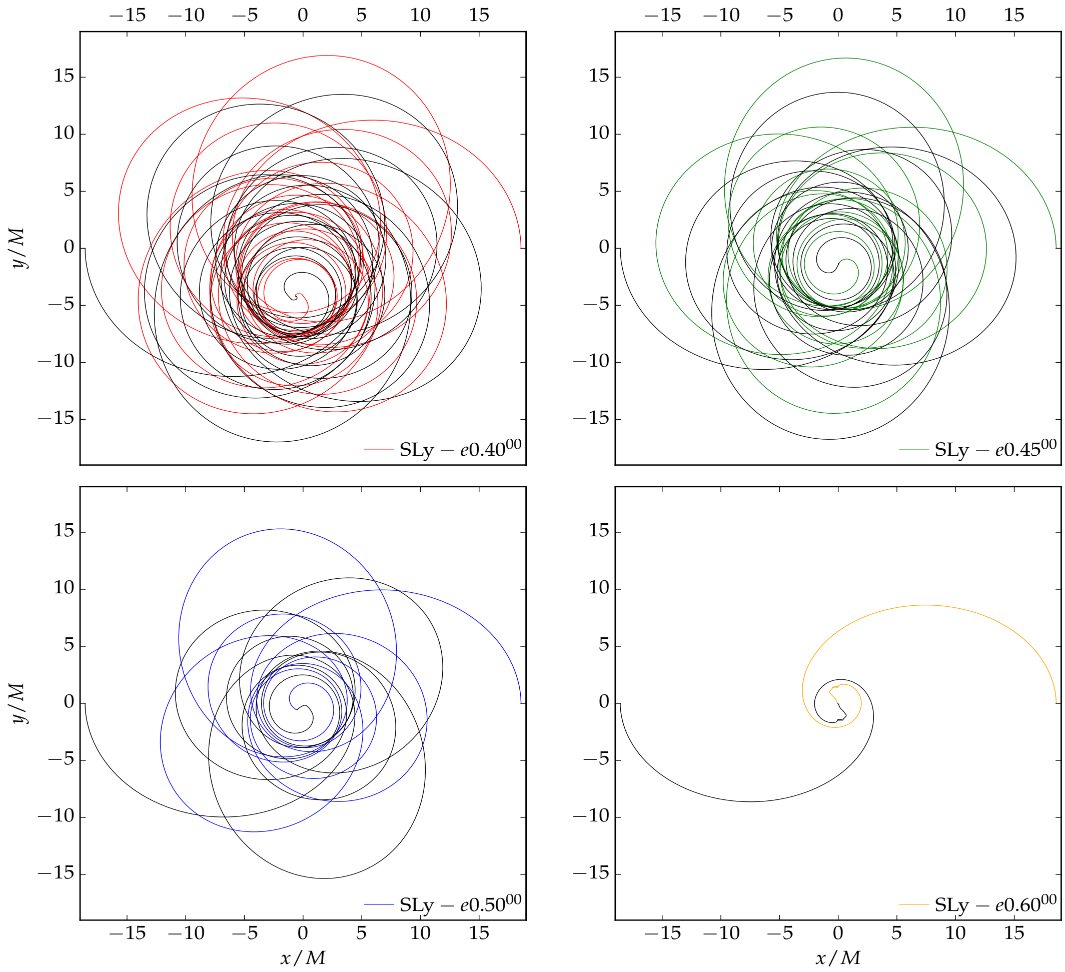

FIGURE 4.2: Tracks of the star centers for the SLy^{00} cases. Each panel refers to a different input eccentricity: $e = 0.40$ (upper left, red), $e = 0.45$ (upper right, green), $e = 0.50$ (lower left, blue), $e = 0.60$ (lower right, orange). The star that originally starts on the left-hand side always has its track colored black.

In order to elaborate on the orbital dynamics and the eventual merger, we present the SLy$-e0.50^{00}-$R2 configuration in Fig. 4.4. The stars in this case perform ~ 5.5 encounters until they finally merge. During the inspiral, the system emits energy and angular momentum in the form of GWs. The NSs come to within ~ 45 km of each other during the periastron encounters, causing the deformation of the individual stars to increase due to stronger tidal forces induced by the companion. Because of these deformations the stars start to oscillate. Moreover, at a later stage in the evolution, a fraction of the material is ejected from the system during grazing encounters. Figure 4.4 shows the ejecta on a brown to green color scale whereas the bound density is shown from blue to red. In particular, the second column plot shows a large amount of matter which gets ejected from the system just after

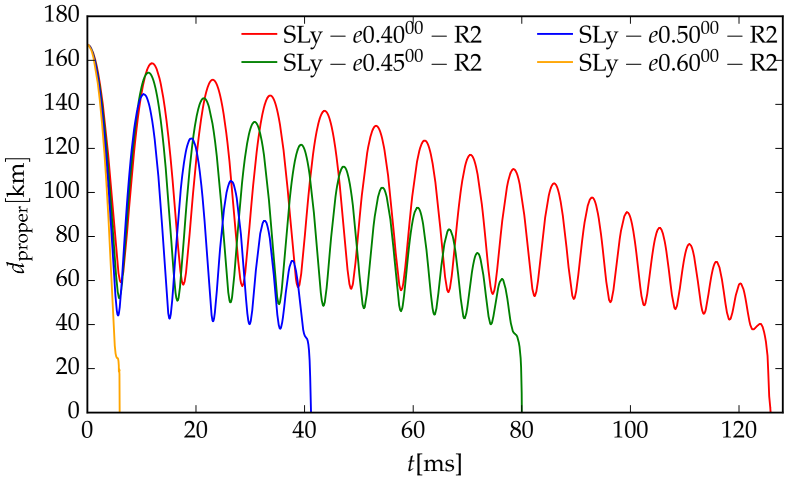

FIGURE 4.3: The evolution of the proper distance between the two non-spinning NSs with SLy EOS and with different initial eccentricities. For the system with less initial eccentricity, the stars do not approach each other as closely, compared to the system with relatively larger initial eccentricity. In other words, the larger the initial eccentricity the smaller is the impact parameter. Adapted from (Chaurasia et al., 2018).

a grazing periastron encounter. At the onset of merger (third column) one clearly sees tidal tails behind the two stars from which most material is released. Lastly, after the merger, the remnant stabilizes and either forms a stable massive neutron star (MNS, MS1b cases) or a hypermassive neutron star (HMNS, SLy cases).

Energetics

The conservative dynamics of the system can be understood qualitatively by computing the binding energy E_b and specific angular momentum ℓ from our numerical simulations (definitions given in the discussion below Eq. (4.4)), see e.g., (Bernuzzi et al., 2014a; Damour et al., 2012; Dietrich et al., 2017a).

Figure 5.2 shows the binding energy versus the specific angular momentum curves for the nonspinning (top panel) and spin-aligned (bottom panel) SLy (A) and MS1b (B) configurations. It is found that for increasing eccentricity, the curves start with less angular momentum, even though the initial distance is fixed. In the limit of $e \nearrow 1$, one would obtain an initial specific orbital angular momentum of $\ell = 0$, because then, at the star center, the symmetry vector of Eq. (4.2) and therefore the fluid velocity will have no component perpendicular to the position vector of the star's center (i.e., no y-component).

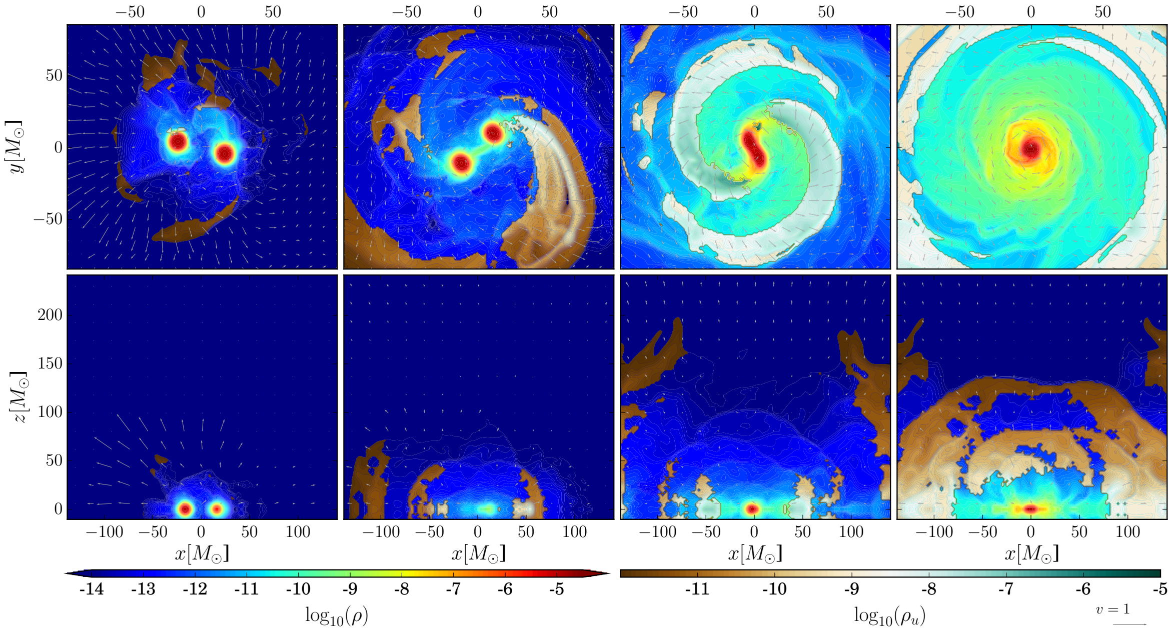

FIGURE 4.4: 2D-plots for the SLy-e0.50^{00}−R2 configuration showing the density and velocity field at different times, with the unbound material [computed using the criterion in Eq. (A.1)] shown in the brown to green color scale, while the bound material is shown in a blue to red color scale. *Top row* plots show the $xy-$plane covering a distance of $\sim$ 176 km in each direction; *Bottom row* plots show the $xz-$plane, where each direction is covering a distance of $\sim$ 440 km. *First column*: Time after the first encounter, where the stars come as close as $\sim$45 km (proper distance). As the stars undergo a tightly bound whirl orbit, one can see that some low-density matter is ejected. *Second column*: Time after third periastron encounter at a later time in the evolution. Here also we see similar features as in the first case except that there is also mass transfer at a density $\sim \mathcal{O}(10^{-9}) - \mathcal{O}(10^{-8})$ $[\mathcal{O}(10^{8}) - \mathcal{O}(10^{9})$ g/cm$^3]$. *Third column*: Time just before the merger. Unbound matter with densities $\mathcal{O}(10^{-7}) - \mathcal{O}(10^{-6})$ $[\mathcal{O}(10^{10}) - \mathcal{O}(10^{11})$ g/cm$^3]$ is ejected from the tidal tail and as the unbound matter expands its density decreases. *Fourth column*: Post-merger phase when the cores of the NSs have merged and formed a hypermassive NS.

As the system inspirals, energy and angular momentum are emitted in the form of GWs. In general, for an increasing eccentricity, the slope of the individual curves increases. Consequently, the dimensionless frequency $M\hat{\Omega} = \partial E_b/\partial \ell$ at a given specific orbital angular momentum is larger for increasing values of the eccentricity. The systems are less bound for larger eccentricities at fixed ℓ during the early part of the inspiral as predicted by PN theory; see (Mora et al., 2004). We find the behavior of the dimensionless frequency with eccentricity to be opposite to that predicted by PN theory. The cause of the difference is not clear, but could be due to the fact that most of the energy and angular momentum are lost near periastron, where the PN approximation is not very accurate. In the most extreme case the

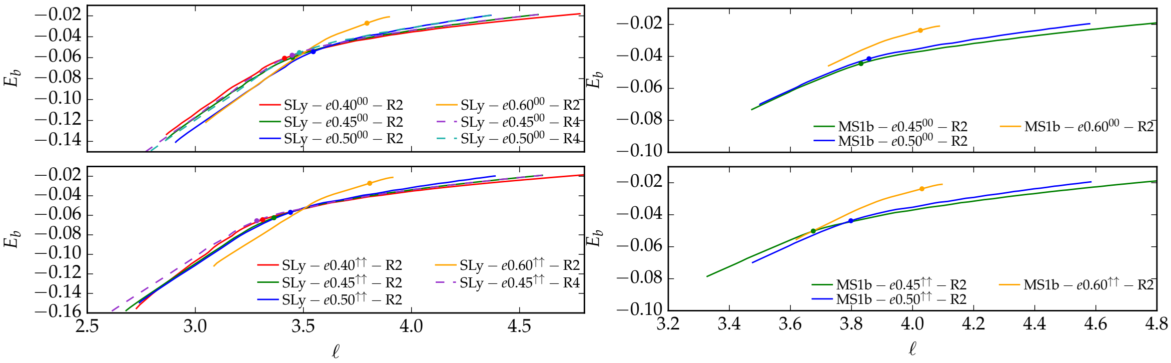

(A) (B)

FIGURE 4.5: Binding energy vs. specific angular momentum curves $E_b(\ell)$ for, **(A)**: SLy EOS and **(B)**: MS1b EOS, for nonspinning (top panel) and aligned spin configurations (bottom panel). The moments of merger are marked by circles. Adapted from (Chaurasia et al., 2018).

stars would perform a head on collision for which the angular momentum remains zero regardless of the separation. The stars can be almost unbound even for very small (or even zero) angular momentum. This cannot be achieved for setups with decreasing eccentricity.

We notice that close to the merger and after the merger the ordering of the binding energy curves changes. The merger itself is marked by circles in Fig. 5.2. This observation can be understood as follows. The moment of merger marks the initial configuration for the evolution of the postmerger. Consequently when the angular momentum and binding energy is larger the remnant is less bound and rotates faster i.e., $\hat{\Omega}$ is larger.

Merger Remnant

Owing to the choice of the particular total mass of $M \sim 2.7 M_\odot$, in general, three different outcomes are found for the simulations presented. One possible outcome is the formation of a stable MNS in cases where the total mass of the remnant is below the maximum allowed mass of a spherically symmetric star for the given EOS. Since MS1b supports non-rotating stars with masses up to $\sim 2.76 M_\odot$, all remnants formed by the merger of the MS1b configurations are indeed found to be MNSs. On the other hand, the SLy EOS instead only supports nonrotating stars with masses up to $\sim 2.06 M_\odot$. Consequently the remnant is unstable and will collapse to a BH. In fact, the total masses of the remnants formed during the merger of the SLy setups even exceeds the maximum mass of $\sim 2.5 M_\odot$ of a rigidly rotating SLy star, and hence the remnants from such setups are characterized as HMNSs (Baiotti et al., 2017; Baumgarte et al., 2000; Hotokezaka et al., 2013a). Four out of the eight SLy configurations form a BH during the simulation time, at the R2 resolution, see Table 4.3; one additional configuration only forms a BH during the simulation time at higher resolutions. (The other cases that do not form a BH during the simulation time were not evolved at higher resolutions.)

TABLE 4.3: Properties of the merger remnant and ejecta for all setups. The columns refer to: the name of the configuration, the mass of the ejecta from the volume integral $M^{\mathcal{V}}_{\rm ej}$, the mass of the ejecta from the matter flux through coordinate spheres $M^{\mathcal{S}}_{\rm ej}$, the kinetic energy of the ejecta $T_{\rm ej}$, the D-weighted integral of $v^2 = v^i v_i$ of fluid elements inside the orbital plane $\langle \bar{v} \rangle_\rho$ and perpendicular to it $\langle \bar{v} \rangle_z$, the lifetime, τ, of the HMNS formed during our simulation, given in $M_\odot$ and in ms; the final mass of the BH, $M_{\rm BH}$, if the HMNS collapsed during our simulation; the dimensionless spin of the final BH, $\chi_{\rm BH}$ and the mass of the disk surrounding the BH, $M_{\rm disk}$ (see Appendix A for details on computing these quantities). We also show the quantities computed from different resolutions for some configurations. The quantities for configurations that did not undergo collapse to a BH (SLy) or formed a MNS (MS1b) are marked with "$-$". Adapted from (Chaurasia et al., 2018).

Name	$M^{\mathcal{V}}_{\rm ej}$	$M^{\mathcal{S}}_{\rm ej}$	$T_{\rm ej}$		$\langle \bar{v} \rangle_\rho$	$\langle \bar{v} \rangle_z$	τ		$M_{\rm BH}$	$\chi_{\rm BH}$	$M_{\rm disk}$
	$[10^{-2} M_\odot]$		$[10^{-5} M_\odot]$	$[10^{49}$ erg$]$	$[c]$	$[c]$	$[M_\odot]$	[ms]	$[M_\odot]$		$[M_\odot]$
SLy$-e0.40^{00}-$R2	2.06	1.96	55.0	98.3	0.08	0.15	1300	6.4	2.58	0.62	0.08
SLy$-e0.45^{00}-$R1	2.00	1.84	14.0	25.0	0.09	0.14	2100	10.3	2.53	0.55	0.09
SLy$-e0.45^{00}-$R2	1.07	1.02	5.6	10.0	0.11	0.14	6000	29.6	2.45	0.48	0.13
SLy$-e0.45^{00}-$R3	2.03	1.95	10.0	17.9	0.13	0.15	-	-	-	-	-
SLy$-e0.45^{00}-$R4	1.13	1.08	9.7	17.4	0.14	0.16	3200	15.8	2.48	0.54	0.09
SLy$-e0.50^{00}-$R1	0.90	0.89	1.0	1.7	0.06	0.06	-	-	-	-	-
SLy$-e0.50^{00}-$R2	0.49	0.46	1.6	2.9	0.10	0.11	-	-	-	-	-
SLy$-e0.50^{00}-$R3	1.90	1.74	20.0	35.7	0.09	0.09	1700	8.4	2.55	0.59	0.07
SLy$-e0.50^{00}-$R4	0.32	0.27	1.5	2.7	0.11	0.13	2700	13.3	2.51	0.56	0.09
SLy$-e0.60^{00}-$R2	0.23	0.21	1.3	2.4	0.12	0.14	-	-	-	-	-
SLy$-e0.40^{\uparrow\uparrow}-$R2	1.54	1.52	9.6	17.2	0.11	0.15	1900	9.4	2.56	0.60	0.07
SLy$-e0.45^{\uparrow\uparrow}-$R1	0.94	0.90	3.1	5.5	0.09	0.11	5400	26.6	2.42	0.46	0.16
SLy$-e0.45^{\uparrow\uparrow}-$R2	0.30	0.35	1.2	2.2	0.10	0.11	2400	11.8	2.54	0.59	0.07
SLy$-e0.45^{\uparrow\uparrow}-$R3	0.82	0.81	6.6	11.7	0.14	0.15	2500	12.3	2.54	0.58	0.07
SLy$-e0.45^{\uparrow\uparrow}-$R4	0.68	0.65	2.9	5.18	0.10	0.11	-	-	-	-	-
SLy$-e0.50^{\uparrow\uparrow}-$R2	0.70	0.65	1.7	3.1	0.08	0.09	-	-	-	-	-
SLy$-e0.60^{\uparrow\uparrow}-$R2	1.15	1.06	4.4	7.9	0.11	0.12	-	-	-	-	-
MS1b$-e0.45^{00}-$R2	1.12	1.05	2.3	4.1	0.06	0.08	-	-	-	-	-
MS1b$-e0.50^{00}-$R2	1.55	1.49	2.8	5.0	0.06	0.08	-	-	-	-	-
MS1b$-e0.60^{00}-$R2	0.33	0.29	1.2	2.2	0.10	0.10	-	-	-	-	-
MS1b$-e0.45^{\uparrow\uparrow}-$R2	1.72	1.69	6.6	11.8	0.10	0.10	-	-	-	-	-
MS1b$-e0.50^{\uparrow\uparrow}-$R2	0.90	0.85	2.0	3.5	0.08	0.09	-	-	-	-	-
MS1b$-e0.60^{\uparrow\uparrow}-$R2	3.49	3.15	12.9	23.1	0.10	0.11	-	-	-	-	-

Lifetime of the merger remnant:- The lifetime and merger properties in our simulations are mostly affected by the total mass of the system and the EOS (Dietrich et al., 2015b; Hotokezaka et al., 2013a). It is generally true that systems with a softer EOS collapse earlier than systems with a stiffer EOS. In cases where the EOS is stiff enough, MNSs can form, as in our MS1b simulations. Systems with stiffer EOS are in general less bound at the merger than systems with softer EOS. The relations presented in (Bernuzzi et al., 2014b; Read et al., 2013; Takami et al., 2015) also imply that stiffer EOSs lead to merger remnants with larger angular momentum support. In addition to the angular momentum support, the pressure support in the central regions is larger for stiffer EOS, and the merger remnant is even further stabilized. Apart from the dependence on physical quantities, e.g., angular momentum and EOS, the lifetime of the merger remnant is also very sensitive to numerical errors and grid resolutions, as discussed in, e.g., (Bernuzzi et al., 2014a, 2016b; Hotokezaka et al., 2013a). It is thus difficult to quantify the collapse time, and uncertainties can be of the order of several milliseconds, cf. Table 4.3. When shocks form, e.g. during the collision of the stars, even high order - high resolution shock capturing methods lose their high convergence properties (Bernuzzi et al., 2016a; Bugner, 2017; Guercilena et al., 2017). In chapter 5 we will present results from the investigations of using high order spectral methods a.k.a the discontinuous Galerkin methods for solving the GRHD equations. We will further comment on the issue of convergence and robustness of numerical methods with respect to numerical relativity. Overall, it is found that the measurement of the remnant's lifetime is less robust for eccentric orbits than for quasi-circular ones. This could be due to the sensitive dependence of the postmerger evolution on the number of close encounters before merger, which itself depends sensitively on the eccentricity, spin, and/or resolution; see Sec. 4.6.

Despite these issues, a robust feature seems to be that configurations with larger initial eccentricity with a fixed initial separation have larger angular momentum at the moment of merger. Due to the larger angular momentum at the moment of merger, a delayed BH formation is expected. While it is found that this is in agreement with the results at the R2-resolutions for which the largest set of simulations is available, higher resolutions suggest a more complicated picture. A further study to quantify the remnant lifetime is therefore scheduled for the future. On the other hand, the imprint of spin is less clear. While it is found that spin aligned with the orbital angular momentum leads to a delayed merger (orbital hang-up effect (Bernuzzi et al., 2014a; Campanelli et al., 2006)), it is also seen that more angular momentum and energy in the form of GWs is emitted before the merger and hence the formed merger remnant has less angular momentum leading to a faster collapse.

Black hole and disk properties:- Four out of the 14 configurations collapse to a BH after the merger during our simulation time at the R2 resolution, and one more collapses when run at higher resolutions. We expect that if we evolved our configurations with the SLy EOS for longer times then all configurations would have formed BHs. In cases where a BH forms, we report the BH mass M_{BH}, the dimensionless spin χ_{BH} of the BH, and the mass of the accretion disk M_{disk} in Table 4.3.

Independent of the exact setup, we expect that systems with a larger lifetime form less massive black holes with generally smaller dimensionless spins, but more massive disks. However, no clear imprint of the eccentricity can be seen, taking into account the uncertainty of the numerical relativity simulations.

Ejecta and EM Counterparts

Ejecta:- In parallel to our discussion about the effect of numerical errors and grid resolutions on remnant lifetime, we find that clear quantitative statements about the exact ejecta mass cannot be made and the discussion should just be seen as qualitative. This is often the case for computations of ejecta masses using full 3D NR simulations. Even though simulation methods are continually being improved and simulations are achieving better and better accuracies, the quantification of ejecta material is still challenging and results come with large error bars. It is well known in the NR community that the accuracy of the NR data for quantities such as the unbound mass and kinetic energy have uncertainties which range between $\sim$10% up to even $\sim$100%; see e.g., Appendix A of (Hotokezaka et al., 2013b; Shibata et al., 2017) and (Abbott et al., 2017a; Dietrich et al., 2017d) for more discussions. Even though there are large uncertainties in the predictions for the ejecta masses, it nevertheless is useful to understand at least qualitatively the dynamical ejecta mechanisms for eccentric binaries.

Table 4.3 lists the ejecta properties for all the setups computed using the two methods as described in Appendix A, where $M_{\mathrm{ej}}^{\mathcal{V}}$ denotes the volume integrated ejecta mass computed using Eq. (A.2) and $M_{\mathrm{ej}}^{\mathcal{S}}$ the ejecta mass computed via Eq. (A.4) i.e., the method of integrating the flux of unbound matter through coordinate spheres.

A good agreement is found between the two ejecta mass estimates, with differences $\lesssim$11%. The ejecta mechanism for highly eccentric BNS mergers is shown in Fig. 4.4 considering one setup.

Although we do not obtain clean convergence for the estimates of the unbound matter with increasing resolution, our results are in good agreement with the few comparable results available in the literature (East et al., 2012, 2016b,a; Radice et al., 2016; Stephens et al., 2011). Specifically, $\sim \mathcal{O}(10^{-2})\ M_\odot$ of matter can be ejected at the merger. This is slightly more than in the quasi-circular case for the SLy binaries, and about an order of magnitude more for the MS1b binaries. In our simulations tidal tail ejecta are more prominent compared to shock-heated ejecta or ejecta due to the redistribution of angular momentum in the postmerger remnant. Interestingly, another source for small amounts of unbound matter is grazing close encounters before the merger cf. first and second columns of Fig. 4.4. As the stars undergo more frequent encounters, the unbound matter increases from $\mathcal{O}(10^{-4})M_\odot$ to $\mathcal{O}(10^{-3})M_\odot$ until merger. Overall, the unbound material at the merger $[\mathcal{O}(10^{-3})M_\odot - \mathcal{O}(10^{-2})M_\odot]$ is found to be ejected as a mildly relativistic and mildly isotropic outflow with the velocities $\sim 6 - 15\%$ of the speed of light. However, considering the difference among eccentric setups with fixed initial separation, no strong correlation between the exact eccentricity and the ejected mass is visible for all the configurations except the ones with SLy EOS and no spin.

EM Counterparts:- Following Dietrich et al. (2017b,c) and as described in a bit more detail in (Chaurasia et al., 2018), we compute order-of-magnitude estimates, see Table 4.4, for possible electromagnetic counterparts to the merger of the eccentric binary neutron stars studied in this work. Considering EM transients, we find compatible results for quasi-circular and eccentric BNS mergers. In general, the considered configurations will produce kilonovae with luminosities between $10^{39} - 10^{42}$ erg s^{-1} over a time ranging from a few days to two weeks after the merger. On the other hand, the radio flares will have the largest fluence at $t^{\rm radio}_{\rm peak}$ $\sim \mathcal{O}(\text{years})$, similar to equivalent quasi-circular cases. Furthermore, since the EM transients depend on the amount and properties of the ejecta, they show similar trends considering the dependence on initial eccentricity of the setups.

TABLE 4.4: Properties of electromagnetic counterparts and post-merger. The columns refer to: the name of the configuration, the time in which the peak in the near infrared occurs $t^{\rm NIR}_{\rm peak}$, the corresponding peak luminosity $L^{\rm NIR}_{\rm peak}$, the temperature at this time $T^{\rm NIR}_{\rm peak}$, the time of peak in the radio band $t^{\rm radio}_{\rm peak}$, and the corresponding radio fluence (the flux density per unit frequency) $F^{\nu \rm radio}_{\rm peak}$ at 100 Mpc, the dimensionless merger frequency $M\omega_{\rm mrg}$, the dimensionful merger frequency $f_{\rm mrg}$ (in kHz), and the dominant postmerger frequencies extracted from the $(2,1)$, $(2,2)$, and $(3,3)$ modes. We mark "$-$" for cases where the frequencies could not be extracted properly, mostly due to the shorter lifetime of the HMNS. We present results for all resolutions. Table adapted from (Chaurasia et al., 2018).

Name	$t^{\rm NIR}_{\rm peak}$ [days]	$L^{\rm NIR}_{\rm peak}$ [10^{40}erg s^{-1}]	$T^{\rm NIR}_{\rm peak}$ [10^3K]	$t^{\rm radio}_{\rm peak}$ [years]	$F^{\nu \rm radio}_{\rm peak}$ [mJy]	$M\omega_{\rm mrg}$	$f_{\rm mrg}$ [kHz]	f_1 [kHz]	f_2 [kHz]	f_3 [kHz]
SLy$-e0.40^{00}-$R2	5.4	4.5	1.9	15.7	0.860	0.153	1.83	$-$	3.51	$-$
SLy$-e0.45^{00}-$R1	5.4	4.4	1.9	10.2	0.208	0.149	1.78	$-$	3.45	$-$
SLy$-e0.45^{00}-$R2	3.8	3.7	2.0	6.8	0.097	0.165	1.97	$-$	3.64	$-$
SLy$-e0.45^{00}-$R3	4.9	5.0	1.9	6.9	0.222	0.156	1.87	1.77	3.54	5.33
SLy$-e0.45^{00}-$R4	3.6	4.3	2.0	6.1	0.251	0.165	1.97	$-$	3.66	$-$
SLy$-e0.50^{00}-$R1	5.0	2.2	2.3	12.9	0.003	0.158	1.89	1.78	3.56	$-$
SLy$-e0.50^{00}-$R2	2.8	2.5	2.4	6.0	0.019	0.167	1.99	1.86	3.69	5.53
SLy$-e0.50^{00}-$R3	6.0	3.7	1.9	18.1	0.162	0.160	1.91	$-$	$-$	$-$
SLy$-e0.50^{00}-$R4	2.1	2.4	2.5	4.7	0.024	0.158	1.89	$-$	3.47	$-$
SLy$-e0.60^{00}-$R2	1.7	2.2	2.7	3.9	0.025	0.151	1.81	1.78	3.56	5.49
SLy$-e0.40^{\uparrow\uparrow}-$R2	4.5	4.4	1.9	7.5	0.184	0.152	1.82	1.78	3.54	$-$
SLy$-e0.45^{\uparrow\uparrow}-$R1	4.0	3.1	2.2	8.1	0.032	0.140	1.67	1.81	3.45	$-$
SLy$-e0.45^{\uparrow\uparrow}-$R2	2.2	2.1	2.6	5.5	0.014	0.169	2.01	$-$	3.46	5.17
SLy$-e0.45^{\uparrow\uparrow}-$R3	3.1	3.7	2.1	5.6	0.156	0.177	2.12	$-$	3.52	$-$
SLy$-e0.45^{\uparrow\uparrow}-$R4	3.3	2.8	2.3	7.4	0.034	0.178	2.12	1.80	3.62	5.43
SLy$-e0.50^{\uparrow\uparrow}-$R2	3.7	2.5	2.3	8.8	0.012	0.157	1.87	1.87	3.72	5.62
SLy$-e0.60^{\uparrow\uparrow}-$R2	4.1	3.6	2.1	7.3	0.063	0.139	1.65	1.72	3.47	5.17
MS1b$-e0.45^{00}-$R2	5.2	2.6	2.2	13.2	0.011	0.116	1.36	1.07	2.06	3.16
MS1b$-e0.50^{00}-$R2	6.1	2.9	2.1	14.0	0.013	0.112	1.32	1.05	2.11	3.16
MS1b$-e0.60^{00}-$R2	2.4	2.1	2.6	6.0	0.013	0.112	1.32	1.05	2.11	3.16
MS1b$-e0.45^{\uparrow\uparrow}-$R2	5.4	3.8	2.0	10.5	0.068	0.128	1.50	1.08	2.15	3.21
MS1b$-e0.50^{\uparrow\uparrow}-$R2	4.2	2.7	2.2	9.2	0.014	0.126	1.48	1.07	2.17	3.12
MS1b$-e0.60^{\uparrow\uparrow}-$R2	7.5	5.0	1.7	12.1	0.149	0.106	1.25	1.10	2.17	3.24

4.4 Gravitational Waves

Gravitational Waves and metric multipoles are extracted following Brügmann et al. (2008). The multipoles, $\ell = m = 2$, of the GWs extracted at $r = 900M_\odot$ are shown in Fig. 4.6 for the configurations employing SLy EOS and no spin. The metric multipoles $rh_{\ell m}$ are reconstructed from the curvature multipoles[3] $r\Psi^4_{\ell m}$ using the

---

[3] Note that the GW strain h and the Weyl-Scalar Ψ_4 are related as $\Psi_4 = \ddot{h}$ and therefore to obtain h one needs to perform a double integration.

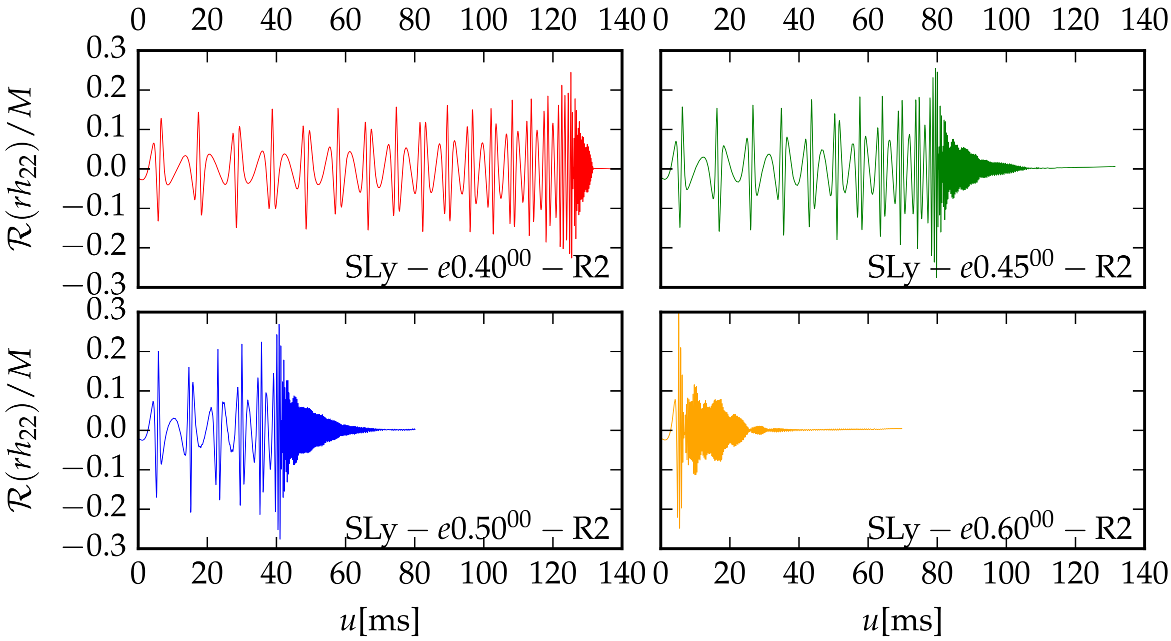

FIGURE 4.6: Real part of the (2,2) mode of the gravitational wave strain rh vs. the retarded time u. The color code refers to Fig. 4.2 and corresponds to different eccentricities. See, e.g., (Hinder et al., 2018) for eccentric BBH waveforms, for comparison (albeit for smaller eccentricities). Adapted from (Chaurasia et al., 2018).

fixed frequency integration of Reisswig et al. (2011). For this, the low-frequency cutoff is set to be half the initial GW frequency.

The gravitational waveforms for highly eccentric binaries significantly differ from the classical chirp signal of quasi-circular inspirals with its slowly but monotonically increasing amplitude and frequency, cf. (Dudi et al., 2018, Fig. 1) where a hybrid waveform for a similar mass and EOS NSs is shown. On highly eccentric orbits, one of the interesting features is that, each encounter of the stars leads to a burst of GW radiation. In Fig. 4.6, one can see that the usual oscillations in the strain at twice the orbital frequency are modulated by an oscillating envelope with a frequency lower than the orbital frequency, corresponding to apsidal precession of the pericenter.

A notable feature for BNSs on eccentric orbits is the quasinormal mode oscillations of the NSs. Periastron encounters in BNSs and BHNS on eccentric orbits lead to tidal interactions that can excite oscillations of the star(s), which in turn generate their own characteristic GW signal, see (Chirenti et al., 2017; Kokkotas et al., 1995; Parisi et al., 2018; Turner, 1977; Yang et al., 2018). These oscillations are superposed on the GW signal from the binary's orbital motion. While the NS oscillations are

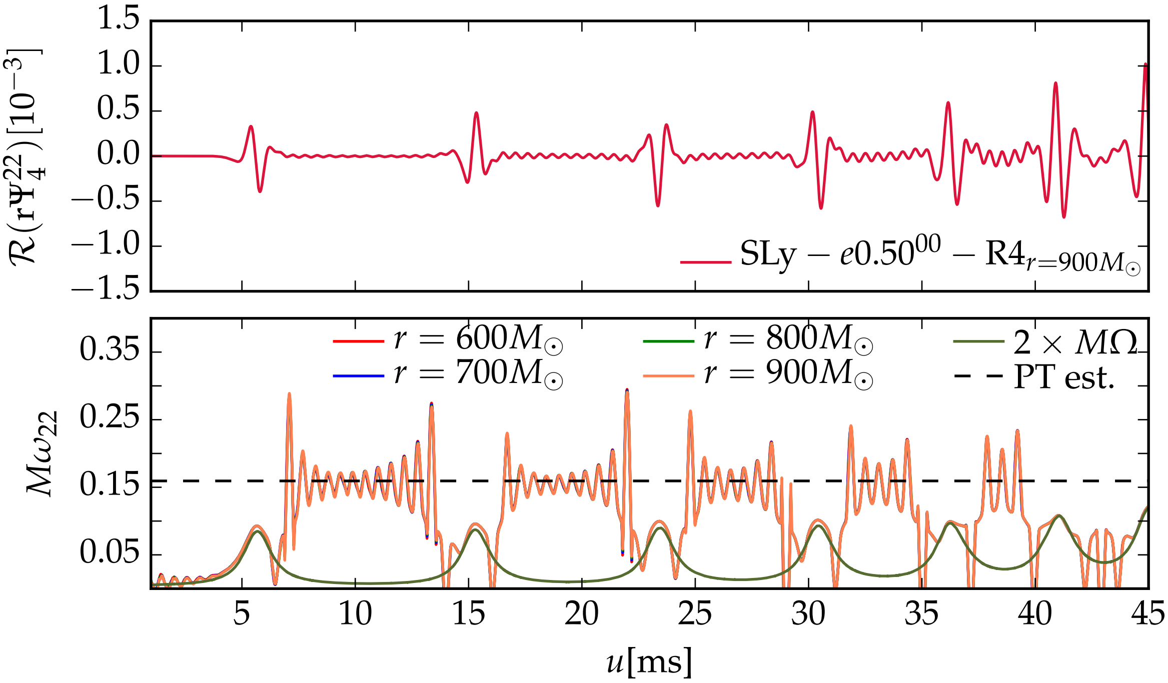

FIGURE 4.7: $r\Psi_4^{22}$ extracted at $r = 900M_\odot$ and instantaneous GW frequency $M\omega_{22}$ computed from the phase of $r\Psi_4^{22}$ (note that the curves at different extraction radii are coincident) plotted alongside $2 \times M\Omega$ as computed from the coordinate tracks of the NSs, both for the inspiral part of the SLy$-e0.50^{00}$ − R4 case. We find a good agreement for the relation $M\omega_{22} = 2 \times M\Omega$ and similar results hold for all the other cases. The higher frequency in-between the periastron encounters correspond to the quasinormal mode excitations of the NSs. We also plot the perturbation theory (PT) estimate for the f-mode frequency as a black dashed line. Adapted from (Chaurasia et al., 2018).

hardly visible in the metric multipole rh_{22}, they are evident in the curvature multipoles.

In Fig. 4.7, we plot the (2,2) mode of $r\Psi_4$ and the corresponding instantaneous GW frequency for the SLy$-e0.50^{00}$ − R4 case, focusing on the inspiral part. The figure also shows consistency of the extracted GW signals at different extraction radii, and in general other quantities extracted at finite radii from the simulated BNS system. In the lower panel of Fig. 4.7, we find that the influence of finite radius extraction of the GWs is negligible. Therefore, no radius extrapolation to compensate for the finite radius extraction (Bernuzzi et al., 2016a) is employed. It is reassuring that the GW frequency computed from the phase of the GWs matches twice the orbital frequency computed from the star trajectories during close encounters. Furthermore, comparing with the plot of the instantaneous GW frequency for eccentric BBHs in (Hinder et al., 2018, Fig. 2), we find for the BBH case there is no frequency higher than twice the orbital frequency whereas for the BNS case we find a much

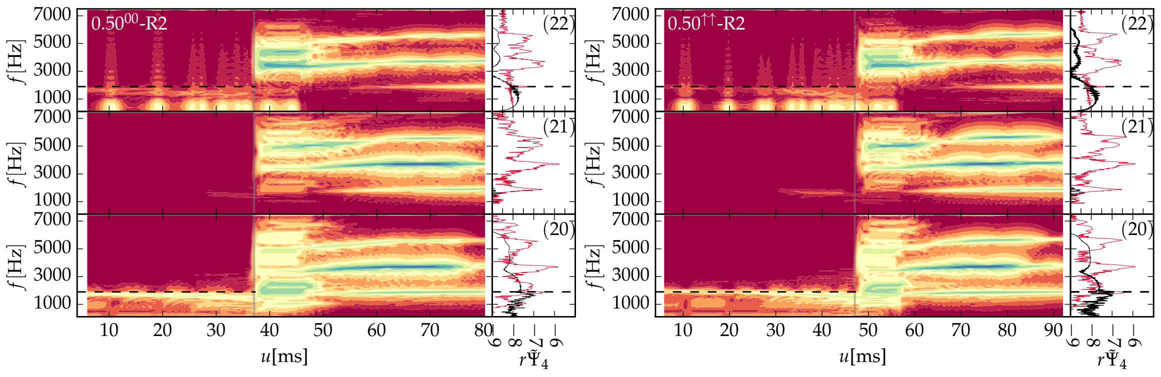

(A) (B)

FIGURE 4.8: **(A)**: Spectrogram (left) and PSD (right) of the curvature scalar $r\Psi_4$ for the SLy$-e0.50^{00}$ $-$ R2 configuration. The labels in the right panel plot refer to the (22), (21), and (20) modes of the curvature scalar. The black dashed line marks the PT estimate of the f-mode frequency and the gray line marks the moment of merger. The PSD is split into a part before the moment of merger (black) and a part after the merger (crimson). **(B)**: Similar to **(A)** but for the SLy$-e0.50^{\uparrow\uparrow}-$R2 configuration. The black dashed line marks the PT estimate of the f-mode frequency for *nonspinning* stars and the gray line marks the moment of merger. Adapted from (Chaurasia et al., 2018).

higher frequency due to the f-mode oscillations of the stars.

4.5 *f*-mode Oscillations

Figure 4.8a and Fig. 4.8b (left panels) show the (normalized) spectrogram (as described in Appendix A) for SLy$-e0.50^{00}$ $-$ R2 and SLy$-e0.50^{\uparrow\uparrow}$ $-$ R2, respectively. The right panels show the power spectral density (PSD) for the premerger (black) and postmerger (crimson) phases as different colors for the individual modes. The color bar in the spectrogram goes from red to blue and is given in arbitrary units, since we are only interested in the frequencies and the relative strength.

During the inspiral one observes discrete GW bursts present in the $(2,2)$ mode. This is in contrast to the typical chirp signal for the quasi-circular orbits, where the frequency and the amplitude increase monotonically over time, cf. (Dietrich et al., 2017b, Fig. 12). We also find a low power, but higher frequency region (1.5 kHz - 2 kHz) distinct from the inspiral burst signals. Such a frequency region is prominent for cases where the NSs' distance decreases to values as small as 40km-60km (cf. Fig. 4.3) during the periastron encounters.

The matter mode excitations can be reliably confirmed by studying the spectra of the $(2,0)$ fluid mode excitations. For BNS (and BHNS) in eccentric orbits, the

$(2,0)$ fluid mode is expected to be excited as the stars undergo periastron passage (see, e.g., the Newtonian calculations by Yang et al. (2018)). However, the spectrogram in the bottom panel of Fig. 4.8a for the $(2,0)$ curvature scalar mode, where a relatively high power signal is visible at $\sim$ 1.8kHz during the inspiral phase is accounted almost entirely by mode-mixing from (2,±2) modes, as we will see in the following discussion. Note that for the current set of simulations presented in this thesis we do not have the 3D data which is required for studying the fluid mode oscillations and therefore such an analysis is delayed to future study.

Perturbation theory estimate for f-mode frequency:- We compute the perturbation theory (PT) estimate of the f-mode excitation frequency for the SLy EOS with no spin of the NSs using the f-Love relation from (Chan et al., 2014),[4] obtaining an f-mode frequency of 1.89 kHz. As visible in the spectrogram, Fig. 4.8a, there is good agreement between the NS oscillation frequency from the simulation and the PT estimate of the f-mode frequency (horizontal black dashed line). Some of the differences between the PT estimate and the spectrogram are attributable to the gravitational redshift due to the star's companion, as discussed below, while others are due to the relatively low resolution of the simulation (R2): The f-mode frequency observed in the simulations increases with resolution.

In the spinning case, we find in Fig. 4.8b that the bright area near 1.8kHz in the $(2,2)$ and the $(2,0)$ mode in Fig. 4.8a for the nonspinning case is shifted to slightly higher frequencies. Notice that the dashed line in both figures shows the PT estimate for the nonspinning configuration for easier comparison. Overall, we find similar results for the simulations performed at different resolutions for the same configurations; see Sec. 4.6.

To obtain a PT estimate for the f-mode oscillation frequency of spinning configurations, we follow Doneva et al. (2013). Since we find an increase in the f-mode frequency with spin, we want to consider the $\ell = 2$, $m = -2$ mode. Note that since the stellar modes describe real quantities, e.g., the perturbations to the star's density, the $m = -2$ mode of the star will have an angular dependence of $e^{\pm 2i\phi}$, and thus its radiation will have a significant overlap with the $(2,2)$ spin-(-2)-weighted spherical harmonic mode. Additionally, it is expected that this mode will be excited most strongly in highly eccentric binaries, as discussed in (Yang et al., 2018), using Newtonian calculations. For our case, the NSs with SLy EOS are spinning at $f_\star \simeq 191$Hz. Since the Doneva et al. results relate the f-mode frequency of a spinning star to that of a nonspinning star with the same central density, we first note that a nonspinning SLy star with the same central density as the spinning star has a mass of $1.42 M_\odot$ and thus a f-mode frequency of $f^{\text{no-Cowling}}_{\text{nonspinning}} = 1.93$ kHz (obtained using the f-Love relation from (Chan et al., 2014)). We then use Eq. (24) in Doneva et al. (2013), which gives[5]

---

[4] We use the publicly available TOV solver of Bernuzzi et al. (2015) and Bernuzzi et al., IHES EOB code to compute the Love number.

$$\frac{\omega^{\text{corot, Cowling}}_{\text{spinning}}}{\omega^{\text{Cowling}}_{\text{nonspinning}}} = 1 - 0.235\frac{\Omega_\star}{\Omega_{\text{K}}} - 0.358\left(\frac{\Omega_\star}{\Omega_{\text{K}}}\right)^2. \tag{4.5}$$

Here $\omega^{\text{corot, Cowling}}_{\text{spinning}} = \omega^{\text{Cowling}}_{\text{spinning}} - 2\Omega_\star$ is the mode's angular frequency in the frame corotating with the star, where $\omega^{\text{Cowling}}_{\text{spinning}}$ is the mode's angular frequency in the inertial frame of an external observer and $\Omega_\star = 2\pi f_\star$ is the angular velocity of the star. We have $\Omega_\star/\Omega_{\text{K}} = 0.157$ for these SLy stars, where Ω_{K} is the Kepler angular velocity for an SLy star with the same central density as the stars we consider (computed using (LORENE code)). Additionally, we have used superscripts of "Cowling" to denote that the expression in Doneva et al. is derived using the Cowling approximation.

The Cowling approximation generally overestimates the f-mode frequency, as illustrated in, e.g., Fig. 5 in (Zink et al., 2010). However, this figure shows that this overestimate is independent of spin (to a good approximation, particularly for the relatively small spins we are considering). Thus, we can use the Cowling approximation offset of $\Delta f_{\text{Cowling}} \simeq 500$ Hz for a $1.42 M_\odot$ nonspinning star obtained from Fig. 8 in (Chirenti et al., 2015) to correct for the effect of the approximation (which is, however, only a $\sim 1\%$ effect on the final value). Specifically, if we write $\omega^{\text{corot, Cowling}}_{\text{spinning}} =: k\omega^{\text{Cowling}}_{\text{nonspinning}}$ (so $k = 0.95$ here), we have

$$\omega^{f\text{-mode}}_{\text{spinning}} = k\omega^{f\text{-mode}}_{\text{nonspinning}} + 2\pi(k-1)\Delta f_{\text{Cowling}} + 2\Omega_\star. \tag{4.6}$$

This procedure gives a f-mode frequency of 2.20 kHz.

---

[5] Note that the typo (i.e. the pre-factor in the last term) in (Chaurasia et al., 2018, Eq. (13)) and the superscript "Cowling" in the expression of f-mode frequency computed from the universal relation is fixed here. However, in the computations the correct factor was used.

Gravitationally redshifted f-mode frequency:- The redshifted PT estimate of the frequency is $\sim 5\%$ larger than the frequency observed in the spectrogram or the instantaneous frequency we compute using the method given below. One would need the spin of the stars to be $\sim 40\%$ smaller than its actual value in order for the instantaneous frequency estimated from the waveform to agree with the redshifted PT frequency. Such a large difference in spin is well outside the maximum expected difference between the true value of the spin and the one estimated from the inputs to the initial data construction, as discussed by Dietrich et al. (2017c). (Note that the spin we estimate from the initial data inputs agrees well with the one we compute in the early part of the inspiral using the quasilocal computation described by Dietrich et al. (2017c).) Thus, we are not sure of the source of the discrepancy between the PT estimate and the frequency of the oscillations observed in the simulation.[6] Additionally, there do not appear to be any other $m = \pm 2$ modes that would occur at the observed frequency.

In order to see the effects of the redshift, we can examine the instantaneous f-mode frequency we obtain from the $(2,2)$ mode after removing the orbital contribution (as described in Appendix A). This is shown in Fig. 4.9. (Since $\mu_{2,2;2,2}$ is real, accounting for mode mixing does not change the instantaneous frequency here.) Here we estimate this redshift using the stars' tracks and the leading PN expression of $\omega^{\text{redshifted}}_{f\text{-mode}} = (1 - M^B/d)\omega_{f\text{-mode}}$ (see, e.g., Krisher (1993)), where d is the separation of the two stars, noting that it suffices to consider only star A, as the binary is symmetric.[7]

The remaining oscillations of the instantaneous frequency are likely due to a combination of the effects mentioned below in the discussion of the $(2,0)$ mode amplitude, as well as the lack of removal of the $(2,2) \leftrightarrow (2,-2)$ mixing (which does not seem straightforward to remove), and possibly also mixing in of intrinsic

---

[6] A potential source of the disagreement might be the change in the external gravitomagnetic fields of the NSs due to the intrinsic NS spins (Steinhoff et al., 2016). However, this effect does not seem large enough to account for the observed discrepancy.

[7] Note that Krisher (1993) calculates higher PN corrections, through $O(c^{-4})$, including effects of the star's velocity. [See Eq. (4.1), noting that $\beta = \gamma = 1$ and the other parameterized PN parameters vanish in general relativity.] The contributions from the velocity are all negligible here (producing almost indistinguishable curves on this plot), which is why we do not include them. The leading $O(v)$ effect from the star's velocity only affects the phase of the $(2,2)$ mode of the waveform on the timescale of the orbit, and thus does not affect the f-mode signal we consider here. The star's velocity is small enough that the $O(v^2)$ terms produce differences of $\sim 1\%$. We do not consider the additional corrections involving the gravitational potential, as they are expected to be small in the region between periastra. Moreover, it is unclear if adding higher corrections would improve the accuracy of the predictions, as we are not evaluating the expression using PN coordinates.

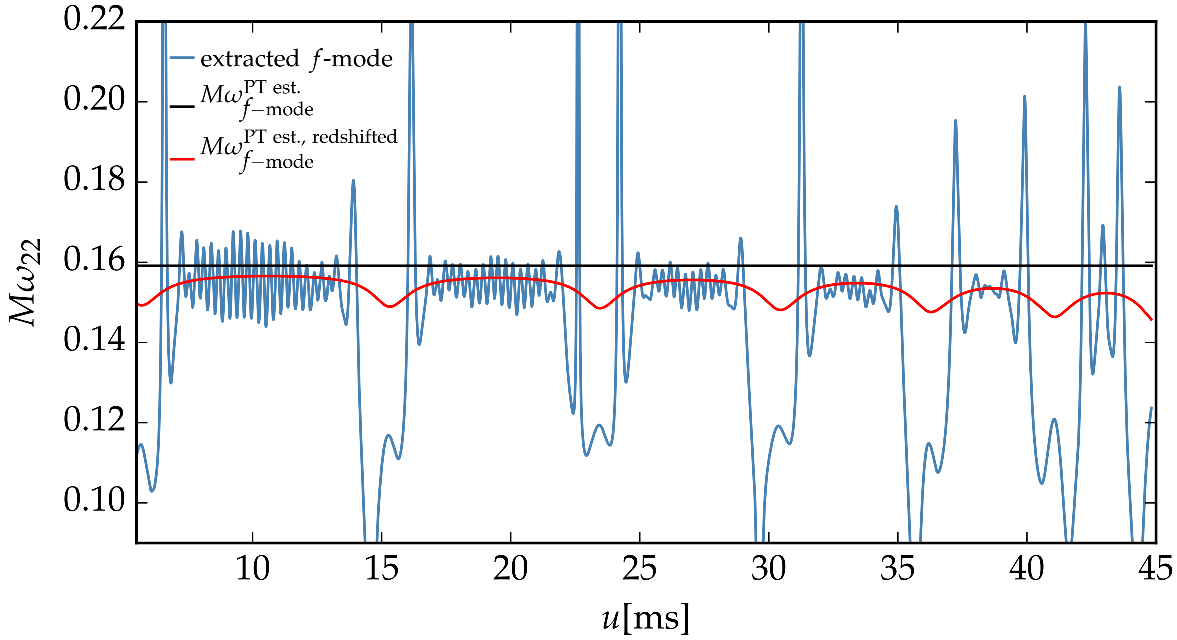

FIGURE 4.9: Instantaneous frequency of $\Psi_{2,2}^{4,f\text{-mode}}$ for SLy$-e0.50^{00}-$R4, compared to the prediction of the f-mode frequency of an isolated star, as well as the f-mode frequency including the estimated gravitational redshift due to the star's companion. These curves should only be compared away from the periastron bursts. Adapted from (Chaurasia et al., 2018).

higher-ℓ modes.

Removing displacement-induced mode mixing in the GW signal from tidally-induced oscillations:- We now want to apply the displacement-induced mode mixing analysis from Appendix A to obtain the dominant $(2, \pm 2)$ modes of the f-mode oscillations that would be extracted if the stars were at rest at the origin. We will then use the amplitude of these modes to estimate the energy stored in the f-mode oscillations.

If we just have a $(2, \pm 2)$ intrinsic excitation of the stars, we will also obtain a purely real contribution to the $(2, 0)$ mode from this intrinsic excitation due to the mode mixing. This contribution is purely real because the extracted $(2, \pm 2)$ modes have the usual relation for nonprecessing binaries of $\Psi^4_{2,-2} = \left(\Psi^4_{2,2}\right)^*$ and we have $\mu_{2,-2;2,-2} = \mu_{2,2;2,2}$ and $\mu_{2,-2;2,0} = \mu^*_{2,2;2,0}$, so the contribution to the $(2, 0)$ mode from mode mixing is

$$\begin{aligned}\Psi^{4,\text{mixing from }2,\pm2}_{2,0} &= \Psi^{4,f\text{-mode}}_{2,2}\mu_{2,2;2,0}/\mu_{2,2;2,2}\\ &\quad+\Psi^{4,f\text{-mode}}_{2,-2}\mu_{2,-2;2,0}/\mu_{2,-2;2,-2}\\ &= 2\mathcal{R}(\Psi^{4,f\text{-mode}}_{2,2}\mu_{2,2;2,0}/\mu_{2,2;2,2}).\end{aligned} \tag{4.7}$$

In fact, we find that if we compute the mixing coefficients using the tracks to give the positions of the stars, the mixing from the $(2,\pm2)$ modes appears to account for all of the f-mode signal we extract in the $(2,0)$ mode, as illustrated in Fig. 4.10. [We use the PT computation of the f-mode frequency used in the previous-to-previous subsection. We also checked that we find the expected contributions to the $(3,\pm2)$ and $(3,0)$ modes due to displacement-induced mode mixing from the $(2,\pm2)$ modes.] The slight deviations in amplitude are likely due to the approximation of using the coordinate tracks to compute the mixing coefficients and residual contributions from the orbital motion that are not removed by our simple moving average procedure to separate the orbital and f-mode signals. Additionally, while we expect a contribution to the $(2,0)$ mode from the binary's orbital motion, we find that any such contribution is considerably smaller than the f-mode signal that arises from displacement-induced mode mixing.

We can also use the Schwarzschild tortoise coordinate computed from the tracks instead of the tracks themselves to compute the retarded time, using the system's ADM mass as the Schwarzschild mass. This is analogous to the procedure used for the extraction of gravitational waves, as described in Sec. V of Dietrich et al. (2017b), though it is less well-motivated here in the stronger-field regime, and we simply consider it to give a comparison for the results computed using the tracks themselves. If we use the tortoise coordinate, then we obtain closer agreement in the amplitude of the mixed contribution to the $(2,0)$ mode and the extracted contribution, but we also obtain intrinsic $(2,\pm2)$ f-mode signals that are considerably larger and look rather unphysical, since their amplitude increases towards apastron. We thus chose to present the results with the plain coordinate track computation.

Energy estimate of the NS oscillations:- In order to give an order of magnitude estimate of the energy stored in the NS oscillations, we assume that it decays exponentially due to the emission of GWs. We then compute the f-mode GW damping time and use it to infer the energy stored in the NS oscillations by computing the

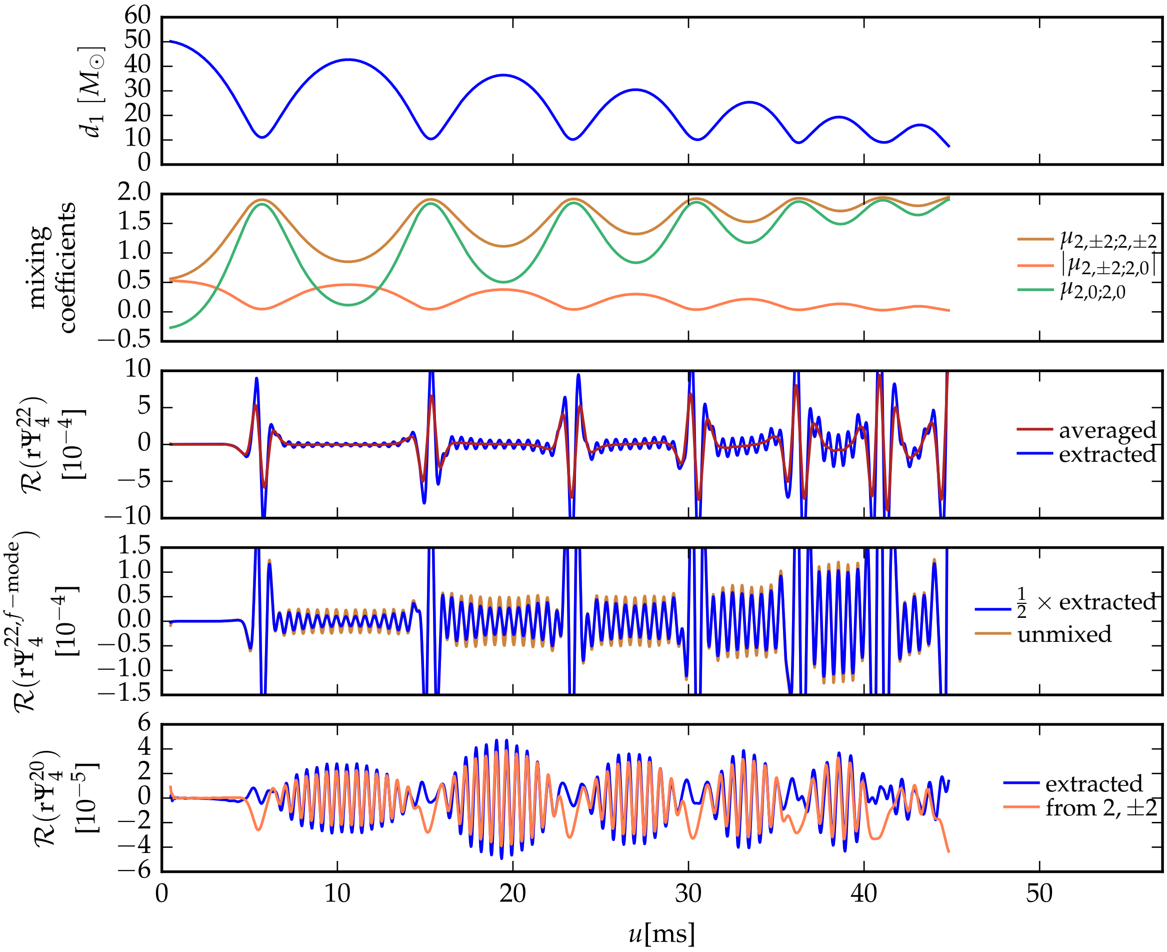

FIGURE 4.10: Illustration of the effects of displacement-induced mode mixing on the waveforms extracted from $\text{SLy}-e0.50^{00}-\text{R4}$: Coordinate distance from star 1 to the origin *(top)*; mode mixing coefficients *(second-from-top)* ($|\mu_{2,\pm2;2,\mp2}|$ is almost indistinguishable from 0 at this scale, so we do not show it); illustrating the averaging used to separate the f-mode and orbital signals *(third-from-top)*; comparing the full mode mixing calculation of the intrinsic f-mode contribution to the real part of the $(2,2)$ mode from a single star to the naive calculation of taking half of the extracted mode *(second-from-bottom)* (the result for the imaginary part is exactly analogous); comparing the contribution to the real part of the $(2,0)$ mode from mode mixing to that extracted from the evolution of the binary *(bottom)* (the imaginary part vanishes). In all cases, the approximations used to compute the mode mixing are only valid during the inter-burst f-mode oscillations, and the predictions of the mode mixing calculation for the periastron bursts should not be considered. Adapted from (Chaurasia et al., 2018).

energy radiated in GWs. In particular, we compute the f-mode angular frequency using the same f-Love relation from Eq. (3.5) in (Chan et al., 2014) used previously, which gives an f-mode frequency of 1.40 kHz for the nonspinning MS1b stars. The damping time $\tau_{f\text{-mode}}$ (the inverse of the imaginary part of the mode's angular frequency) is computed using Eq. (20) in (Lioutas et al., 2018), which gives it in terms of the star's mass and radius. We obtain damping times of 0.186 s and 0.317 s, respectively, for the nonspinning SLy and MS1b stars.

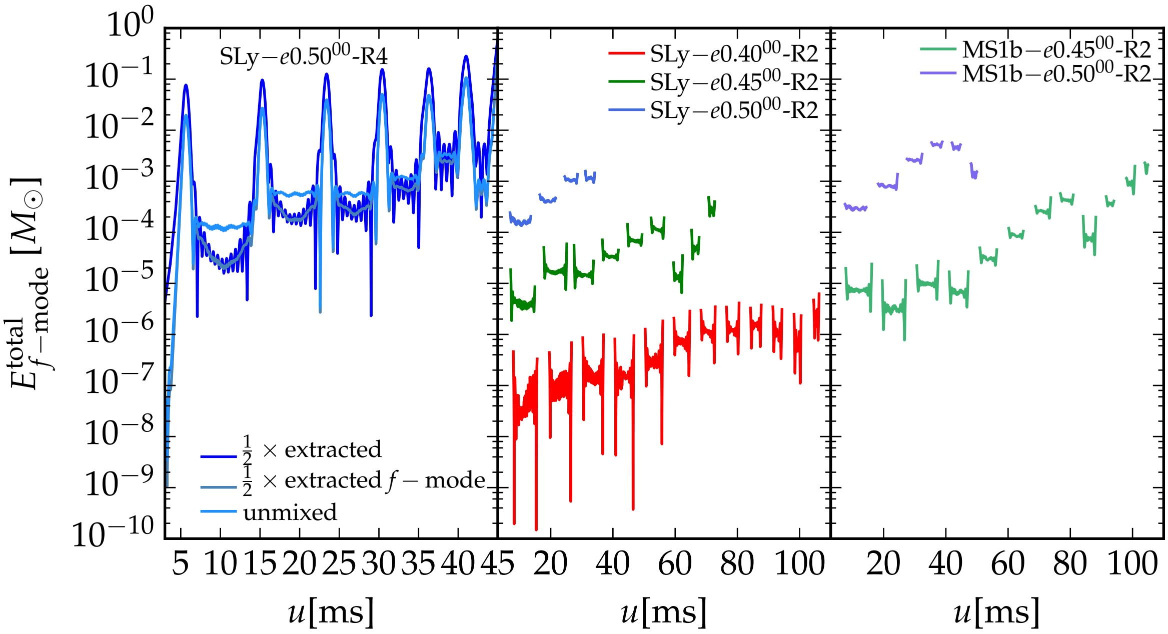

FIGURE 4.11: Estimate of the energy stored in f-mode oscillations as a function of the retarded time. *(Left panel):* Comparison of the results after accounting for displacement-induced mode mixing to those obtained using half the extracted signal, both plain (i.e. the pure extracted signal), and with only the f-mode part for SLy$-e0.50^{00}-$R4. The energy estimate is only valid in the times between the periastron bursts. *(Middle and right panels):* The energy estimate computed accounting for displacement-induced mode mixing for the nonspinning SLy and MS1b cases that have multiple encounters before merger, considering the R2 resolutions for which we have data for the most eccentricities. In order to clarify these plots, we have excluded the portions of the traces that are close to the periastron bursts. Adapted from (Chaurasia et al., 2018).

We compute the energy radiated by using the intrinsic $(2, \pm 2)$ modes of an individual star computed in the previous subsection. Since the f-mode damping times are much longer than the time between periastra, we assume that the f-mode GW signal is exactly sinusoidal, with angular frequency $\omega_{f\text{-mode}}$ and has the same amplitude in both the $(2, 2)$ and $(2, -2)$ modes, by symmetry. We then use this to compute the antiderivative of Ψ_4 (by dividing by $\omega_{f\text{-mode}}$), which gives

$$\dot{E} \simeq \frac{1}{8\pi}\left(\frac{r|\Psi^{4,f\text{-mode}}_{2,2}|}{\omega_{f\text{-mode}}}\right)^2, \tag{4.8}$$

cf. Eq. (52) in (Brügmann et al., 2008). Now, the energy stored in the f-mode oscillation is $E_{f\text{-mode}}(t) = E^{\text{total}}_{f\text{-mode}} e^{-2t/\tau_{f\text{-mode}}}$. The factor of 2 arises because we are looking at the energy, which goes as the amplitude squared. Thus, we have a radiated energy of $\dot{E}_{\text{GW}} = -\dot{E}_{f\text{-mode}} \simeq (2/\tau_{f\text{-mode}})E^{\text{total}}_{f\text{-mode}}$, where we have evaluated this at $t = 0$, by the same argument about the length of the f-mode damping times compared to the time between periastra as above. This finally gives

$$E^{\text{total}}_{f\text{-mode}} \simeq \frac{\tau_{f\text{-mode}}}{16\pi} \left(\frac{r|\Psi^{4,f\text{-mode}}_{2,2}|}{\omega_{f\text{-mode}}} \right)^2 . \tag{4.9}$$

We plot the energy estimate as a function of time for the nonspinning cases in Fig. 4.11. (We do not include the spinning cases, since we found that the mode mixing removal was not working quite as well for them, likely because the estimate of the f-mode frequency is not sufficiently accurate.) We illustrate how removing the displacement-induced mode mixing is necessary to make an accurate energy estimate, and then compare the energy estimates for the different cases.

We find that the amount of energy stored in the f-mode oscillations increases with initial eccentricity, and is also larger for the MS1b stars than the SLy stars, at a fixed eccentricity. Both of these are to be expected, since the periaston separations decrease with increasing eccentricity, so the stars are experiencing larger tidal perturbations, and the MS1b stars are more tidally deformable than the SLy stars, so they will absorb more energy. We also find that the energy stored in the stars does not always increase monotonically with time, as would be expected, since the tidal perturbations of the stars may be close to out of phase with the already existing oscillations. This is also seen in the analytic calculations of Yang et al. (2018). (There is a particularly dramatic illustration of such an effect in Fig. 2 of Radice et al. (2016), though that paper suggests that it may be an artifact of the π symmetry imposed during the evolution.) The remaining time variation of the energy estimate in between periastron encounters is presumably due to the same effects discussed previously for the amplitude of the $(2, 0)$ mode from displacement-induced mode mixing and the instantaneous frequency of the f-mode signal. The energy estimates for the first few encounters are robust across resolutions, while the later ones differ more, since the later dynamics also differ between resolutions, as shown for the gravitational waveform in Sec. 4.6.

We find that the f-mode oscillations of the SLy stars store up to $\sim 10^{-3} M_{\odot}$ of energy in the $e = 0.5$ case. While $10^{-3} M_{\odot}$ is relatively small compared to some of the other energy scales in the problem (such as the binding energy of the star or the binary's initial orbital binding energy, which are on the order of 10^{-1} and $10^{-2} M_{\odot}$, respectively), it is a tremendous amount of energy, $\sim 10^{51}$ erg, comparable to the energy released in a supernova.

Furthermore, such energies will be sufficient to shatter the NSs' crust and release the elastic energy stored in these oscillations (cf. (Thompson et al., 1995) where they report $\sim 10^{46}$ erg to be stored in elastic energy). This will likely lead to flaring activity from milliseconds up to possibly a few seconds before merger (cf. Fig. 4.11). The signature could be similar to the resonance-induced cracking for quasi-circular inspirals proposed by Tsang et al. (2012), though through different mechanism and time scales. Such a cracking of the NS crust is reported as one possible explanation for sGRB precursors observed by Swift (Troja et al., 2010) and might also be visible for BNSs on eccentric orbits.

4.6 Convergence Study

To give some diagnostics for the accuracy of our simulations, we present a convergence study for the conservation of baryonic mass of the system, Fig. 4.12a, the ADM constraints, Fig. 4.12b, and the waveform, Fig. 4.13, for the SLy$-e0.50^{00}$ configuration. A detailed discussion about the convergence and accuracy of SGRID can be found in (Dietrich et al., 2015a; Tichy, 2009a) and for BAM in (Bernuzzi et al., 2012, 2016a; Dietrich et al., 2015b).

Mass conservation:- A detailed discussion about the mass conservation in BNS simulations with BAM was presented by Dietrich et al. (2015b). Here, we want to present the rest-mass conservation for at least one of our simulations. Figure 4.12a shows the mass conservation for the SLy$-e0.50^{00}$ configuration. It is clear that the mass conservation improves with increasing resolution. However, note that the merger itself happens at different times due to different numerical dissipation for different resolutions. Additionally, after the merger no considerable mass loss is present at higher resolutions (except for the cases where a BH forms, which is expected) and the difference to the initial mass stays below 0.6% for the lowest resolution simulation and below 0.01% for the highest resolution simulation.

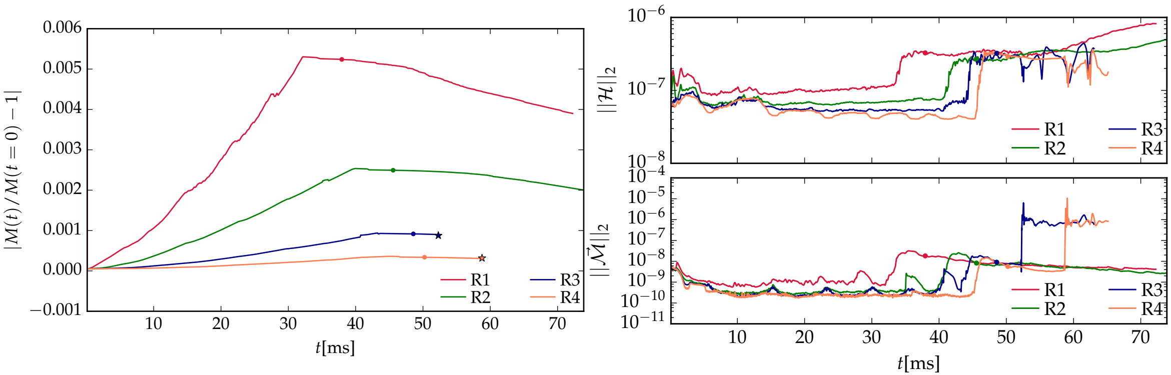

(A) Baryonic Mass Conservation

(B) ADM Constraints

FIGURE 4.12: **(A)**: Rest mass conservation of SLy$-e0.50^{00}$ case on refinement level $l = 1$. The panel shows the absolute error of the rescaled mass evolution of the baryonic mass. We mark the moment of merger as circles and the moment when a BH forms with a star. The error in the total mass stays below 0.6% for the lowest resolution and below 0.01% for the highest resolution over the entire evolution time. Mass conservation is not violated once a BH forms. **(B)**: ADM constraints for the SLy$-e0.50^{00}$ case. The upper panel shows the L^2 volume norm of the Hamiltonian constraint, $||\mathcal{H}||_2$. The lower panel shows the Euclidean norm of the L^2 volume norms of the Cartesian components of the momentum constraint, $||\vec{\mathcal{M}}||_2 = \sqrt{||\mathcal{M}^x||_2^2 + ||\mathcal{M}^y||_2^2 + ||\mathcal{M}^z||_2^2}$. The constraints are evaluated on refinement level 4 and are decreasing for increasing resolution during the inspiral of the neutron stars. Note that here we restrict our convergence analysis to the refinement level 4, cf. Tab. 4.1. This is needed since for the coarser refinement levels even the higher resolution setups are only barely able to resolve the star whereas for the coarser resolutions not a single point covers the NS leading to a nonconvergent behavior. We have filtered our data with an average filter to give a better visualization and reduce high frequency noise and mark the times of merger by circles. Adapted from (Chaurasia et al., 2018).

ADM constraints:- Since we use a free evolution scheme of the (3+1)-decomposed Einstein equations, we have to ensure that the Hamiltonian and the momentum constraints are fulfilled over the entire simulation. While we explicitly solve the constraints to obtain our initial data, the constraints are not solved during the simulation. Figure 4.12b shows the L^2 volume norm of the Hamiltonian constraint (top panel) and the L^2 volume norm of the square magnitude of the momentum constraint (bottom panel) during the simulation. We see that the constraints are well behaved for the entire duration of the numerical simulation. Oscillations during the inspiral are caused by the movement of inner refinement levels which follow the motion of the neutron stars. After merger those oscillations are absent since the stars stay near the center or only move with a small velocity compared to the inspiral.

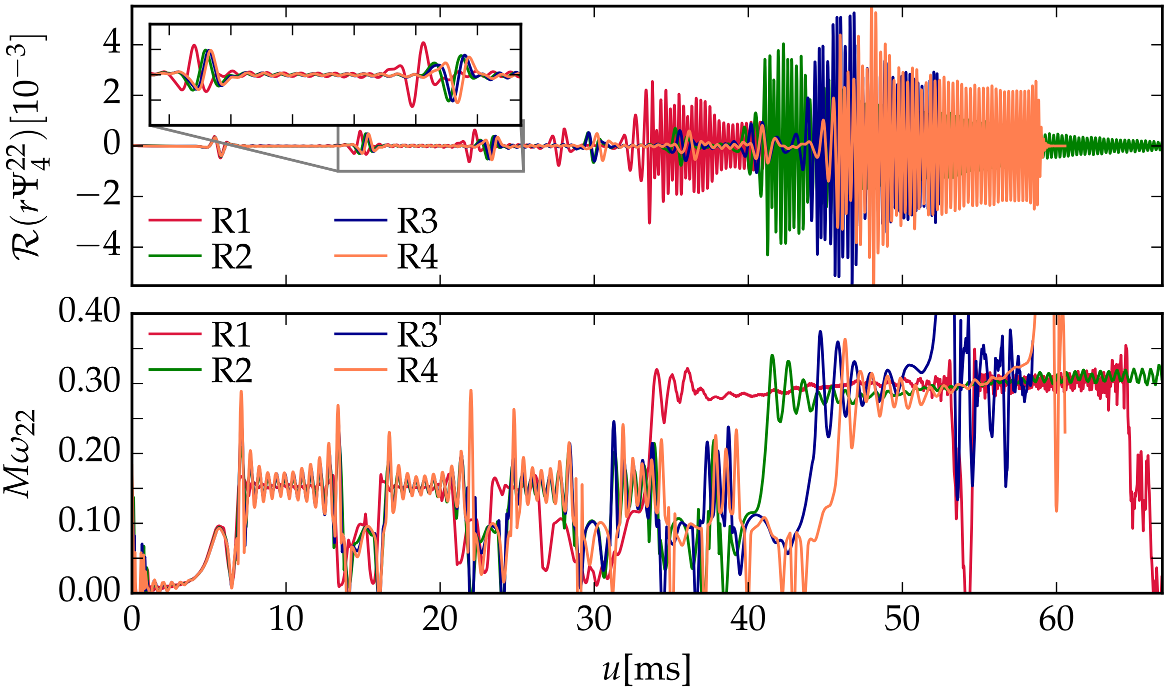

FIGURE 4.13: (*Top panel*): Real part of the curvature multipole $r\Psi_4^{22}$ for the SLy$-e0.50^{00}$ configuration for four different resolution, see Table 4.2. The inset figure shows two periastron encounters and the region in between where the f-mode oscillations are present. (*Bottom panel*): The instantaneous dimensionless frequency $M\omega_{22}$ computed from $r\Psi_4^{22}$. The plots show the robustness of the NS oscillations and the different evolution of the postmerger part. The merger times also vary depending on the resolution due to varying numerical dissipation, which is an inevitable numerical phenomenon for all simulations.

Waveform:- In order to estimate the convergence properties of the GW signal, we use the merger times for the SLy$-e0.50^{00}$ case with multiple resolutions (cf. Fig. 4.13).

Considering the merger times computed from the R1, R2, R3, and R4 resolutions, we obtain a convergence of order ~ 1.5. While this is an indicator that the simulations are in the convergent regime a more careful investigations, see e.g. (Bernuzzi et al., 2016a), is needed for a full error assessment. Nevertheless, our results show that the simulations can be used as first test beds once eccentric BNS waveform models become available. But in order to perform detailed waveform modelling and further reduce the uncertainty of our numerical results, even higher resolution simulations are the immediate need. These high resolution simulations will require large amounts of computational resources..

Chapter 5

Precessing Binary Neutron Stars

In this chapter we briefly present our work on the study of precessing BNS systems using full (3+1)D numerical relativity simulations with consistent initial data (Chaurasia et al., 2020). In these systems the NS spins are misaligned with respect to the orbital angular momentum of the system leading to a precessing motion of the entire orbital plane. In addition to the precession of the orbital plane the individual spins of the stars are expected to show nutation or precession of the NS spins.

In a large fraction of the studies done in numerical relativity concerning NSs, spins have been overlooked or have been treated unrealistically by assuming that the stars are tidally locked. Only in the recent years NR groups have performed simulations including NS spins, dropping the corotational assumption. Studies done using consistent initial data for configurations in which the individual NSs are spinning, are presented in (Bernuzzi et al., 2014a; Dietrich et al., 2015a, 2017c, 2018b; East et al., 2019; Most et al., 2019; Tsokaros et al., 2019). With respect to precessing NS binaries, the list of studies is even shorter (Dietrich et al., 2015a, 2018c; Tacik et al., 2015).

This chapter is structured as follows: Section 5.1 briefly describes the BNS configurations considered and the evolution scheme followed. In Sec. 5.2 we discuss the orbital motion of the precessing BNSs and the corresponding GWs. In Sec. 5.3 we study the conservative dynamics of the system. Finally, in Sec. 5.4 we present a short discussion about the ejecta from precessing systems.

5.1 Precessing Configurations & Evolution

The initial data for the precessing BNS systems presented in this chapter are constructed following the same strategy as described in Sec. 4.1. However, unlike the

TABLE 5.1: BNS configurations. The first column gives the configuration name and the next 5 columns provide the physical properties of the individual stars: the gravitational masses of the individual stars $M^{A,B}$, the baryonic masses of the individual stars $M_b^{A,B}$, the stars' dimensionless spins magnitude $\chi^{A,B}$ and their orientations $\hat{\chi}^A$ and $\hat{\chi}^B$. The last 4 columns give the residual eccentricity e, the initial GW frequency $M\omega_{22}^0$, the ADM mass $M_{\rm ADM}$, and the ADM angular momentum $J_{\rm ADM}$. The configurations were evolved with the resolutions of Table 5.2. The simulation data will be made available on the CoRe (2018) database in future.

Name	$M^{A,B}$	$M_b^{A,B}$	$\chi^{A,B}$	$\hat{\chi}^A$	$\hat{\chi}^B$	e	$M\omega_{22}^0$	$M_{\rm ADM}$	$J_{\rm ADM}$
SLy$^{(\uparrow\uparrow)}$	1.3505	1.4946	0.0955	(0,0,1)	(0,0,1)	0.00753	0.03405	2.6799	8.1939
SLy$^{(\nwarrow\nearrow)}$	1.3505	1.4946	0.0956	$\frac{(-1,0,1)}{\sqrt{2}}$	$\frac{(1,0,1)}{\sqrt{2}}$	0.00793	0.03406	2.6799	8.0993
SLy$^{(\nearrow\nearrow)}$	1.3505	1.4946	0.0955	$\frac{(1,0,1)}{\sqrt{2}}$	$\frac{(1,0,1)}{\sqrt{2}}$	0.00813	0.03406	2.6799	8.1020
SLy$^{(\leftarrow\rightarrow)}$	1.3505	1.4946	0.0955	(-1,0,0)	(1,0,0)	0.00922	0.03408	2.6799	7.8712
SLy$^{(\swarrow\searrow)}$	1.3505	1.4946	0.0956	$\frac{(-1,0,-1)}{\sqrt{2}}$	$\frac{(1,0,-1)}{\sqrt{2}}$	0.01083	0.03411	2.6799	7.6437
SLy$^{(\searrow\searrow)}$	1.3505	1.4946	0.0956	$\frac{(1,0,-1)}{\sqrt{2}}$	$\frac{(1,0,-1)}{\sqrt{2}}$	0.01194	0.03409	2.6799	7.6437
SLy$^{(\downarrow\downarrow)}$	1.3505	1.4946	0.0955	(0,0,-1)	(0,0,-1)	0.01197	0.03411	2.6799	7.5484

highly eccentric BNSs studied in the previous chapter, here the quasi-equilibrium configurations of binaries are constructed for BNSs on circular orbits, see Table 5.1.

We study BNSs with equal mass NSs having fixed rest masses (baryonic masses) of $M_b^{A,B} = 1.4946 M_\odot$. SLy EOS as described in Sec. 4.2 is used. The individual stars are spinning and have dimensionless spins $\chi^A = \chi^B \approx 0.096$. The simulated configurations differ in their spin orientation with respect to the orbital angular momentum direction of the system. The gravitational masses for the NSs in isolation are $M^{A,B} \simeq 1.35 M_\odot$, leading to a binary mass of $M \simeq 2.70 M_\odot$, see details in Table 5.1.

`BAM` code is used for evolving the initial data and we employ the Z4c formulation (Bernuzzi et al., 2010; Hilditch et al., 2013) of the Einstein equations for the evolution system instead of the BSSN formulation owing to better constraint propagation and damping properties of the former[1]. Slicing conditions employed are the same as in Chapter 4, namely, (1+log)-lapse and gamma-driver-shift conditions. Numerical fluxes for the general relativistic hydrodynamics system are constructed with a flux-splitting approach based on the local Lax-Friedrich flux. The reconstruction is performed with a fifth-order WENOZ algorithm (Borges et al., 2008) on the

---

[1] In the study of highly eccentric BNSs in the previous chapter it was found that the Z4c evolution system was unstable, giving rise to a blowup in the constraint violations at a later stage in the evolution. However, for quasi-circular cases this is not the case. Therefore, we used the BSSN system for evolutions of the highly eccentric systems. The cause of the instability could be due to the boundary conditions for the Z4c system being available for curved outer boundaries whereas we were using box grids with straight boundaries.

TABLE 5.2: Grid configurations. The columns refer to: the resolution name, the number of levels L, the number of moving box levels L_{mv}, the number of points in the non-moving boxes n, the number of points in the moving boxes n_{mv}, the grid spacing in the finest level h_6 covering the NS diameter, the grid spacing in the coarsest level h_0, and the outer boundary position R_0. The grid spacing and the outer boundary position are given in units of $M_\odot$

Name	L	L_{mv}	n	n_{mv}	h_6	h_0	R_0
R1	7	3	192	64	0.246	15.744	1511.4
R2	7	3	288	96	0.164	10.496	1511.4
R3	7	3	384	128	0.123	7.872	1511.4
R4	7	3	480	160	0.0984	6.2976	1511.4

characteristic fields (Jiang, 1996; Mignone et al., 2010; Suresh, 1997) to obtain high order convergence (Bernuzzi et al., 2016a).

Since we are interested in spin and precession effects, we can not enforce any additional symmetry and evolve the full 3D grid. This increases the computational costs by a factor of two compared to the simulations presented in the previous chapter where we employed bitant symmetry. In order to have compatible simulations even the spin-aligned and anti-aligned setups that are not expected to show any precession are evolved without imposing any symmetry. Details about the different grid configurations employed in this study are given in Table 5.2; the grid configurations are again labeled R1, R2, R3, R4, ordered by increasing resolution.

5.2 Orbital Motion & Gravitational Waves

In Fig. 5.1 we show a summary of all the configurations studied employing the R4 resolution. The figure shows the coordinate tracks of the individual NSs (positions of the local minimum of the lapse) in column-one, the precession cones of the individual spins (‘green’ & ‘blue’) and the orbital angular momentum (‘red’) in column-two, and the (2,2)- and (2,1)-modes of the GW signal in column-three. The individual rows refer to the different configurations given in the same order as the rows in Table 5.1.

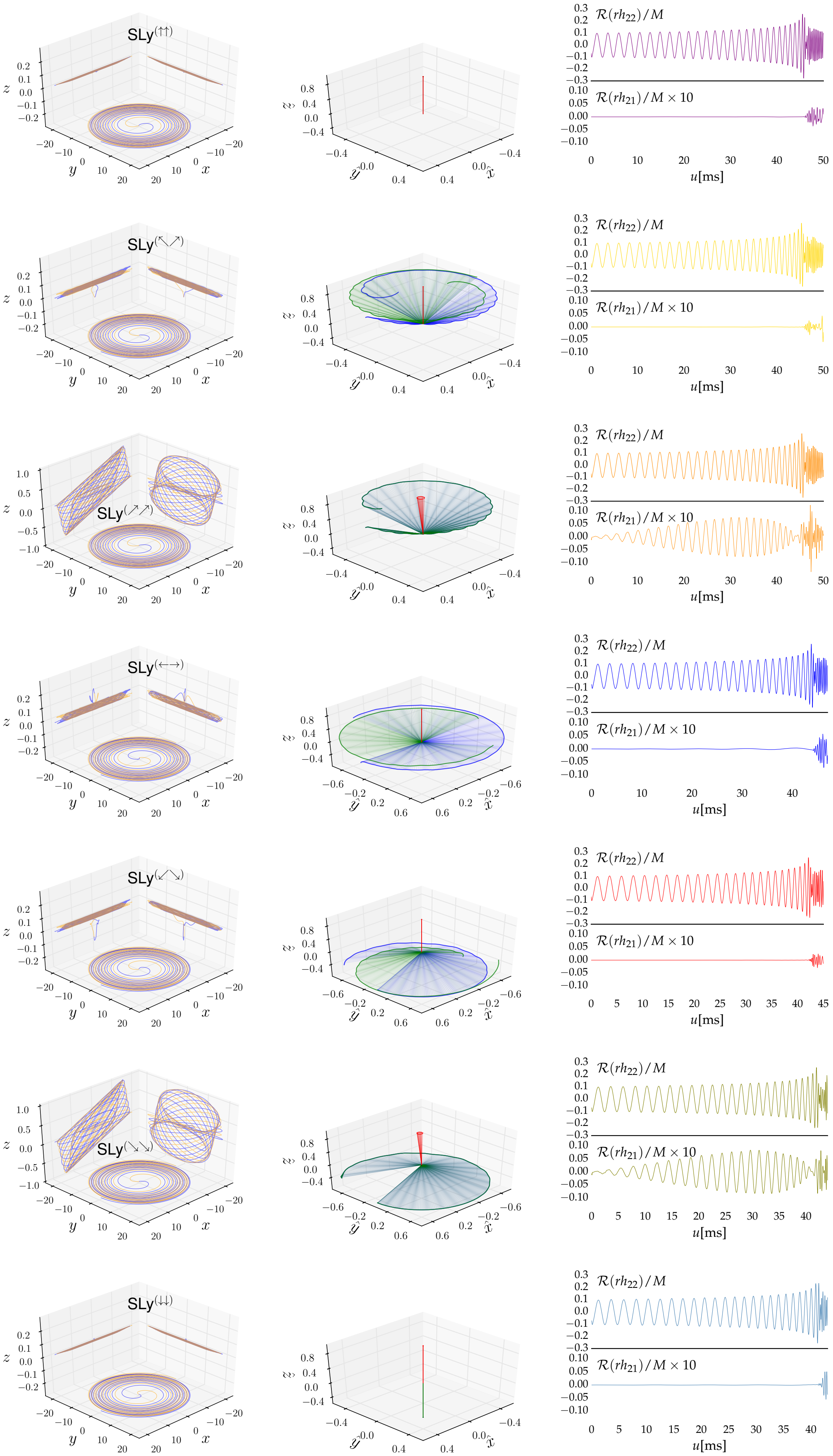

FIGURE 5.1: Orbital dynamics and GW emission for all configurations. *Column 1* shows the coordinate tracks of each NS in the binary. *Column 2* shows the corresponding precession cones. The spin evolution of the individual stars ('blue' and 'green'), and the orbital angular momentum of the system ('red') are shown here. *Column 3* shows the (2,2)- and (2,1)-modes of the GW strain *rh*.

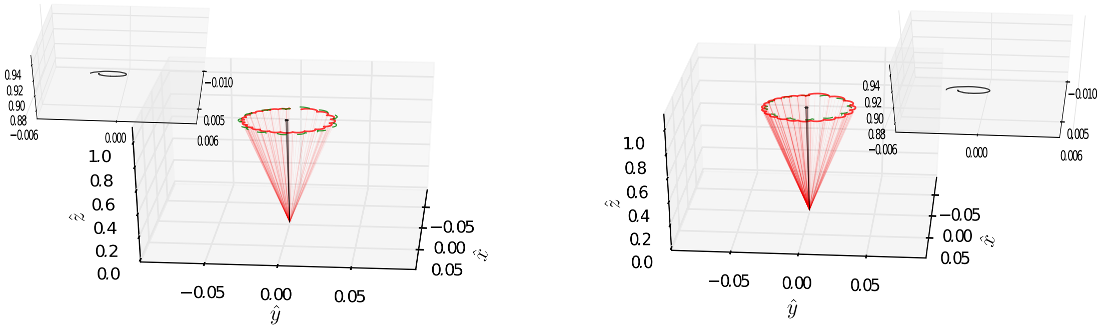

(A)

(B)

FIGURE 5.2: Precession cone for SLy$^{(\nearrow\nearrow)}$ **(A)** and SLy$^{(\searrow\searrow)}$ **(B)** configuration for the orbital angular momentum ('red'). Additionally, the precession cone of the total angular momentum ('black') is also presented, see inset above the main panels. As green dashed line we show the precession cones for $(\hat{L}_x, \hat{L}_y, \hat{L}_z)$ for SLy$^{(\searrow\searrow)}$ configuration in **(A)** and for SLy$^{(\nearrow\nearrow)}$ configuration in **(B)**. These overlays show that the opening angles for both the configurations are almost identical. It is possibly due to the rather small spins for the NSs considered in this study, that has only minor contribution to the orbital angular momentum of the system.

We find that the precession effect is largest for the SLy$^{(\nearrow\nearrow)}$ and the SLy$^{(\searrow\searrow)}$ configurations owing to the asymmetrically misaligned initial spins of the individual NSs. The orbital plane for these configurations undergo 'wobbling' motion i.e., the motion of the stars do not lie in a fixed plane but along 3D trajectories, dynamically changing in time. Moreover, the precession cones of the orbital angular momentum ($\hat{\mathbf{L}} = \hat{\mathbf{r}} \times \mathbf{d}\hat{\mathbf{r}}/\mathbf{dt}$, where $\mathbf{r}$ is the vector connecting star A and B, and hats denote the unit normalization of the vector) for these configurations, column-two of Fig. 5.1, show the largest opening angle. Apart from precession, the spin misaligned systems also show nutation of the spin axis i.e., small oscillations can be seen at about twice the orbital frequency and therefore on a much shorter timescale than the precession timescale. These nutation cycles are clearly visible for the individual spins for SLy$^{(\nwarrow\nearrow)}$ and SLy$^{(\nearrow\nearrow)}$ cases but are also present for the SLy$^{(\swarrow\searrow)}$ and SLy$^{(\searrow\searrow)}$ cases. Furthermore, the imprint of the orbital precession is also clearly seen in the modulation of the GW strain signal rh in the (2,1)-mode as is expected for such systems.

Other configurations for e.g SLy$^{(\leftarrow\rightarrow)}$ show different orbital dynamics owing to their symmetrically misaligned spins with respect to the orbital angular momentum. Precession effect is absent for such systems as is seen in the precession cones and the zero-signal in the (2,1)-modes. However, for such symmetrically misaligned configurations, as there is spin component that lies in the orbital plane and are opposite and of equal magnitude, any $z-$motion of the stars is in the same direction. This results in a 'bobbing motion of the orbital plane rather than the 'wobbling' motion that is expected for precession. In contrast to the spin (anti-) aligned configurations, this 'bobbing' motion is visible in the tracks of the stars as seen in the projections of the orbital motion on the $xz-$ and $yz-$planes in column-one of Fig. 5.1.

Interestingly, the motion of the orbital plane, 'wobbling' or 'bobbing' for the spin misaligned systems can be explained by considering the general relativistic frame-dragging effect or specifically the Lense-Thirring effect (Morsink et al., 1999). Due to this effect, a rotating mass in general relativity influences the motion of objects in its vicinity i.e., the rotating mass "drags along" spacetime in its vicinity, see Fig. 5.3. The frame-dragging due to the NS spins either produces a torque or a net force on the orbital plane giving rise to either 'wobbling' or 'bobbing' motions respectively.

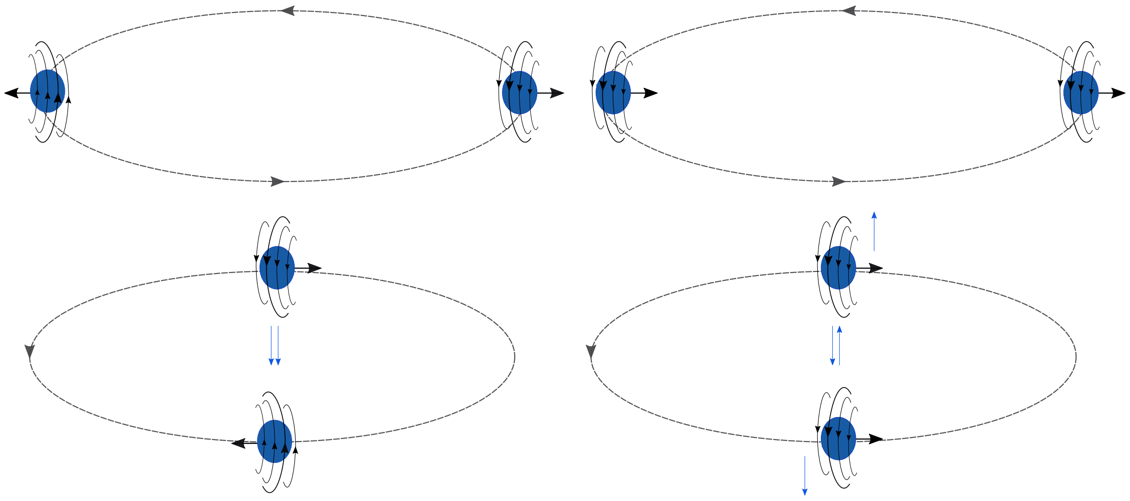

FIGURE 5.3: Schematic of the frame-dragging effect for a symmetrically misaligned system (column-one) and an asymmetrically misaligned system (column-two) on the orbital motion. Top rows show the initial configurations and the bottom rows show the state of the system at a later time in the evolution. Nutation of the spins here is assumed to be small for eaiser representation.

For the SLy$^{(\uparrow\uparrow)}$and SLy$^{(\downarrow\downarrow)}$configurations there is no precession as their initial spins are (anti-) aligned with the orbital angular momentum. Moreover, the orbital hang-up (speed-up) effect (Bernuzzi et al., 2014a; Campanelli et al., 2006) i.e., the fact that spin-aligned systems merge later and vice versa, is clearly visible in the

GW signal with respect to the peak time in the amplitude at the merger. This effect also holds for the spin misaligned systems that have an effective (anti-) aligned spin components with respect to the orbital angular momentum of the system.

5.3 Energetics

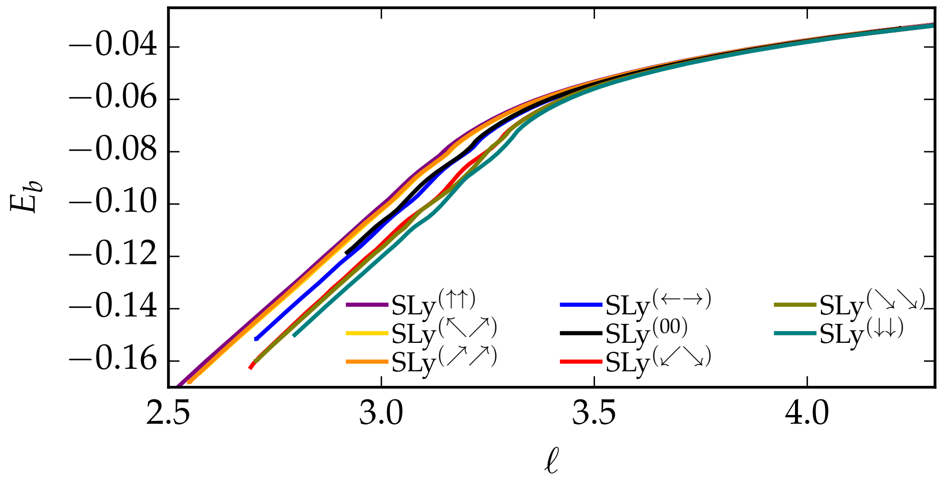

FIGURE 5.4: Binding energy E_b as a function of the specific orbital angular momentum ℓ for all configurations considered in this study for the R4 resolution. Additionally, we also include the curve for an irrotational case $\mathrm{SLy}^{(00)}$ taken from the CoRe Database (CoRe, 2018; Dietrich et al., 2018a) for comparison. The irrotational curve matches quite nicely to the $\mathrm{SLy}^{(\leftarrow\rightarrow)}$ case as would be expected for the symmetrically misaligned in-plane configuration.

We study the conservative dynamics for all the configurations presented by computing the binding energy,

$$E_b = \frac{M_{\mathrm{ADM}}(t_0) - E_{\mathrm{rad}} - M}{\nu\, M}, \tag{5.1}$$

and the specific orbital angular momentum,

$$\ell = \frac{|\tilde{\mathbf{J}}_{\mathrm{ADM}}(t_0) - \tilde{\mathbf{S}}_{\mathbf{A}}(t_0) - \tilde{\mathbf{S}}_{\mathbf{B}}(t_0) - \tilde{\mathbf{J}}_{\mathrm{rad}}|}{\nu\, M^2}. \tag{5.2}$$

Here $\nu := M^A M^B / M^2$ is the symmetric mass ratio, $E_{\mathrm{rad}}, \tilde{\mathbf{J}}_{\mathrm{rad}}$ are the emitted energy and angular momentum in the radiated GWs, and $M_{\mathrm{ADM}}, \tilde{\mathbf{J}}_{\mathrm{ADM}}$ denote the ADM-mass and angular momentum vector at the start of the simulation (i.e. at $t = t_0$), see e.g. (Bernuzzi et al., 2014a; Damour et al., 2012). $\tilde{\mathbf{S}}_{\mathbf{A}}(t_0)$ and $\tilde{\mathbf{S}}_{\mathbf{B}}(t_0)$ are estimated from the initial data, columns 5, 6 and 7 of Table 5.1, and $\tilde{\mathbf{S}}_{A,B} = M^{A,B}\chi^{A,B}\hat{\chi}^{A,B}$. In Appendix B, we present a few details about the post-processing step for the computation of the radiated energy and angular momentum in GWs extracted in numerical relativity simulations employing the `BAM` code.

In Fig. 5.4 we show the E-ℓ curve for all the configurations for R4 resolution. For comparison we also show the curve for an irrotational configuration SLy$^{(00)}$ ('black line') obtained from the CoRe database of BNS merger waveforms (CoRe, 2018; Dietrich et al., 2018a). For the early inspiral part of the orbital dynamics (large E & ℓ), though not apparent from the E-ℓ curves, there are non-vanishing differences among the simulated configurations and the irrotational case SLy$^{(00)}$ that we show with respect to their spin contribution to the binding energy E_b as seen in the top panel of Fig. 5.5. As a consequence of an effectively zero-spin contribution of the SLy$^{(\leftarrow\rightarrow)}$ configuration, its conservative dynamics is identical with SLy$^{(00)}$ configuration as can be seen in the top panel of Fig. 5.5. Moreover, during the late inspiral part when the stars have come close to each other due to the emission of energy and angular momentum in GWs, a clear difference is present as seen in Fig. 5.4 between the configurations. The irrotational configuration SLy$^{(00)}$ and the effectively zero-spin configuration SLy$^{(\leftarrow\rightarrow)}$ clearly demarcate the effectively aligned spin and the effectively anti-aligned spin configurations. In fact, aligned spin configurations are less bound while the anti-aligned spin configurations are more bound than the corresponding irrotational setup, which can be clearly seen from the curves. This follows from the fact that the spin-orbit interaction, which is the dominant spin-related effect, is repulsive for aligned spins and attractive for anti-aligned spins, e.g. (Damour, 2001).

The error estimate in Fig. 5.5 is shown as shaded-regions. It is obtained by taking into account the finite resolution of the simulations and is estimated from the difference between R3 and R4 resolutions. Furthermore, an additional uncertainty of 10^{-5} is added for accounting the errors coming in from the initial data solver (Dietrich et al., 2015a). The error bounds shown are obtained from error propagation assuming errors from different configurations are uncorrelated.

In order to disentangle the different contributions to the total binding energy due to the spin and orbital dynamics (Bernuzzi et al., 2014a; Dietrich et al., 2017c), we assume that it consists of a nonspinning contribution including tidal effects E_0, a spin-orbit E_{SO} contribution, and a spin-spin contribution E_{SS},

$$E_b = E_0 + E_{SO} + E_{SS} + \mathcal{O}(S^3). \tag{5.3}$$

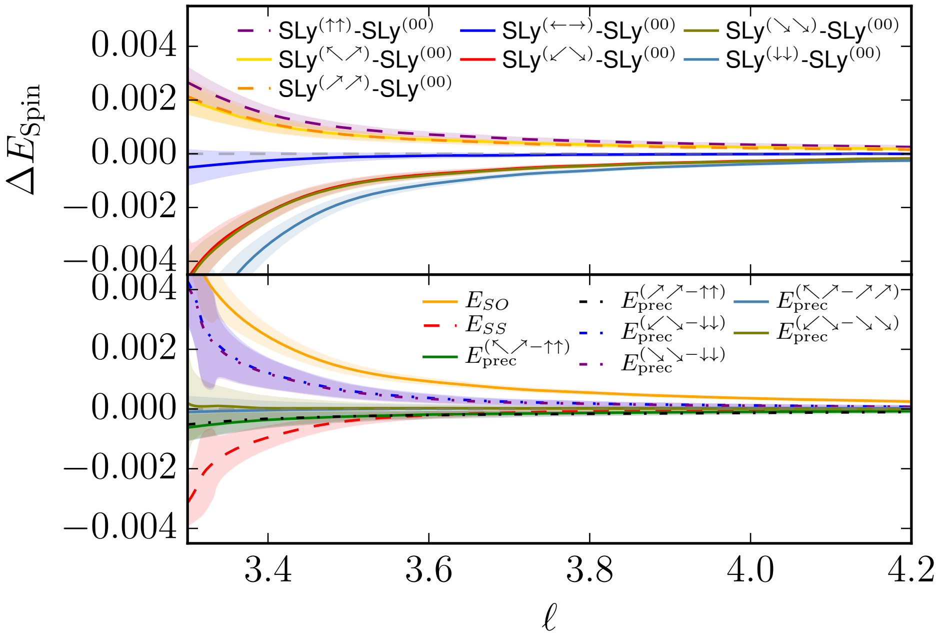

FIGURE 5.5: *Top panel* Estimate of the spin orientation effect on the conservative dynamics by taking the difference between all the configurations and the SLy$^{(00)}$configuration. The shaded region marks the difference in results obtained with a lower resolution and takes into account the uncertainty of the initial data. *Bottom panel* Spin and orbital contributions to the binding energy estimated following the discussion in the text.

The bottom panel in Fig. 5.5 shows these contributions to the binding energy. We compute the spin-orbit term E_{SO} as,

$$E_{SO} = \frac{E_b[\mathrm{SLy}^{(\uparrow\uparrow)}] - E_b[\mathrm{SLy}^{(\downarrow\downarrow)}]}{2}. \tag{5.4}$$

In general, the $SO-$interaction is at leading order $\propto \tilde{\mathbf{L}} \cdot \tilde{\mathbf{S}}_\mathbf{i}/\mathbf{r}^3$, see (Kidder et al., 1993). The magnitude E_{SO} is always positive and therefore the $SO-$interaction is either repulsive or attractive i.e., positive or negative, according to the sign of $\tilde{\mathbf{L}} \cdot \tilde{\mathbf{S}}_\mathbf{i}$. The spin-spin term includes the self-spin term (of the form $\tilde{\mathbf{S}}_\mathbf{i} \cdot \tilde{\mathbf{S}}_\mathbf{i}$) and an interaction term (of the form $\tilde{\mathbf{S}}_\mathbf{i} \cdot \tilde{\mathbf{S}}_\mathbf{j}$) between the two spins. The interaction term in particular is $\propto [3(\tilde{\mathbf{n}} \cdot \tilde{\mathbf{S}}_\mathbf{1})(\tilde{\mathbf{n}} \cdot \tilde{\mathbf{S}}_\mathbf{2}) - (\tilde{\mathbf{S}}_\mathbf{1} \cdot \tilde{\mathbf{S}}_\mathbf{2})]/\mathbf{r}^3$ (with $\vec{\mathbf{n}}$ denoting the unit vector pointing from one star to the other), see e.g. (Kidder et al., 1993). Note that the first term in the interaction term is zero for the (anti-) aligned configurations and the remaining term $\propto -(\tilde{\mathbf{S}}_1 \cdot \tilde{\mathbf{S}}_2)$ does not change sign if both spins flip. We estimate the complete spin-spin term i.e., including the interaction term and the self-spin term as,

$$E_{SS} = \frac{E_b[\mathrm{SLy}^{(\uparrow\uparrow)}] + E_b[\mathrm{SLy}^{(\downarrow\downarrow)}]}{2} - E_b[\mathrm{SLy}^{(00)}]. \tag{5.5}$$

We find that compared to the $SO-$interaction, the spin-spin interaction is almost zero during most part of the inspiral. This is almost for the entire simulation within the uncertainty of our data. SO is the dominant contribution to the binding energy up until the late inspiral after which tidal effects dominate the dynamics (Bernuzzi et al., 2014a). Intuitively, this is understandable since the dynamics reaches the hydrodynamical regime during the late inspiral and thereafter.

The effect of precession is understood by computing the following contribution,

$$E_{\mathrm{prec}}^{(\nwarrow\nearrow-\uparrow\uparrow)} = E_b[\mathrm{SLy}^{(\nwarrow\nearrow)}] - E_b[\mathrm{SLy}^{(\uparrow\uparrow)}], \tag{5.6}$$

and similar other combinations as shown in the legend of bottom panel in Fig. 5.5. We find that the configurations ($\mathrm{SLy}^{(\nwarrow\nearrow)}$ & $\mathrm{SLy}^{(\nearrow\nearrow)}$) and ($\mathrm{SLy}^{(\swarrow\searrow)}$ & $\mathrm{SLy}^{(\searrow\searrow)}$) are almost identical with respect to their binding energy contribution as seen in the bottom panel of that figure. This could be due to two reasons, (i) the spins are rather small to show any distinguishable effect and (ii) even the highest resolution employed in the simulations falls short in resolving the differences between those configurations. Overall, even though from the tracks, the precession cones and the GWs, cf. Fig. 5.1, the precession effects are apparent, the energetics does not shed any light on the differences, at least among the above mentioned pairs.

5.4 Ejecta

As in the study of the highly eccentric BNS mergers presented in the previous chapter, here again we compute the amount of ejected matter and its properties as shown for the R4 resolution simulation in Table 5.3.

Unbound matter in the case of precessing binaries like their quasi-circular counterparts, is mostly ejected in the very late inspiral from the tidal tail ejection mechanism or from shock heating during the collision of the cores of the NSs. Bound and unbound matter along with their velocity profile is shown for the $\mathrm{SLy}^{(\swarrow\searrow)}$ case in Fig. 5.6. Here, we see that the ejection does not happen until the surfaces of the NSs have touched (column-one). After that (column-two), unbound matter with

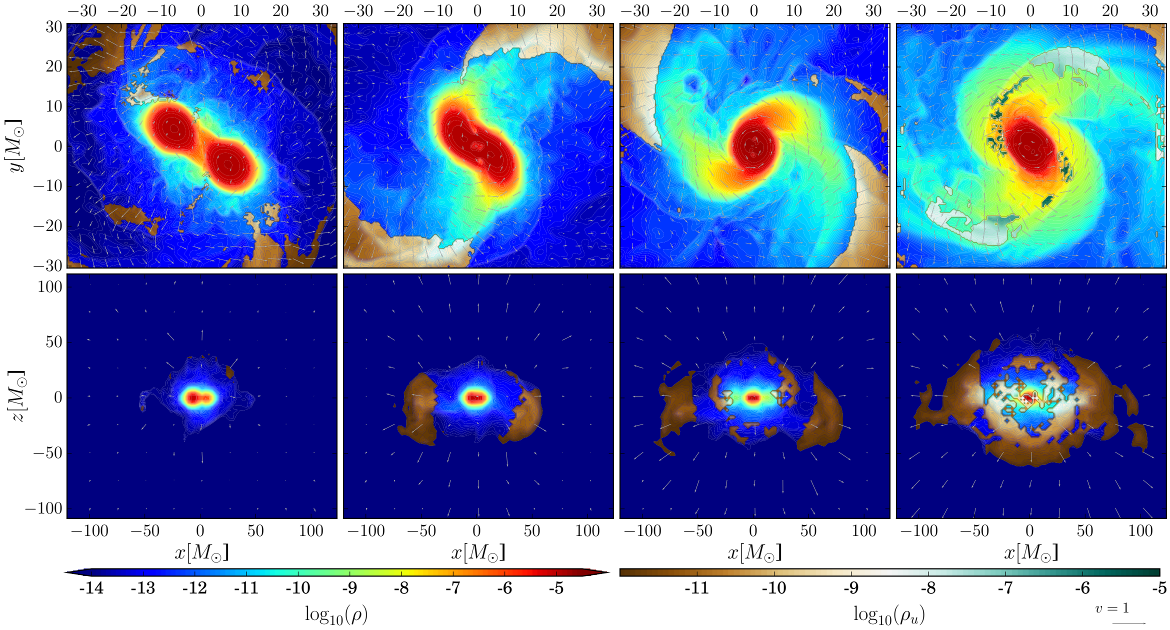

FIGURE 5.6: 2D-plots for the SLy$^{(\swarrow\searrow)}$ configuration showing the density and velocity field at different times close to the merger, with the unbound material [computed using the criterion in Eq. (A.1)] shown in the brown to green color scale, while the bound material is shown in a blue to red color scale. *Top row* plots show the $xy-$plane covering a distance of $\sim$ 88 km in each direction; *Bottom row* plots show the $xz-$plane, where each direction is covering a distance of $\sim$ 293 km. *columns one-three*: time after the surfaces touch till the cores of the NSs have collided and merged. *Fourth column*: Post-merger phase when a hypermassive NS has been formed.

density $\sim \mathcal{O}(10^{-9}) - \mathcal{O}(10^{-8})$ can be seen coming out from the tidal tail mostly in the orbital plane (note that this case does not show any precession, see Fig. 5.1). This ejecta quickly expands into the volume surrounding the system, dropping in density $\sim$ three orders of magnitude. Once the cores of the NSs have merged (column-three) there is ejecta also in the direction normal to the orbital plane owing to shock heating. During these last phases in the merger unbound matter of density $\sim \mathcal{O}(10^{-8}) - \mathcal{O}(10^{-6})$ is ejected nearly isotropically. In principle, unlike equal mass quasi-circular BNSs where the matter should be symmetrically ejected, similar setups for precessing BNSs can eject matter asymmetrically due to the 'wobbling' or the 'bobbing' motion of the system. This asymmetrical ejection of matter would then give a kick to the merged object due to linear momentum conservation. In addition to the matter ejecta, GW emission will also play a major role in deciding the magnitude and the direction of the kicks. Although not computed during the writing of this thesis, kick estimates will be presented in (Chaurasia et al., 2020).

From Table 5.3 we see that the unbound matter increases when the spin of the

TABLE 5.3: Ejecta properties. The columns refer to: the name of the configuration, the mass of the ejecta from the volume integral $M_{\mathrm{ej}}^{\mathcal{V}}$ and the kinetic energy of the ejecta T_{ej} in $M_{\odot}$ and in cgs units.

Name	$M_{\mathrm{ej}}^{\mathcal{V}}$ $[M_{\odot}]$	T_{ej} $[10^{-5} M_{\odot}]$	$[10^{49}$ erg$]$
$\mathrm{SLy}^{(\uparrow\uparrow)}$	0.0043	3.864	6.91
$\mathrm{SLy}^{(\nwarrow\nearrow)}$	0.0062	14.1	25.20
$\mathrm{SLy}^{(\nearrow\nearrow)}$	0.0054	3.569	6.38
$\mathrm{SLy}^{(\leftarrow\rightarrow)}$	0.0162	31.6	56.49
$\mathrm{SLy}^{(\swarrow\searrow)}$	0.0188	53.1	94.92
$\mathrm{SLy}^{(\searrow\searrow)}$	0.0189	33.1	59.17
$\mathrm{SLy}^{(\downarrow\downarrow)}$	0.0192	52.0	92.95

NSs is effectively anti-aligned to the orbital angular momentum. This indicates that the ejecta is dominated via shock mechanism during the merger of the cores of the two stars (Kastaun et al., 2017). Overall, $\sim \mathcal{O}(10^{-3}) - \mathcal{O}(10^{-2}) M_{\odot}$ of unbound matter is ejected for the configurations studied. The kinetic energy follows a similar pattern, where overall in-plane or effectively anti-aligned configurations have ejecta with largest kinetic energy. This will result in larger fluencies of possible radio flares. Furthermore, no quantitative effect of precession is found and can be resolved with respect to the ejecta amount within our simulations. However, the morphology of the ejecta could show differences as discussed earlier.

Chapter 6

Discontinuous Galerkin Method for GRHD

In this chapter we present the results from our implementation of the discontinuous Galerkin method for solving the general relativistic hydrodynamics equations derived in Sec. 2.2. Solutions obtained using spectral methods are known to show exponential convergence to the true solution across the entire domain for smooth functions and in the relevant norm, see Sec. 3.6 for a brief discussion and (Grandclément et al., 2009; Kopriva, 2009) for more details. While the final goal of using high-order spectral methods in solving PDEs is to obtain very accurate solutions using efficient computational methods, it nevertheless behooves us in understanding how this applies to systems that have discontinuities and can form shocks, such as the astrophysical scenarios arising in numerical relativity simulations.

We present the test results of our methods, as presented in Secs. 3.3 and 3.4 with a fairly good choice of testbeds representative of the complexity involved in finding solutions to the GRHD equations for astrophysically relevant scenarios. Apart from the tests themselves, the methods treating discontinuities are also chosen as a representative from the pool of methods available for handling discontinuities.

In Sec. 6.1 we start with a 1D benchmark problem, namely, an isentropic smooth wave test in flat spacetime. It is an important benchmark as exact solutions are available for this setup. Continuing with the equations of special relativistic hydrodynamics, we test a robust shock detecting method and use it to test shock capturing ability of our implementation using a minmod slope limiter and a WENO-3 limiter in shock tube simulations in 1D. The multidimensional schemes are in general obtained by successive application of 1D schemes and therefore it is justified to have robust tests in lower dimensions. In Sec. 6.2 we perform an isolated neutron star evolution in three-dimensions in the cowling approximation and present the results obtained.

6.1 Flat Spacetime Tests

We consider the complete set of the GRHD conservation law Eqs. (2.51–2.52) without source terms i.e., we set $\alpha = 1$, $\beta_i = 0$ and $\gamma_{ij} = \delta_{ij}$ for simulating the special relativistic test case i.e., flat spacetime.

Isentropic Smooth Wave

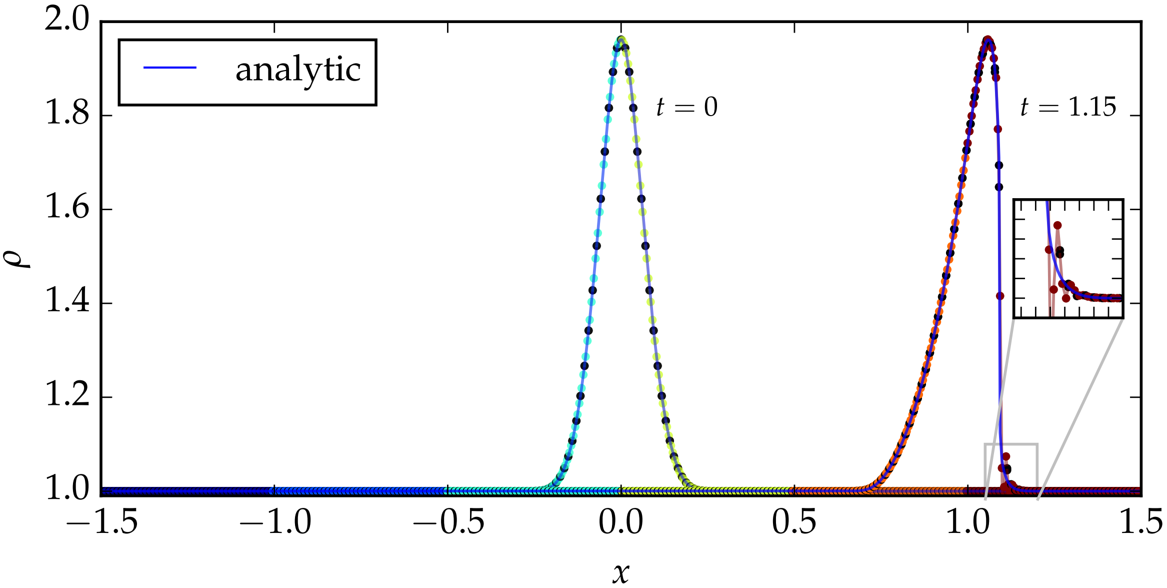

FIGURE 6.1: Relativistic simple wave in 1D. Solution is computed on $K = 256$ elements with each element using a $\mathcal{P}_3$ polynomial constructed using $N + 1 = 4$ Legendre-Gauss-Lobatto collocation nodes. The system is known to form a shock at $t \sim 0.63$, see (Liang, 1977, Eq. (III.2)). The inset plot shows the Gibbs phenomena that arises due to discontinuities as discussed in Sec. 3.6. The color code refers to the distribution of the grids on different processors (here #processors = 6). The 'black' points refer to the boundary nodes of each element. Load balancing is employed to evenly distribute the elements across the processors. The evolution uses a CFL factor of 0.125.

Relativistic simple waves are nonlinear elementary waves that are analogous to linear sound waves (Anile, 1990; Liang, 1977). One can find the exact solutions implicitly by the method of characteristics. During the evolution of such waves a shock is expected to form in finite time due to nonlinearities. The right traveling simple wave initial data are set up by (a) setting a reference state ($\rho = 1$, $v = 0$), (b)

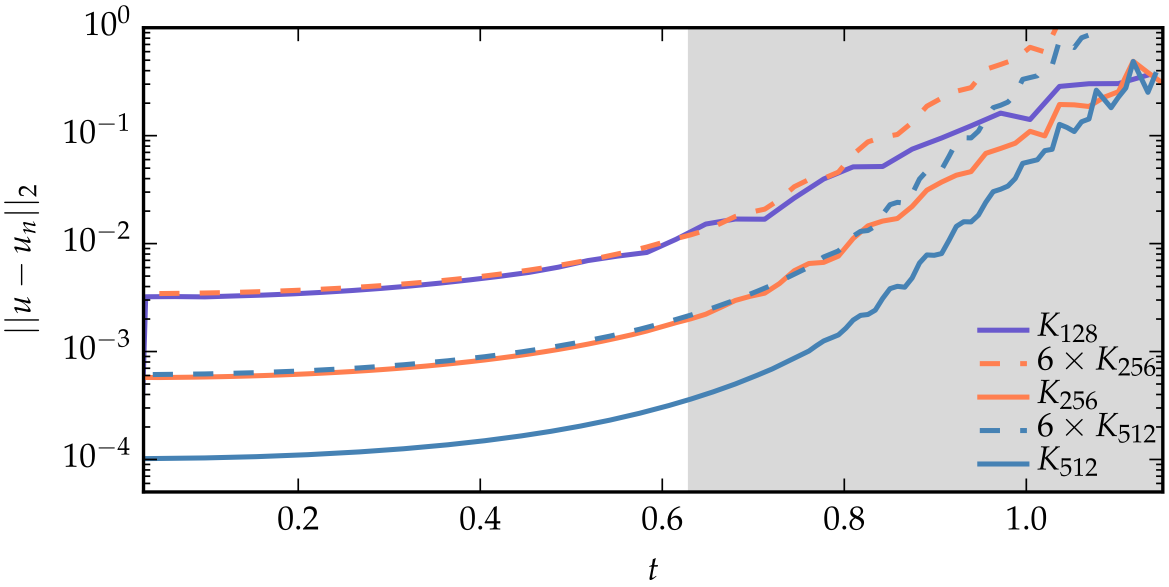

FIGURE 6.2: The L_2-norm for the isentropic wave test. Until the shock formation at $t \sim 0.63$, the pure DG method upholds close to the theoretical order of convergence, namely, N^{th} order convergence for $\mathcal{P}_N$, where $N = 3$. The grey shaded region marks the time after the shock formation. Seen in Fig. 6.1, as the pulse evolves towards the right boundary it forms a shock on the right-front. The pure DG method is able to handle weak shocks but at later times when the shock becomes stronger (i.e., the slope of the solution steepens) Gibbs phenomena takes over in the shock region, see the inset plot in Fig. 6.1 and thereby the error in the solution grows.

assigning a velocity perturbation, and (c) calculating the sound speed according to the value of the Riemann invariant (Liang, 1977, Eq. (II.15)). The other quantities follow from the EOS. The velocity profile in this test is set as,

$$v = a\,\Theta\left(|x| - X\right)\,\sin^6\left[\frac{\pi}{2}\left(\frac{x}{X} - 1\right)\right], \tag{6.1}$$

where $\Theta(x)$ is the Heaviside function, $a = 0.5$ and $X = 0.3$. Assuming a polytropic EOS, Eq. (2.54a), with $\Gamma = 5/3$ and $\kappa = 100$, the value of the sound speed in the reference state is $c_s \simeq 0.815$; the initial density profile is shown in Fig. 6.1.

Numerical solutions are computed on the domain $[-1.5, 1.5]$, with the RK4 integrator and a CFL factor of 0.125. During the evolution the initial profile progressively steepens on the right-front and finally forms a shock at $t \simeq 0.63$. The time of shock formation is estimated using (Liang, 1977, Eq. (III.2)) with the velocity profile given by Eq. (6.1). Figure 6.1 shows the initial state at $t = 0$ and the numerical solution at $t = 1.15$ for a grid configuration of $K = 256$ elements with each element consisting of $N + 1 = 4$ Legendre-Gauss-Lobatto nodes. An integer number of elements are evenly distributed across the available processors allowing for a proper load balancing.

Although no shock capturing strategy is applied, we find that the DG method is able to handle the shock while it is still weak (i.e., steepening of the slope is gradual) close to the shock formation. As shown in Fig. 6.2, we obtain close to the expected N^{th} polynomial-order-convergence[1] with the L_2-norm until the caustic formation. After caustic formation the error in the solution grows mainly due to the oscillations in the solution near the shock front. The maximum difference between the analytic solution and the numerical solution does not converge to zero even when N is increased. The spurious oscillations near the discontinuity as seen in the inset box in Fig. 6.2 are the famous Gibbs phenomena as discussed in Sec. 3.6. Spectral methods typically perform poorly for non-smooth problems, such as the modeling of fluid shocks and discontinuities.

Shock tubes

In the previous test we concluded that the DG method is spectrally convergent only for smooth problems. Once the solution develops discontinuities, the use of spectral method becomes less appealing. Therefore, one way forward with using such methods is to minimize or completely remove the spurious oscillations using some filtering or limiting procedure. However, for most cases with discontinuities filtering alone is not enough and has to be supplemented with a robust limiting technique. To identify the regions of the computational domain containing discontinuities a robust troubled cell indicator is a preliminary step.

In this work we tested a new troubled cell indicator based on a measure of the locally generated entropy inspired by Zingan et al. (2013) and Guercilena et al. (2017). Canonical indicators are usually based on comparing neighbor cell-averages (or element-averages) to detect troubled regions (Bugner et al., 2016; Kidder et al., 2017) and often come with a caveat such that extrema regions of the solution are also marked as troubled. Moreover, such cell-average based indicators require additional communications of the averages which adds to the scalability overhead of the code. In order to overcome this issue, the entropy measure is used to flag generically problematic points of the computational domain. Since entropy is produced only in the presence of shocks, this results in a very robust method that is able to mark the truly troubled regions and since it is a local measure, no communication is required for evaluating it.

---

[1] For a hp-element method, the order of accuracy is given at least to be $\mathcal{O}(h^p)$, where h is the mesh size and p is the order of the interpolating polynomial.

Entropy indicator

Following (Guercilena et al., 2017; Guermond et al., 2011; Zingan et al., 2013), our motivation is to construct a troubled cell indicator such that it is related with some property of the fluid flow. However, note that in (Guercilena et al., 2017) the basic idea has been to add an entropy-residual weighted low-order numerical flux to a high-order numerical flux in a finite-differencing scheme, and in (Guermond et al., 2011; Zingan et al., 2013) the entropy-residual is used to add a viscous-term in a DG scheme. As in Guercilena et al., the specific entropy s of the fluid is chosen. For the simple case of a perfect fluid with an ideal-gas EOS, see Eq. (2.54b), the specific entropy can be written, excluding constant factors (Rezzolla et al., 2013), as

$$s = \ln\left(\frac{\epsilon}{\rho^{\Gamma-1}}\right). \tag{6.2}$$

The precise form of s will be different for different EOSs. Moreover, since the specific entropy is a physical entropy measure, it must satisfy the second law of thermodynamics, such that the entropy residual, or entropy-production rate, $\mathcal{R}$ can be introduced for the general relativistic[2] scenario as

$$\mathcal{R} := \nabla_\mu\left(\rho s u^\mu\right) \geq 0, \tag{6.3a}$$

$$\mathcal{R} = \frac{\rho W}{\alpha}\left[\partial_t s + (\alpha v^i - \beta^i)\partial_i s\right]. \tag{6.3b}$$

The expanded form of $\mathcal{R}$ in (6.3b) can be derived from (6.3a) by using the rest-mass conservation equation (2.33) and the the 3+1 split of the fluid four-velocity. In the numerics, the spatial derivative of s is computed from the DG differentiation matrix multiplication. The time derivative in (6.3b), however, is approximated by finite differencing. In particular, at every iteration the current value of the specific entropy and the values at the two previous timesteps are used to compute a second-order approximation of $\partial_t s$ via a backward differentiation stencil i.e.,

---

[2] Note that for flat spacetime tests we set $\alpha = 1$, $\beta_i = 0$ which will give the special relativistic equivalent of the entropy residual.

$$(\partial_t s)^n = \frac{1}{2\Delta t}(3s^n - 4s^{n-1} + s^{n-2}) + \mathcal{O}[\Delta t^2]. \tag{6.4}$$

As noted in the references, the entropy residual is such that it should not decrease in time and is restricted spatially to confined regions in the proximity of shocks. This can be recognized as a delta function peaked at the location $\bar{x}_s$ of shocks, i.e., $\mathcal{R} \propto \delta(\bar{x} - \bar{x}_s)$. The shocks are localized since, and as noted in (Guercilena et al., 2017), the Euler equations in general truly apply to perfect fluids, and although they are capable of capturing non-ideal features i.e., shocks, the description of the latter is only approximate. Moreover, while the flow is smooth and the perfect-fluid approximation holds, all phenomena are reversible and there can be no production of entropy. However, in those scenarios where the perfect-fluid approximation breaks down and non-ideal effects become prominent, namely, at the location of shocks, the entropy production is nonzero and the entropy jumps locally to higher values. Further, since shocks are regions of dimension $m-1$ (spatially), in manifolds with m (spatial) dimensions, the entropy residual $\mathcal{R}$ can only be a Dirac-delta peaked at shock locations for it to provide a finite contribution.

Taking motivation from Zingan et al. (2013, Eq. (6.7)), to construct a shock indicator θ based on the entropy residual and to concoct it such that it is a function of the spatial discretization, we define it as,

$$\theta := ch^2|\mathcal{R}|. \tag{6.5}$$

Note that since $\mathcal{R}$ has to approximate a delta function, it is expected to show oscillations with potential negative values in the numerics. Therefore, the absolute value is used for $\mathcal{R}$ in (6.5). In expression (6.5), h is the minimum spacing on each element and c is a positive tunable constant which we always set to unity.

Further, since our purpose for computing the entropy residual is to detect regions containing shocks, it is useful to set θ_E, the residual over the whole element, as the maximum of θ computed at each node of the element,

$$\theta_E = \max(\theta_0, \theta_1 \ldots \theta_N). \tag{6.6}$$

This definition ensures that if entropy is generated at a single node of the element then the whole element is marked as troubled.

As noted in the references, the advantage of using entropy to detect shocks is its ability in automatically differentiating shocks from contact discontinuities. This follows from the fact that at contact discontinuities there is no entropy production and therefore the residual there is zero, as in the smooth regions (Zingan et al., 2013). However, in the following tests it will become clear that this is not true in numerical applications where there could be numerical entropy generation.

Riemann Problem in 2D

We consider a two-dimensional special relativistic Riemann problem on the domain $(x, y) \in [-1, 1] \times [-1, 1]$, see (Zhao et al., 2013, Example (4.8)). The initial data are set as follows:

$$\left\{\rho, v_x, v_y, p\right\}(x, y, t = 0) = \begin{cases} (0.03515, 0, 0, 0.163), & x \geq 0, y \geq 0 \\ (0.1, 0.7, 0, 1), & x < 0, y \geq 0 \\ (0.5, 0, 0, 1), & x < 0, y < 0 \\ (0.1, 0, 0.7, 1), & x \geq 0, y < 0 \end{cases} \tag{6.7}$$

Figure 6.3 shows the density (top row) and the entropy residual (bottom row) at four evolution stages for the initial data for the Riemann problem. We find that the four initial discontinuities interact each other and form a "mushroom cloud" around the point $(0, 0)$ as time increases, cf. (Zhao et al., 2013, Fig. (4.16)). The left and bottom discontinuities are two contact discontinuities and the top and right are two shock waves. The DG scheme using 100×100 elements with each element having $(N + 1) = 6$ LGL nodes in each direction, in addition to filtering as described in (Hilditch et al., 2016), captures the contact discontinuities, shock waves, and other complex structures well albeit with unwanted oscillations that grows near the contact discontinuities.

The entropy residual marks the troubled regions remarkably well. Since no limiting procedure is applied in this test and filtering alone is not enough to remove all the oscillations arising from Gibbs phenomena, the solution shows oscillations in the proximity of the contact discontinuities, see also the discussion of Sec. 3.6. Furthermore, as opposed to the fact that at contact discontinuities no entropy is

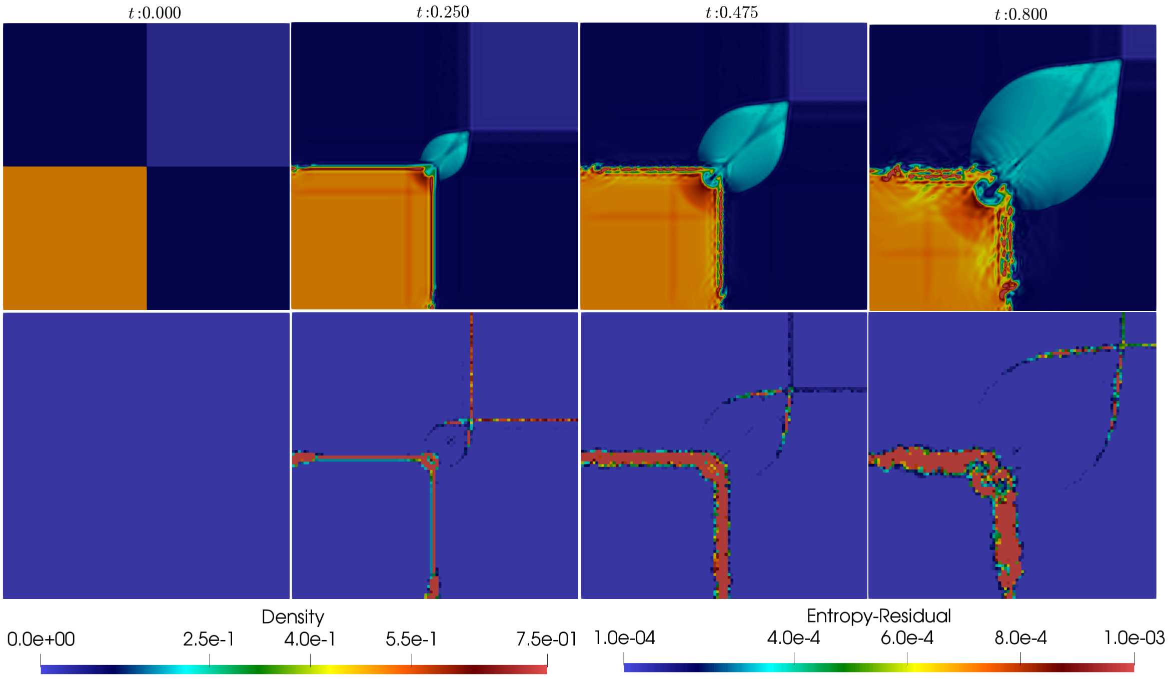

FIGURE 6.3: Shock tube test in 2D using an ideal-gas EOS with $\Gamma = 5/3$, see Eq.(2.54b). Time evolution is shown from left to right for four different times. The domain covers $(x, y) \in [-1, 1] \times [-1, 1]$ and uses 100×100 elements, with each element having $(N+1) = 6$ LGL nodes in each direction. RKDG scheme is used everywhere without additional shock capturing methods but with filtering as described in (Hilditch et al., 2016). The top row shows the density ρ and the bottom row shows the troubled cells marked using the entropy residual. We see that the troubled regions are marked remarkably well. Moreover, the contact discontinuity is also marked as troubled owing to Gibbs phenomena and possibly from the implicit transformation from the conserved variables to the primitive variables using the root finding procedure.

generated, Fig. 6.3 shows otherwise. The contact discontinuity is also marked as troubled owing to Gibbs phenomena i.e., numerical entropy generation due to the limitations of the DG (or spectral) method in approximating discontinuities and possibly from the implicit transformation from the conserved variables to the primitive variables using the root finding procedure as discussed in Sec. 3.5.

Riemann Problem in 1D

Next we look at the Riemann problem in 1D on the domain $x \in [-0.5, 0.5]$, see (Zhao et al., 2013, Example (4.2)). We perform a preliminary test for detecting troubled regions using our entropy based indicator and apply limiting procedure on the conserved variables. Ideal-gas EOS with $\Gamma = 5/3$ is used and the initial data are set as follows:

$$\{\rho, v_x, p\}\,(x, t=0) = \begin{cases} (1, 0, 1000), & x \leq 0 \\ (1, 0, 0.01), & x > 0 \end{cases} \tag{6.8}$$

The exact solution comprises of a right-going shock wave, followed by a contact discontinuity and a left-going rarefaction wave (the curved region), cf. Fig. 6.4. Since the pressure has an initial jump of five orders of magnitude, the flow profile is sharp and difficult with a very curved profile for the rarefaction wave due to the appearance of the ultra-relativistic regime. The contact discontinuity and shock wave move at essentially the same speed, giving rise to a very narrow constant rest-mass density state between the two such that resolving those waves is very challenging.

The exact solution ("solid blue line") and the numerical solution at $t = 0.4$ obtained by the RKDG method with a minmod slope limiter, as described in (Kidder et al., 2017), and a high resolution shock capturing WENO-3 limiter (3^{rd} order accurate), as described in (Bugner et al., 2016), are shown in Fig. 6.4.

6.2 Isolated Star in Cowling Approximation

For the tests in this section we evolve the GRHD variables on a fixed curved spacetime background. This is known as Cowling approximation (Cowling, 1941). We consider a single static neutron star in three-dimensions albeit with octant symmetry i.e., due to the spherical symmetry of the system we evolve only the octant of the numerical domain to reduce computational costs. The initial data for the neutron star is setup by obtaining the *Tolman-Oppenheimer-Volkoff* (TOV) solution (Oppenheimer et al., 1939; Tolman, 1939), which is the simplest solution for Einstein-Euler equations i.e., Einstein field equations in the presence of matter fields (Carroll, 2003; Wald, 1984).

The TOV solution is determined by the central density ρ_c of the star under the prescription of an EOS. For each EOS there exists a unique ρ_c that gives a stable equilibrium solution. Above this threshold, the solution is in unstable equilibrium and can collapse to a BH or settle to a stable configuration when perturbed.

We construct and evolve a TOV model with central rest-mass density $1.28 \times 10^{-3} M_\odot$ with a polytropic EOS with $\Gamma = 2, \kappa = 100$, yielding a (baryon) rest mass of $1.5 M_\odot$ and a radius of $\simeq 9.59 M_\odot$ (or $\simeq 8.13 M_\odot$ in isotropic coordinates that is used in constructing the initial data such that the spatial part of the metric is explicitly conformally flat). A polytropic EOS is used for the initial data construction whereas

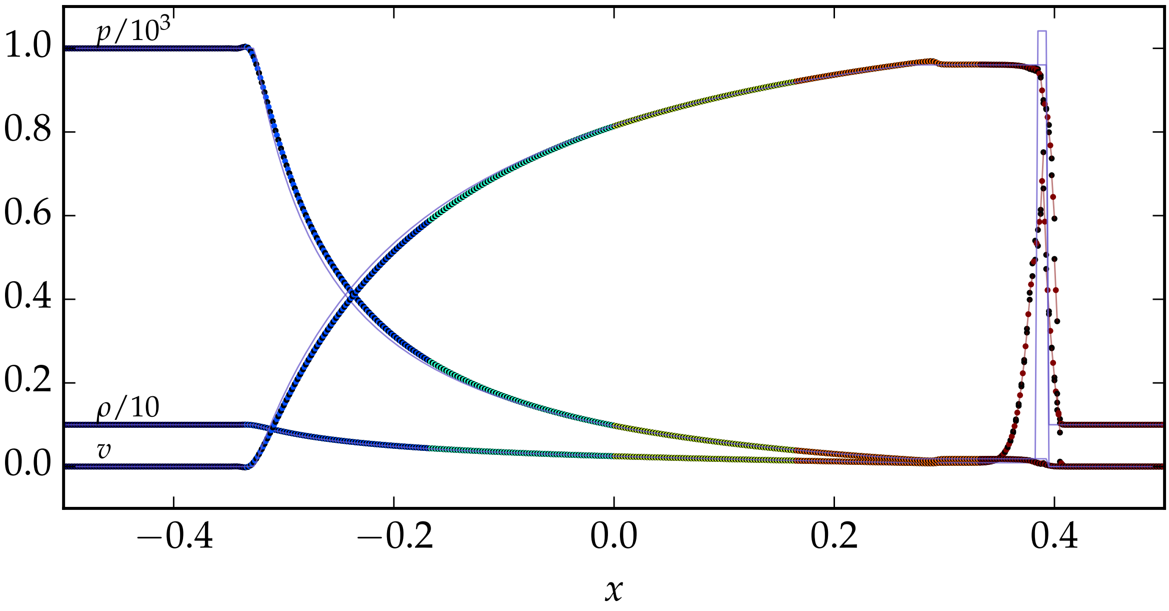

(A) minmod limiter, K = 400 with $\mathcal{P}_2$ polynomial.

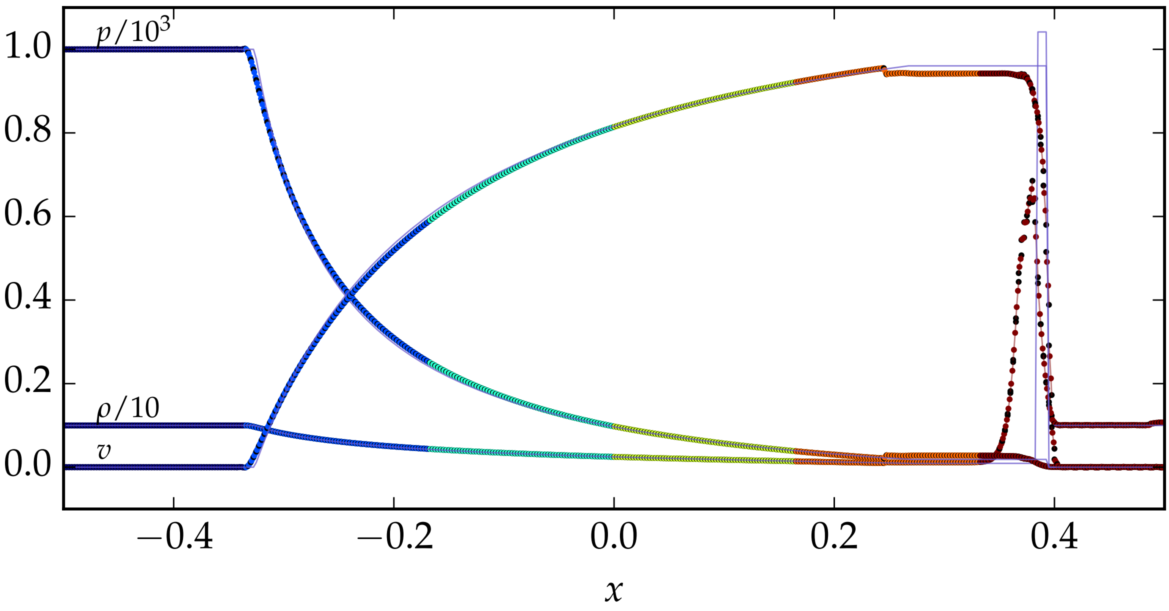

(B) weno-3 limiter, K = 400 with $\mathcal{P}_3$ polynomial.

FIGURE 6.4: Riemann problem in 1D (Blastwave), cf. (Zhao et al., 2013, Figs. (4.4-4.6)). Shown here is the numerical and the analytical profile of the rest-mass density, velocity and the pressure at t = 0.4. The domain covers $x \in [-0.5, 0.5]$ and uses 400 elements. RKDG scheme is used everywhere with additional shock capturing methods. The limiters are applied in the troubled regions marked by computing the entropy residual as discussed in the text.

for the evolution an ideal-gas EOS is considered. A CFL factor of 0.25 is used for the evolutions and the atmosphere value ρ_{atm} is set to be 1.28×10^{-15}.

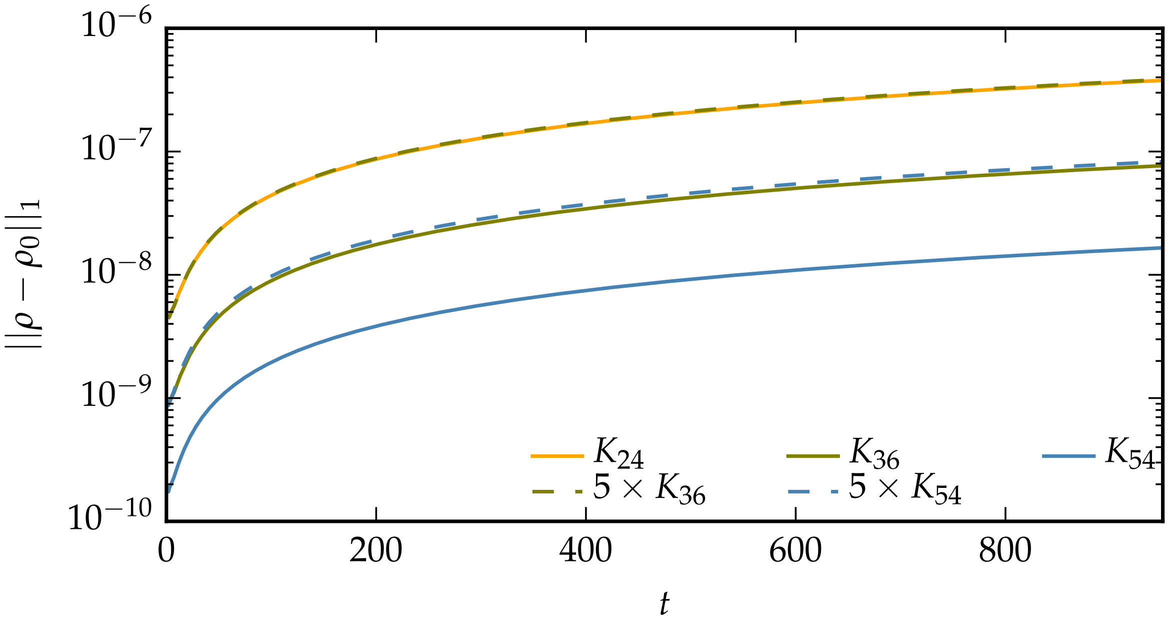

FIGURE 6.5: Shown here is the L_1-norm of the error in density of a TOV star in three-dimensions where the surface of the star is excluded in the evolution. Cowling approximation is assumed and DG method with each element having a polynomial $\mathcal{P}_5$ is used.

Taking motivation from the previous tests where the presence of a discontinuity introduced unwanted oscillations in the numerical solution, we first evolve the TOV star excluding its surface from the numerical domain as the matter-vacuum interface is identified as a contact discontinuity. Since the interior of the star is expected to be smooth in the current model, the DG method shows the expected order of convergence, see Fig. 6.5. We used the difference between numerical and analytical density solution as an error estimate. From this we can confirm that the DG method gives the expected order of convergence for a general relativistic setup with non-trivial background spacetime though with smooth solutions.

The evolution of the entire star , see Fig. 6.6, i.e., including the star surface within the computational domain, however, does not show the expected convergence.

In Fig. 6.6 we show the density in the top row plots and the entropy residual in the bottom row plots at $t = 0$ (left column) and $t = 1000M_\odot$ (right column). The entropy indicator marks the surface as troubled owing to the Gibbs oscillations due to the inability of the DG method to capture sharp profiles, see Sec. 3.6 and possibly the root finding procedure to transform the conservative variables to the primitives at the surface might be introducing additional errors that grow in time.

To cure these pathological oscillations and capture sharp profiles of the discontinuities, high resolution shock capturing methods have been used effectively

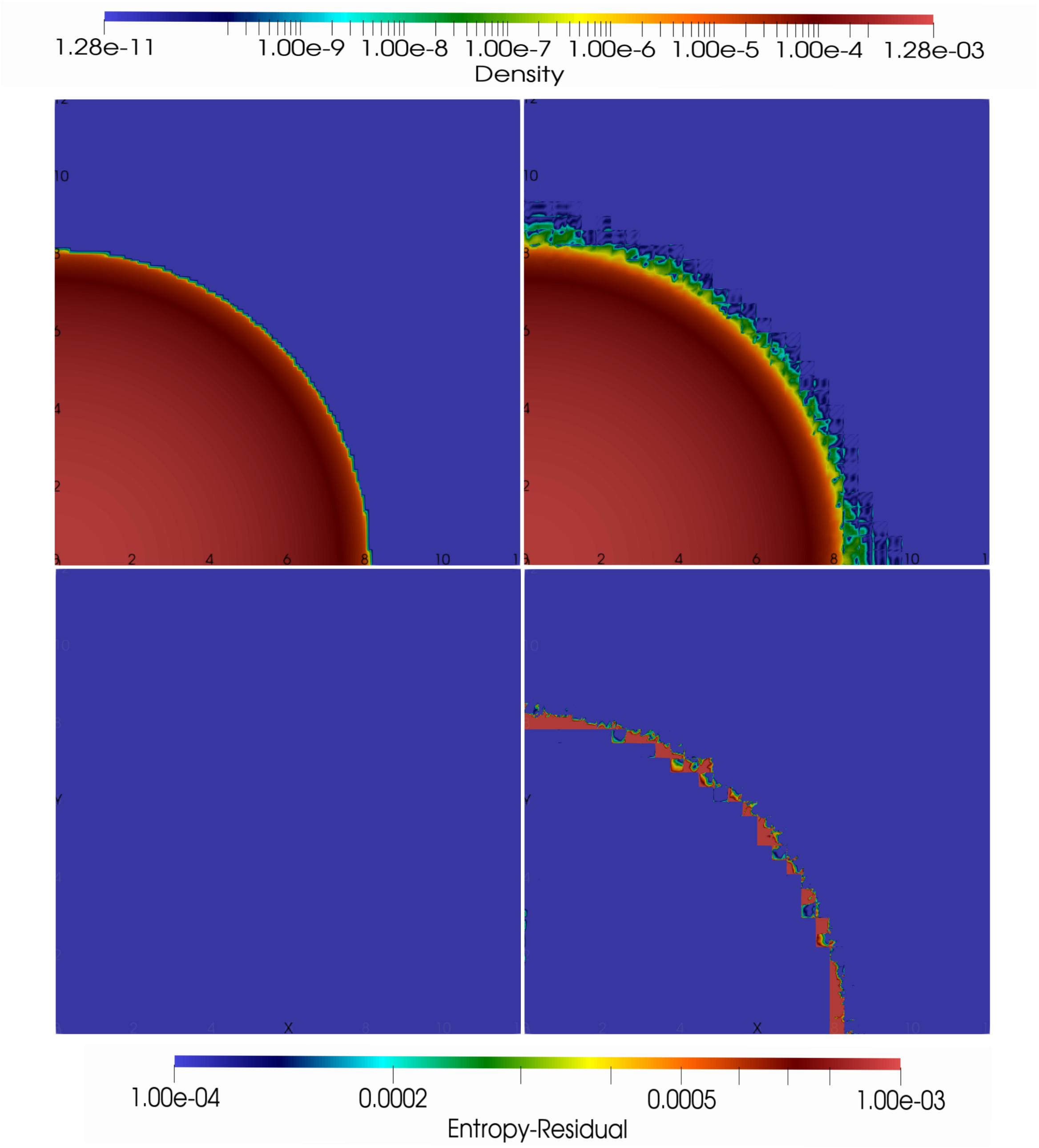

FIGURE 6.6: Shown here is the xy-plane of a TOV star evolution in cowling approximation in three-dimension using the DG method with a $\mathcal{P}_5$ polynomial. Similar views are obtained for the yz- and the xz-planes. *Left column* shows the density (top row) and the entropy residual (bottom row) at $t = 0$. *Right column* shows the same quantities but at $t = 1000M_\odot$. Note that no limiting procedure is applied here, although we use filtering as referenced earlier. Surface of the star is a discontinuity which the pure DG method fails to sharply capture.

though with varying degree of success in astrophysical simulations and most naturally in the context of finite difference or finite volume methods (Radice et al., 2014; Thierfelder et al., 2011). However such schemes potentially suffer from major shortcomings in the context of spectral element methods; (i) increasing the formal order of accuracy downgrades the essential feature of spectral element methods i.e., the method starts to resemble finite difference or finite volume stencils leading to larger requirements of neighbor data communications depending on the order of the HRSC method employed; (ii) Owing essentially to this non-locality, these schemes can lead to load imbalance in parallel implementations as a result of their complexity, downgrading the scalability of such spectral codes; all at the cost of obtaining at best a linear-order convergence in the presence of discontinuities.

In future, a detailed exploration going beyond the conventional methods of limiting discontinuous solutions, such as using filtering (Hilditch et al., 2016) and HRSC methods (Bugner et al., 2016; Kidder et al., 2017), is required in the context of spectral methods. Some techniques to try, but not limited to, are entropy-residual weighted artificial viscosity (Zingan et al., 2013) method, reprojection (Gottlieb et al., 1992; Gottlieb et al., 2011), and mollification (Gottlieb et al., 1985; Piotrowska et al., 2019; Tadmor, 2007).

Chapter 7

Conclusions

In this thesis we investigated the violent merger scenario arising in the coalescence of BNS mergers on highly eccentric orbits, and on precessing orbits. We performed full (3+1)D NR simulations employing the `BAM` code using consistent initial data i.e., data which are in agreement with the Einstein equations and with the equations of GRHD in equilibrium. This helped us in shedding light on the astrophysical processes that would be taking place during these events. Further, we investigated the DG method, a new paradigm in numerically solving the GRHD equations arising in neutron star spacetimes using the `bamps` spectral code.

For BNSs on highly eccentric orbits for either irrotational or aligned-spin stars, the initial eccentricity was systematically varied to isolate the effect of (large) eccentricity with a fixed initial separation of the NSs. Depending on the initial eccentricity, it was found that the number of orbits significantly varied (starting from a fixed coordinate separation of the stars), ranging from half an orbit for the most eccentric system to as many as $\sim$ 18 orbits for the least eccentric configuration employing the SLy EOS and aligned spins. Furthermore, no clear imprint of eccentricity on the merger remnant properties in general was found. Thus, quantitative statements about the remnant properties must await future work when much higher resolution simulations will be available.

The estimates for unbound matter showed that $\sim \mathcal{O}(10^{-2})\ M_\odot$ of matter is expected to be ejected at the merger. This was found to be slightly or even an order-of-magnitude more than in the quasi-circular cases for the soft and the stiff EOSs considered respectively. The simulations showed that tidal tail ejecta are more prominent compared to shock-heated ejecta or ejecta due to the redistribution of angular momentum in the postmerger remnant. Moreover, unbound matter $\sim \mathcal{O}(10^{-3}) - \mathcal{O}(10^{-2})\ M_\odot$ was ejected as a mildly relativistic and mildly isotropic outflow with velocities $\sim 6 - 15\%$ of the speed of light. In contrast to noneccentric mergers, it was found that unbound matter of $\sim \mathcal{O}(10^{-4}) - \mathcal{O}(10^{-3})\ M_{\odot}$ of neutron rich material can be ejected before the merger i.e., during the binary's successive periastron encounters. This would in principle allow for observations of EM emissions before the merger, although observatories would require early notice.

Electromagnetic transients were found compatible with the results from quasi-circular BNS mergers. In general, the considered configurations will be expected to produce kilonovae with luminosities between $10^{39} - 10^{42}$ erg s^{-1} over a time ranging from a few days to two weeks after the merger. On the other hand, the radio flares will be expected to have the largest fluence at $t^{\mathrm{radio}}_{\mathrm{peak}} \sim \mathcal{O}(\mathrm{years})$, similar to equivalent quasi-circular cases.

A characteristic feature for BNSs on eccentric orbits is the superposition of GWs from the quasinormal modes of the NSs (specifically the f-mode) on the GW signal from the binary's orbital motion. These quasinormal modes are excited by the time-varying tidal perturbations of the stars during their periastron passages. A good agreement was found between the f-mode frequency from our simulations for the irrotational cases and the one obtained from the perturbation theory estimate for an equivalent isolated NS. The $(2, 0)$ f-mode signal found in our simulations was accounted for entirely by mode mixing of the intrinsic $(2, \pm 2)$ modes of the stars due to the stars' displacement from the origin. The energy stored in the f-mode oscillations was estimated and found to be increasing with increasing eccentricity. In general, stiff EOSs, as MS1b, were seen to store more energy in the oscillations compared to soft EOSs, e.g. SLy. Additionally, the energy stored in the oscillations of the stars did not always increase monotonically with time. This is to be expected, since for some encounters the tidal perturbations will be out of phase with the already existing oscillations. Overall, these oscillations can store $\sim \mathcal{O}(10^{-8}) - \mathcal{O}(10^{-3})\ M_{\odot}$ of energy depending on eccentricity and the sequence of non-merging encounters.

Additionally, we studied BNSs on precessing orbits in full GR. Initial spin orientation of the stars was varied to obtain misaligned spinning BNS systems. During the evolution some systems were found to show precession or 'wobbling' motion of the entire orbital plane. These systems had their spins asymmetrically misaligned to the orbital angular momentum of the system. Other configurations where the spins were symmetrically misaligned showed 'bobbing' motion of the orbital plane i.e., in this kind of motion the entire orbital plane oscillated in the $z-$direction during the evolution.

The precession cone of the orbital angular momentum for the configurations showing ‘wobbling’ motion had the largest opening angle, which confirmed our findings. Moreover, such precessing systems showed a clear modulation for the (2,1)-mode of the GW signal. The corresponding precession cone for the symmetrically misaligned systems showed no precession of the orbital angular momentum and owing to the symmetry of such systems no precession effects were observed in the (2,1)-mode of the GW signal. Apart from ‘wobbling’ or ‘bobbing’ motion, the spin misaligned systems also showed nutation effect i.e., the spins of the individual stars underwent spin precession during the evolution. The timescale for nutation was found to be shorter as compared to the timescale for the orbital precession. Interestingly, the motion of the orbital plane, ‘wobbling’ or ‘bobbing’ for the spin misaligned systems could be qualitatively explained by considering the general relativistic frame-dragging effect or the Lense-Thirring effect.

Unbound matter $\sim \mathcal{O}(10^{-3}) - \mathcal{O}(10^{-2})\ M_\odot$ for BNSs on precessing orbits was found to be ejected in the late inspiral like their nonprecessing quasi-circular counterparts either from tidal tail ejecta mechanism or from shock heating during the collision of the core of the NSs. Furthermore, as opposed to equal mass quasi-circular BNSs where the matter is expected to be symmetrically ejected, similar setups for precessing BNSs can eject matter asymmetrically due to the ‘wobbling’ or the ‘bobbing’ motion of the system. This asymmetrical ejection of matter is then expected to give a kick to the merged remnant due to linear momentum conservation. In addition to the matter ejecta, GW emission would also play a major role in determining the magnitude and the direction of such kicks.

We investigated DG method for solving the GRHD equations in the context of spectral element methods. We confirmed that with the pure DG method for smooth solutions the expected N-th polynomial order convergence was obtained in a $hp-$ or spectral element method. Once discontinuities formed in the system the method drastically dropped in its accuracy. Therefore, we concluded that the pure DG method was not feasible for accurate and stable numerical evolutions in the context of GRHD equations where shocks and discontinuities can be present, importantly, in the astrophysical scenarios arising in NR.

Further, we tested a new and a robust troubled cell indicator based on the measure of local entropy generation. Compared to conventional indicators, the entropy indicator is advantageous since (i) it does not require cell-averages from the neighboring grids, thereby reducing the data communication in parallel codes and (ii) cell-average based indicators also mark the extrema regions of the solutions as troubled which is not the case with the entropy based indicator. The indicator was tested in shock tube problems in 1D and 2D, and in the Cowling evolution of an isolated TOV star in 3D, where it was shown to mark the problematic regions remarkably well. This was an important step in handling the troubled regions for solutions containing discontinuities.

In the shock tube test in 1D, we tested a minmod slope limiter and a WENO3 limiter which were able to handle the troubled regions although without sharply capturing the discontinuities. Such limiting methods have been employed with varying degrees of success in astrophysical simulations, although most naturally in the context of finite difference or finite volume methods. However, HRSC schemes suffer from major shortcomings in the context of spectral element methods whereby they downgrade the essential feature of spectral element methods i.e, (i) making the spectral scheme resemble more like finite difference or finite volume schemes and (ii) owing to non-locality of the HRSC methods, the spectral schemes with limiting could lead to load imbalance in parallel implementations as a result of their complexity, thereby downgrading the scalability of such spectral codes.

In future a detailed exploration going beyond the conventional methods, for e.g. filtering and HRSC methods, of limiting discontinuous solutions is required in the context of spectral methods. Some techniques that could be tried, but not limited to, are entropy-residual weighted artificial viscosity method, reprojection, and mollification.

Appendix A

Simulation Analysis

For the analysis of the numerical relativity simulations, we briefly summarize the important quantities in the following:

Ejecta mass. We compute the amount of unbound matter ejected following two different methods (i) purely based on the volume integration of the unbound matter (Dietrich et al., 2017b,c), $M_{\text{ej}}^{\mathcal{V}}$, and (ii) computing the matter flux of the unbound material across coordinate spheres sufficiently far from the system, $M_{\text{ej}}^{\mathcal{S}}$; see e.g., (Kastaun et al., 2015; Radice et al., 2016).

In general, we mark matter as unbound if it fulfills

$$u_t < -1 \quad \text{and} \quad v^i x_i > 0\,, \tag{A.1}$$

where $u_t = -W(\alpha - \beta_i v^i)$ is the time component of the fluid 4-velocity (with a lowered index), α is the lapse, β^i is the shift vector, W is the Lorentz factor, and $x^i = (x, y, z)$. For Eq. (A.1) we assume that the fluid elements follow geodesics and requires that the orbit is unbound and has an outward pointing velocity, cf. also (East et al., 2012). The total ejecta mass given by the volume integral is

$$M_{\text{ej}}^{\mathcal{V}} = \int_{\mathcal{V}} \sqrt{\gamma} D \, d^3x\,, \tag{A.2}$$

where the integral is computed in the region,

$$\mathcal{V} = \left\{ x^i = (x, y, z) : u_t < -1 \quad \text{and} \quad v^i x_i > 0 \right\}\,. \tag{A.3}$$

As pointed out in (Dietrich et al., 2017b) a possible drawback is that material which gets ejected and decompresses can obtain densities of the order of the artificial atmosphere, which is added to allow stable GRHD simulations. Once the density drops below the atmosphere value material is not included in the ejecta computation anymore and the ejecta mass is possibly underestimated. For the case where we compute the ejecta mass due to the matter flux across a coordinate sphere this effect is reduced, since the decompression of material outside the coordinate sphere does not influence the ejecta mass computation. Specifically, based on the continuity equation and the Gauss theorem we compute the surface integral unbound mass as,

$$M_{\mathrm{ej}}^{\mathcal{S}} = \int_0^t dt' \int_{r=r_{\mathcal{S}}} [D_u \left(\alpha v^i + \beta^i\right) n_i] r^2 d\Omega, \tag{A.4}$$

where $n_i = x_i/r$ with $r = \sqrt{x^i x_i}$. D_u denotes the unbound fraction of conserved rest mass density $D = W\rho$. The estimates $M_{\mathrm{ej}}^{\mathcal{V}}$ and $M_{\mathrm{ej}}^{\mathcal{S}}$ are compared in Tab. 4.3.

Ejecta kinetic energy. We estimate the kinetic energy of the ejecta as the difference between the total energy E_{ejecta} (that excludes the gravitational-potential energy), the rest-mass, and the total internal energy U_{ejecta} as

$$T_{ej} = E_{ej} - (M_{ej} + U_{ej}) = \int_{\mathcal{V}} \sqrt{\gamma} D \left(e - 1 - \epsilon\right) d^3x \,, \tag{A.5}$$

where $e = \alpha u^t h - p/(\rho \alpha u^t)$.

Ejecta velocity. To estimate the velocity profile for the ejected matter we compute the $D-$weighted integral of $v^2 = v_i v^i$ inside the orbital plane and perpendicular to it,

$$\langle \bar{v} \rangle_\rho = \sqrt{\frac{\int_{\mathcal{V}_{z=0}} \sqrt{\gamma} D \, v^2 \, d^3x}{\int_{\mathcal{V}_{z=0}} \sqrt{\gamma} D \, d^3x}} \,, \tag{A.6}$$

$$\langle \bar{v} \rangle_z = \sqrt{\frac{\int_{\mathcal{V}_{y=0}} \sqrt{\gamma} D \, v^2 \, d^3x}{\int_{\mathcal{V}_{y=0}} \sqrt{\gamma} D \, d^3x}} \,. \tag{A.7}$$

Black hole properties. A black hole is characterized by its horizon mass M_{BH} and dimensionful spin J_{BH},

$$J_{BH} = \frac{1}{8\pi} \oint \phi^l \, R^m \, K_{ml} \, dA \, , \tag{A.8}$$

$$M_{BH} = \sqrt{\frac{A_{BH}}{16\pi} + \frac{4\pi J_{BH}^2}{A_{BH}}} \, , \tag{A.9}$$

where A_{BH} is the surface area of the horizon, dA is the area element of the surface, ϕ^l is a vector field tangent to the surface satisfying $\mathcal{L}_{\boldsymbol{\phi}} q_{ij} = 0$, where q_{ij} is the induced metric on the horizon; cf. (Thornburg, 2007) for more details.

The accretion disk around the BH has a mass of

$$M_{disk} = \int_{r>r_{AH}} \sqrt{\gamma} D \, d^3x \, , \tag{A.10}$$

where the integration domain excludes the interior of the BH.

Quasi-local spin measure for NS. We evaluate the surface integral

$$S^i \approx \frac{1}{8\pi} \int_{r_s} \sqrt{\gamma} \left(\gamma^{kj} K_{lk} - \delta^j_l K \right) n_j \phi^{li} \, d^2x \, , \tag{A.11}$$

on coordinate spheres with radius r_s around the NSs. $\phi^{li} = \epsilon^{lik} x_k$ defines the approximate rotational Killing vectors in Cartesian coordinates $(\phi^{l1}, \phi^{l2}, \phi^{l3})$, K_{ij} denotes the extrinsic curvature, γ_{ij} the inverse 3-metric, and $n_i = (x_i - x_i^{NS})/r$ the normal vector with respect to the center of the NS. The center is given by the minimum of the lapse inside the NS. Note that the radius should not be chosen too small so that it does not cover all of the tidally deformed star, whereas if the radius is chosen too large the measurement gets affected by the companion star.

In dynamical BNS evolutions, Eq. (A.11) gives us a measure of the spin evolution and spin direction. However, it is to be noted that this measure of spin has a few shortcomings: (i) unambiguous definition of spin of a single object in a binary system does not exist in general relativity; (ii) although in numerical relativity Eq. (A.11) is evaluated in the strong-field region, it is only well defined at spatial infinity; (iii) the choice of the coordinate spheres (r_s) on which the spin is measured are gauge dependent.

Spectrograms. As encountered in Sec. 4.4, density oscillations can be induced in the stars during close encounters on highly eccentric orbits. Most of the oscillation energy is released in the f-modes which imprint their own characteristic GWs on top of the GWs generated by the orbital motion. In order to study these f-mode oscillations, we consider the spectrograms of the individual, $\ell = 2$, dominant modes of the curvature scalar $r\Psi_4$.

We compute the frequency domain GW signal $r\tilde{\Psi}_4^{\ell m}(f)$ using the discrete Fourier transform implemented in MATLAB for time intervals of length $t_2 - t_1$. The corresponding power spectral density (PSD) is given by

$$\mathrm{PSD}(r\Psi_4^{\ell m})(f) = (t_2 - t_1)^2 \left| r\tilde{\Psi}_4^{\ell m}(f) \right|^2 \tag{A.12}$$

to get the distribution of power into frequency components. This gives us a time series distribution of power and frequency, disentangling the dynamics of the system. From the spectrograms we find the frequency at which the NSs oscillate and also other frequencies of the dominant dynamics like inspiral, merger[1] and the oscillations of the merger remnant.

Removing displacement-induced mode mixing from the GW signal:- Since we are considering symmetric systems, the f-mode oscillations seen in the waveform will be twice those of an individual star. However, because the stars are not located at the origin, there will be some mode mixing which can not be neglected. Thus, it is not possible to simply divide the f-mode contribution to a given mode by 2 to obtain the contribution from an individual star that would be extracted if it was at rest at the origin.

To obtain approximate expressions for an individual star's multipole moments (as would be extracted with it at the origin), we will consider times when the stars are well-separated and approximately separate the f-mode signal from the signal from the orbit by taking a moving average of $\Psi^4_{2,\pm 2}$ with a window width given by the period of the f-mode.[2] Specifically, we define $\Psi^{4,f\text{-mode}}_{2,\pm 2} := \Psi^4_{2,\pm 2} - \Psi^{4,\text{avg}}_{2,\pm 2}$, where $\Psi^{4,\text{avg}}_{2,\pm 2}$ denotes the result of applying the moving average to $\Psi^4_{2,\pm 2}$.

---

[1] Note that we define the moment of merger as the peak in the amplitude of the GW strain, rh_{22}.

[2] Here and in all other mode mixing analysis, we denote the (ℓ, m) mode of Ψ_4 by $\Psi^4_{\ell,m}$, for notational simplicity.

Additionally, since the decay times of the f-mode oscillations are much longer than the time between periastra, one can treat the f-mode signal from a single star in a given $(\ell_{\rm i}, m_{\rm i})$ mode as a simple sinusoid, $\Psi^{4,f\text{-mode}}_{\ell_{\rm i},m_{\rm i}} e^{i\omega_{f\text{-mode}}t}$, and can compute the mode mixing due to the stars' displacement from the origin analytically using Eq. (43b) in (Boyle, 2016) (summing the series to obtain an exponential). This mode mixing is due to the variations in the retarded time at different points on the extraction sphere; we compute the retarded time approximately using the coordinate tracks of the stars. We thus take the retarded time to be $t_{\rm ret,0} + \alpha(\theta, \phi)$, where $t_{\rm ret,0}$ denotes the retarded time for a source at the origin, and $\alpha(\theta, \phi) = d_1 \sin\theta \cos(\phi - \Upsilon)$ [cf. the discussion above Eq. (4) in (Boyle, 2016)]. Here θ, ϕ are the angular spherical coordinates on the extraction surface and $d_1(\cos\Upsilon, \sin\Upsilon, 0)$ is the coordinate track of star 1; the negative of this gives the track of the star's companion.[3] Additionally, we take each star to only have an intrinsic $(\ell_{\rm i}, m_{\rm i})$ mode, since we can include further modes by linearity. Thus, the f-mode contribution to the (spin-weighted) spherical harmonic modes extracted from the evolution of the binary will be given by

$$\begin{aligned}\Psi^{4,\rm ext}_{\ell,m} &= 2\Psi^{4,f\text{-mode}}_{\ell_{\rm i},m_{\rm i}} \int_{S^2} \cos[d_1\omega_{f\text{-mode}} \sin\theta\cos(\phi - \Upsilon)] \\ &\quad \times {}_{-2}Y_{\ell_{\rm i},m_{\rm i}}(\theta,\phi)\,{}_{-2}Y^*_{\ell,m}(\theta,\phi)\,d\Omega \\ &=: \mu_{\ell_{\rm i},m_{\rm i};\ell,m}\Psi^{4,f\text{-mode}}_{\ell_{\rm i},m_{\rm i}},\end{aligned} \tag{A.13}$$

where ${}_{-2}Y_{\ell m}$ is the spin-(-2)-weighted spherical harmonic, the star denotes the complex conjugate, and we have defined the mode mixing coefficient $\mu_{\ell_{\rm i},m_{\rm i};\ell,m}$, which describes mixing from the $(\ell_{\rm i}, m_{\rm i})$ intrinsic mode of an individual star into the (ℓ, m) mode of the binary. Note that we have $\mu_{\ell_{\rm i},m_{\rm i};\ell,m} = \mu^*_{\ell,m;\ell_{\rm i},m_{\rm i}}$.

---

[3] Here we are assuming that the binary's center-of-mass (COM) is at the origin, for simplicity of exposition. The COM actually drifts over the course of evolution, and its displacement from the origin is considerable in a few cases (increasing with decreasing eccentricity). We will discuss later how to account for this drift in the mode mixing analysis.

Defining $\zeta := d_1\omega_{f\text{-mode}}$, we obtain mode mixing coefficients of

$$\begin{aligned}
\mu_{2,\pm2;2,\pm2} &= \frac{5}{8}\mathcal{S}(-3,-3;\zeta) \\
&= 2 - \frac{5}{21}\zeta^2 + O(\zeta^4), && \text{(A.14a)} \\
\mu_{2,0;2,0} &= \frac{15}{4}\mathcal{S}(-3,1;\zeta) \\
&= 2 - \frac{3}{7}\zeta^2 + O(\zeta^4), && \text{(A.14b)} \\
\mu_{2,\pm2;2,0} &= \frac{5e^{\pm2i\Upsilon}}{4}\sqrt{\frac{3}{2}}\mathcal{S}(5,1;\zeta) \\
&= -\frac{2e^{\pm2i\Upsilon}}{7\sqrt{6}}\zeta^2 + O(\zeta^4), && \text{(A.14c)} \\
\mu_{2,\pm2;2,\mp2} &= \frac{5e^{\pm4i\Upsilon}}{8}\mathcal{S}(-35,5;\zeta) \\
&= \frac{e^{\pm4i\Upsilon}}{1512}\zeta^4 + O(\zeta^6), && \text{(A.14d)}
\end{aligned}$$

where

$$\begin{aligned}
\mathcal{S}(a,b;z) &:= \frac{z(3a+2bz^2)\cos z + [-3a+(a-2b)z^2+z^4]\sin z}{z^5} \\
&= -a\frac{j_2(z)}{z^2} - 2b\frac{j_1(z)}{z} + j_0(z)
\end{aligned} \tag{A.15}$$

is a sinc-like function; we also give the expression in terms of the spherical Bessel functions of the first kind, j_ℓ. We give the first few terms of the power series expansions to give intuition about the behavior of the mixing coefficients for small ζ. We do not give the mixing coefficients involving the $(2,\pm1)$ modes, as they vanish, due to the symmetry of the system (since we are assuming that the binary's center-of-mass is at the origin in the current discussion). While the $\mu_{2,\pm2;2,\mp2}$ coefficients do not vanish, they are suppressed by higher powers of ζ, only starting at $O(\zeta^4)$, and are small enough for the situations we are considering (magnitudes < 0.03) such that we will simply ignore them and focus on the much larger effects from the other mixing coefficients given above. Similarly, we do not consider mixing of higher-ℓ modes into the $\ell = 2$ modes, since we expect those modes to have intrinsically smaller amplitudes, compared with the $\ell = 2$ modes.

We also do not consider mode mixing due to the boosts, since the speeds due to the binary's orbital motion are relatively small (< 0.15) in the region between bursts, where the stars are well separated and the contributions from the mode mixing due to displacement from the origin are largest: The linear-in-velocity contribution to the mode mixing due to the boost vanishes, due to the symmetry of the binary (see (Gualtieri et al., 2008) for explicit expressions in the linearized case; the general computation is discussed in (Boyle, 2016)).

If one needs to include the displacement of the binary's center-of-mass from the origin, then it is simple to convert the expressions above to cover the general case: The contribution from a single star is just half of the total, so if the two stars are located at $d_1(\cos\Upsilon_1, \sin\Upsilon_1, 0)$ and $-d_2(\cos\Upsilon_2, \sin\Upsilon_2, 0)$, respectively, then, defining $\zeta_A := d_A\omega_{f\text{-mode}}$ with $A \in \{1,2\}$, we have, e.g.,

$$\mu^{\text{general}}_{2,\pm2;2,0} = \frac{5}{8}\sqrt{\frac{3}{2}}\sum_{A=1}^{2} e^{\pm 2i\Upsilon_A}\mathcal{S}(5,1;\zeta_A). \tag{A.16}$$

We use these general expressions for all the results presented in the thesis, though the simpler expressions with the center-of-mass at the origin suffice in almost all cases. Additionally, for completeness, we also give the mixing from the intrinsic $(2,\pm2)$ modes into the $(2,\pm1)$ modes, though we do not consider these further in this thesis:

$$\begin{aligned}\mu^{\text{general}}_{2,\pm2;2,\pm1} &= \frac{5i}{8}\sum_{A=1}^{2}(-1)^A e^{\pm i\Upsilon_A}\mathcal{T}(3,1;\zeta_A)\\ &= \frac{i}{3}(\zeta_1 e^{\pm i\Upsilon_1} - \zeta_2 e^{\pm i\Upsilon_2}) + O(\zeta_{1,2}^3), &\text{(A.17a)}\\ \mu^{\text{general}}_{2,\pm2;2,\mp1} &= \frac{5i}{8}\sum_{A=1}^{2}(-1)^A e^{\pm 3i\Upsilon_A}\mathcal{T}(-5,-3;\zeta_A)\\ &= -\frac{i}{168}(\zeta_1^3 e^{\pm 3i\Upsilon_1} - \zeta_2^3 e^{\pm 3i\Upsilon_2}) + O(\zeta_{1,2}^5), &\text{(A.17b)}\end{aligned}$$

where

$$\begin{aligned}\mathcal{T}(a,b;z) &:= \frac{z(3a+z^2)\cos z + (-3a+2bz^2)\sin z}{z^4}\\ &= -3a\frac{j_1(z)}{z^2} + 2b\frac{j_0(z)}{z} - y_0(z).\end{aligned} \tag{A.18}$$

Here y_ℓ are the spherical Bessel functions of the second kind. [Note that Mathematica (at least as of version 11) will not evaluate the θ integral giving the second of these mixing coefficients as is. However, if one uses the Maclaurin series for the

Bessel function one obtains upon performing the ϕ integral first, and then integrates term-by-term, Mathematica will sum the resulting infinite series with no problems.]

Appendix B

Radiated Energy and Angular Momentum in GWs

To compute the amount of energy and angular-momentum radiated away from the system in the form of gravitational radiation we use the relations as given in (Alcubierre, 2008, Pg. 316). The energy is computed from the time integral of,

$$\frac{dE}{dt} = \lim_{r\to\infty} \frac{r^2}{16\pi} \sum_{\ell,m} \left| \int_{-\infty}^{t} A^{\ell,m}\, dt' \right|^2, \tag{B.1}$$

and the angular-momentum vector is estimated from the time integral of,

$$\begin{aligned} \frac{dJ_x}{dt} =& -\lim_{r\to\infty} \frac{ir^2}{32\pi}\, \mathbf{Im} \left\{ \sum_{\ell,m} \int_{-\infty}^{t} \int_{-\infty}^{t'} A^{\ell,m}\, dt''\, dt' \right. \\ & \left. \times \int_{-\infty}^{t} \left(f_{\ell,m} A^{*\ell,m+1} + f_{\ell,-m} A^{*\ell,m-1} \right) dt' \right\}, \end{aligned} \tag{B.2}$$

$$\begin{aligned} \frac{dJ_y}{dt} =& -\lim_{r\to\infty} \frac{r^2}{32\pi}\, \mathbf{Re} \left\{ \sum_{\ell,m} \int_{-\infty}^{t} \int_{-\infty}^{t'} A^{\ell,m}\, dt''\, dt' \right. \\ & \left. \times \int_{-\infty}^{t} \left(f_{\ell,m} A^{*\ell,m+1} - f_{\ell,-m} A^{*\ell,m-1} \right) dt' \right\}, \end{aligned} \tag{B.3}$$

$$\begin{aligned} \frac{dJ_z}{dt} =& -\lim_{r\to\infty} \frac{ir^2}{16\pi}\, \mathbf{Im} \left\{ \sum_{\ell,m} m \int_{-\infty}^{t} \int_{-\infty}^{t'} A^{\ell,m}\, dt''\, dt' \right. \\ & \left. \times \int_{-\infty}^{t} A^{*\ell,m}\, dt' \right\}, \end{aligned} \tag{B.4}$$

where, $f_{\ell,m} := \sqrt{(\ell-m)(\ell+m+1)} = \sqrt{\ell(\ell+1)-m(m+1)}$ and $\mathbf{Im}(a+ib) = ib$ for real a and b. Note that, $\int_{-\infty}^{t} A_{\ell,m}\, dt' = \dot{h}_{\ell m}(t)$ (where a dot denotes a time derivative) and $\int_{-\infty}^{t} \int_{-\infty}^{t'} A_{\ell,m}\, dt''\, dt' = h_{\ell m}(t)$. A '*' in the above formulas denotes a complex conjugate. Moreover,

$$\begin{aligned} A_{\ell,m} &= \langle {}_{-2}Y_{\ell,m}, \Psi_4 \rangle \\ &= \int_0^{2\pi} \int_0^{\pi} \Psi_4 \; {}_{-2}Y^*_{\ell,m} \; \sin\theta \; d\theta d\phi, \end{aligned} \tag{B.5}$$

where again ${}_{-2}Y_{l,m}$ is the spherical harmonic of spin weight -2.

Bibliography

Abbott, Benjamin P. et al. (2018). Prospects for Observing and Localizing Gravitational-Wave Transients with Advanced LIGO, Advanced Virgo and KAGRA, *Living Rev. Relativity* **21**, p. 3. DOI: `10.1007/s41114-018-0012-9,10.1007/lrr-2016-1`. arXiv: `1304.0670 [gr-qc]`.

Abbott, B. P. et al. (2016a). Observation of Gravitational Waves from a Binary Black Hole Merger, *Phys. Rev. Lett.* **116**, no. 6, p. 061102. DOI: `10.1103/PhysRevLett.116.061102`. arXiv: `1602.03837 [gr-qc]`.

— (2016b). The Rate of Binary Black Hole Mergers Inferred from Advanced LIGO Observations Surrounding GW150914, *Astrophys. J. Lett.* **833**, no. 1, p. L1. DOI: `10.3847/2041-8205/833/1/L1`. arXiv: `1602.03842 [astro-ph.HE]`.

— (2017d). Search for Post-merger Gravitational Waves from the Remnant of the Binary Neutron Star Merger GW170817, *Astrophys. J. Lett.* **851**, no. 1, p. L16. DOI: `10.3847/2041-8213/aa9a35`. arXiv: `1710.09320 [astro-ph.HE]`.

— (2017a). Estimating the Contribution of Dynamical Ejecta in the Kilonova Associated with GW170817, *Astrophys. J. Lett.* **850**, no. 2, p. L39. DOI: `10.3847/2041-8213/aa9478`. arXiv: `1710.05836 [astro-ph.HE]`.

— (2019). GWTC-1: A Gravitational-Wave Transient Catalog of Compact Binary Mergers Observed by LIGO and Virgo during the First and Second Observing Runs, *Phys. Rev. X* **9** (3), p. 031040. DOI: `10.1103/PhysRevX.9.031040`.

— (2020). GW190425: Observation of a Compact Binary Coalescence with Total Mass $\sim 3.4 M_{\odot}$, arXiv: `2001.01761 [astro-ph.HE]`.

Ajith, P. et al. (2011). Inspiral-merger-ringdown waveforms for black-hole binaries with non-precessing spins, *Phys. Rev. Lett.* **106**, p. 241101. DOI: `10.1103/PhysRevLett.106.241101`. arXiv: `0909.2867 [gr-qc]`.

Alcubierre, Miguel et al. (2003). Gauge conditions for long term numerical black hole evolutions without excision, *Phys. Rev. D* **67**, p. 084023. DOI: `10.1103/PhysRevD.67.084023`. arXiv: `gr-qc/0206072 [gr-qc]`.

Alcubierre, M. (2008). *Introduction to 3+1 Numerical Relativity*. Ed. by M. Alcubierre. Oxford University Press.

Andersson, N. et al. (2011). Gravitational waves from neutron stars: Promises and challenges, *Gen. Rel. Grav.* **43**, pp. 409–436. DOI: `10.1007/s10714-010-1059-4`. arXiv: `0912.0384 [astro-ph.SR]`.

Anile, A. M. (1990). *Relativistic Fluids and Magneto-fluids*.

Arnowitt, Richard et al. (2008). Republication of: The dynamics of general relativity, *General Relativity and Gravitation* **40**, no. 9, pp. 1997–2027. ISSN: 1572-9532. DOI: `10.1007/s10714-008-0661-1`.

Asmodelle, Estelle (2017). *Tests of General Relativity: A Review*. arXiv: `1705.04397 [gr-qc]`.

Baade, W. et al. (1934). Cosmic Rays from Super-Novae, *Proceedings of the National Academy of Sciences* **20**, no. 5, pp. 259–263. ISSN: 0027-8424. DOI: `10.1073/pnas.20.5.259`.

Baiotti, Luca et al. (2003). A new three-dimensional general-relativistic hydrodynamics code, *Mem. S.A.It. Suppl.* **1**, p. 210. arXiv: `1004.3849 [gr-qc]`.

Baiotti, Luca et al. (2017). Binary neutron star mergers: a review of Einsteins richest laboratory, *Rept. Prog. Phys.* **80**, no. 9, p. 096901. DOI: `10.1088/1361-6633/aa67bb`. arXiv: `1607.03540 [gr-qc]`.

Baker, John G. et al. (2006). Binary black hole merger dynamics and waveforms, *Phys. Rev. D* **73**, p. 104002. eprint: `gr-qc/0602026`.

Ballmer, Stefan et al. (2015). New Technologies in Gravitational-Wave Detection, *Ann. Rev. Nucl. Part. Sci.* **65**, pp. 555–577. DOI: `10.1146/annurev-nucl-102014-022017`.

Banyuls, Francesc et al. (1997). Numerical 3+1 General Relativistic Hydrodynamics: A Local Characteristic Approach, *Astrophys. J.* **476**, p. 221.

Barack, Leor et al. (2003). Gravitational selfforce on a particle orbiting a Kerr black hole, *Phys. Rev. Lett.* **90**, p. 111101. DOI: `10.1103/PhysRevLett.90.111101`. arXiv: `gr-qc/0212103 [gr-qc]`.

Baumgarte, Thomas W. et al. (1998). On the numerical integration of Einstein's field equations, *Phys. Rev. D* **59**, p. 024007. DOI: `10.1103/PhysRevD.59.024007`. arXiv: `gr-qc/9810065`.

Baumgarte, Thomas W. et al. (2000). On the Maximum Mass of Differentially Rotating Neutron Stars, *Astrophys. J. Lett.* **528**, p. L29. arXiv: `astro-ph/9910565`.

Baumgarte, Thomas et al. (2010). *Numerical Relativity*. Cambridge: Cambridge University Press.

Bauswein, A. et al. (2010). Testing Approximations of Thermal Effects in Neutron Star Merger Simulations, *Phys. Rev. D* **82**, p. 084043. DOI: `10.1103/PhysRevD.82.084043`. arXiv: `1006.3315 [astro-ph.SR]`.

Bernuzzi, Sebastiano et al. (2010). Constraint violation in free evolution schemes: comparing BSSNOK with a conformal decomposition of Z4, *Phys. Rev. D* **81**, p. 084003. DOI: `10.1103/PhysRevD.81.084003`. arXiv: `0912.2920 [gr-qc]`.

Bernuzzi, Sebastiano et al. (2012). Accuracy of numerical relativity waveforms from binary neutron star mergers and their comparison with post-Newtonian waveforms, *Phys. Rev. D* **85**, p. 104030. DOI: `10.1103/PhysRevD.85.104030`. arXiv: `1109.3611 [gr-qc]`.

Bernuzzi, Sebastiano et al. (2014a). Mergers of binary neutron stars with realistic spin, *Phys. Rev. D* **89**, p. 104021. DOI: `10.1103/PhysRevD.89.104021`. arXiv: `1311.4443 [gr-qc]`.

Bernuzzi, Sebastiano et al. (2014b). Quasi-universal properties of neutron star mergers, *Phys. Rev. Lett.* **112**, p. 201101. DOI: `10.1103/PhysRevLett.112.201101`. arXiv: `1402.6244 [gr-qc]`.

Bernuzzi, Sebastiano et al. (2015). Modeling the Dynamics of Tidally Interacting Binary Neutron Stars up to the Merger, *Phys. Rev. Lett.* **114**, no. 16, p. 161103. DOI: `10.1103/PhysRevLett.114.161103`. arXiv: `1412.4553 [gr-qc]`.

Bernuzzi, Sebastiano et al. (2016b). How loud are neutron star mergers?, *Phys. Rev. D* **94**, no. 2, p. 024023. DOI: `10.1103/PhysRevD.94.024023`. arXiv: `1512.06397 [gr-qc]`.

Bernuzzi, Sebastiano et al. (2016a). Gravitational waveforms from binary neutron star mergers with high-order weighted-essentially-nonoscillatory schemes in numerical relativity, *Phys. Rev. D* **94**, no. 6, p. 064062. DOI: `10.1103/PhysRevD.94.064062`. arXiv: `1604.07999 [gr-qc]`.

Blanchet, Luc (2006). Gravitational radiation from post-Newtonian sources and inspiralling compact binaries, *Living Rev. Rel.* **9**, p. 4.

Bona, C. et al. (1996). “A Class Of Hyperbolic Gauge Conditions”, *The Seventh Marcel Grossmann Meeting: On Recent Developments in Theoretical and Experimental General Relativity, Gravitation, and Relativistic Field Theories*. Ed. by R. T. Jantzen et al. Singapore: World Scientific.

Bona, C. et al. (1995). New Formalism for Numerical Relativity, *Phys. Rev. Lett.* **75**, pp. 600–603. eprint: `gr-qc/9412071`.

Borges, Rafael et al. (2008). An improved weighted essentially non-oscillatory scheme for hyperbolic conservation laws, *J. Comput. Phys.* **227**, no. 6, pp. 3191–3211. ISSN: 0021-9991. DOI: `10.1016/j.jcp.2007.11.038`.

Boyle, Michael (2016). Transformations of asymptotic gravitational-wave data, *Phys. Rev. D* **93**, no. 8, p. 084031. DOI: `10.1103/PhysRevD.93.084031`. arXiv: `1509.00862 [gr-qc]`.

Brügmann, Bernd et al. (2008). Calibration of Moving Puncture Simulations, *Phys. Rev. D* **77**, p. 024027. DOI: `10.1103/PhysRevD.77.024027`. arXiv: `gr-qc/0610128 [gr-qc]`.

Bugner, Marcus et al. (2016). Solving 3D relativistic hydrodynamical problems with weighted essentially nonoscillatory discontinuous Galerkin methods, *Phys. Rev. D* **94**, no. 8, p. 084004. DOI: `10.1103/PhysRevD.94.084004`. arXiv: `1508.07147 [gr-qc]`.

Bugner, Marcus (2017). "Discontinuous galerkin methods for general relativistic hydrodynamics". Dissertation, Friedrich-Schiller-Universität Jena, 2017. PhD thesis. Jena. DOI: `10.22032/dbt.33822`.

Buonanno, A. et al. (1999). Effective one-body approach to general relativistic two-body dynamics, *Phys. Rev. D* **59**, p. 084006. DOI: `10.1103/PhysRevD.59.084006`. arXiv: `gr-qc/9811091`.

Camenzind, Max (2007). *Compact objects in astrophysics : white dwarfs, neutron stars, and black holes*. Springer-Verlag. DOI: `10.1007/978-3-540-49912-1`.

Campanelli, Manuela et al. (2006). Spinning-black-hole binaries: The orbital hang up, *Phys. Rev. D* **74**, p. 041501. DOI: `10.1103/PhysRevD.74.041501`. arXiv: `gr-qc/0604012 [gr-qc]`.

Carroll, Sean (2003). *Spacetime and Geometry: An Introduction to General Relativity*. Cambridge University Press. ISBN: 978-1-108-48839-6. DOI: `10.1017/9781108770385`.

Chan, T. K. et al. (2014). Multipolar universal relations between f-mode frequency and tidal deformability of compact stars, *Phys. Rev. D* **90**, no. 12, p. 124023. DOI: `10.1103/PhysRevD.90.124023`. arXiv: `1408.3789 [gr-qc]`.

Chaurasia, Swami Vivekanandji et al. (2018). Gravitational waves and mass ejecta from binary neutron star mergers: Effect of large eccentricities, *Phys. Rev. D* **98**, no. 10, p. 104005. DOI: `10.1103/PhysRevD.98.104005`. arXiv: `1807.06857 [gr-qc]`.

Chaurasia, Swami Vivekanandji et al. (2020). Gravitational waves and mass ejecta from binary neutron star mergers: Effect of spin orientation, arXiv: 2003.11901 [gr-qc].

Chirenti, Cecilia et al. (2015). Fundamental oscillation modes of neutron stars: validity of universal relations, *Phys. Rev. D* **91**, no. 4, p. 044034. DOI: 10.1103/PhysRevD.91.044034. arXiv: 1501.02970 [gr-qc].

Chirenti, Cecilia et al. (2017). Gravitational waves from f-modes excited by the inspiral of highly eccentric neutron star binaries, *Astrophys. J.* **837**, no. 1, p. 67. DOI: 10.3847/1538-4357/aa5ebb. arXiv: 1612.07097 [astro-ph.HE].

Clark, James Alexander et al. (2016). Observing Gravitational Waves From The Post-Merger Phase Of Binary Neutron Star Coalescence, *Classical Quantum Gravity* **33**, no. 8, p. 085003. DOI: 10.1088/0264-9381/33/8/085003. arXiv: 1509.08522 [astro-ph.HE].

CoRe (2018). Database of binary neutron star merger waveforms. http://www.computational-relativity.org/.

Cowling, T. G. (1941). The non-radial oscillations of polytropic stars, *Mon. Not. Roy. Astron. Soc.* **101**, p. 367.

Damour, Thibault (2001). Coalescence of two spinning black holes: An effective one-body approach, *Phys. Rev. D* **64**, p. 124013. DOI: 10.1103/PhysRevD.64.124013. arXiv: gr-qc/0103018.

Damour, Thibault et al. (2012). Energy versus Angular Momentum in Black Hole Binaries, *Phys. Rev. Lett.* **108**, p. 131101. DOI: 10.1103/PhysRevLett.108.131101. arXiv: 1110.2938 [gr-qc].

Dietrich, Tim et al. (2015b). Numerical relativity simulations of neutron star merger remnants using conservative mesh refinement, *Phys. Rev. D* **91**, no. 12, p. 124041. DOI: 10.1103/PhysRevD.91.124041. arXiv: 1504.01266 [gr-qc].

Dietrich, Tim et al. (2015a). Binary Neutron Stars with Generic Spin, Eccentricity, Mass ratio, and Compactness - Quasi-equilibrium Sequences and First Evolutions, *Phys. Rev. D* **92**, no. 12, p. 124007. DOI: 10.1103/PhysRevD.92.124007. arXiv: 1507.07100 [gr-qc].

Dietrich, Tim et al. (2017d). Modeling dynamical ejecta from binary neutron star mergers and implications for electromagnetic counterparts, *Classical Quantum Gravity* **34**, no. 10, p. 105014. DOI: 10.1088/1361-6382/aa6bb0. arXiv: 1612.03665 [gr-qc].

Dietrich, Tim et al. (2017b). Gravitational waves and mass ejecta from binary neutron star mergers: Effect of the mass-ratio, *Phys. Rev. D* **95**, no. 2, p. 024029. DOI: `10.1103/PhysRevD.95.024029`. arXiv: `1607.06636 [gr-qc]`.

Dietrich, Tim et al. (2017c). Gravitational waves and mass ejecta from binary neutron star mergers: Effect of the stars' rotation, *Phys. Rev. D* **95**, no. 4, p. 044045. DOI: `10.1103/PhysRevD.95.044045`. arXiv: `1611.07367 [gr-qc]`.

Dietrich, Tim et al. (2017a). Comprehensive comparison of numerical relativity and effective-one-body results to inform improvements in waveform models for binary neutron star systems, *Phys. Rev. D* **95**, no. 12, p. 124006. DOI: `10.1103/PhysRevD.95.124006`. arXiv: `1702.02053 [gr-qc]`.

Dietrich, Tim et al. (2018c). Numerical Relativity Simulations of Precessing Binary Neutron Star Mergers, *Phys. Rev. D* **97**, no. 6, p. 064002. DOI: `10.1103/PhysRevD.97.064002`. arXiv: `1712.02992 [gr-qc]`.

Dietrich, Tim et al. (2018a). CoRe database of binary neutron star merger waveforms, *Class. Quant. Grav.* **35**, no. 24, 24LT01. DOI: `10.1088/1361-6382/aaebc0`. arXiv: `1806.01625 [gr-qc]`.

Dietrich, Tim et al. (2018b). "High-resolution numerical relativity simulations of spinning binary neutron star mergers", arXiv: `1803.07965 [gr-qc]`.

Doneva, Daniela D. et al. (2013). Gravitational wave asteroseismology of fast rotating neutron stars with realistic equations of state, *Phys. Rev. D* **88**, no. 4, p. 044052. DOI: `10.1103/PhysRevD.88.044052`. arXiv: `1305.7197 [astro-ph.SR]`.

Dudi, Reetika et al. (2018). Relevance of tidal effects and post-merger dynamics for binary neutron star parameter estimation, *Phys. Rev. D* **98**, no. 8, p. 084061. DOI: `10.1103/PhysRevD.98.084061`. arXiv: `1808.09749 [gr-qc]`.

East, William E. et al. (2012). Dynamical Capture Binary Neutron Star Mergers, *Astrophys. J. Lett.* **760**, p. L4. DOI: `10.1088/2041-8205/760/1/L4`. arXiv: `1208.5279 [astro-ph.HE]`.

East, William E. et al. (2016b). Relativistic Simulations of Eccentric Binary Neutron Star Mergers: One-arm Spiral Instability and Effects of Neutron Star Spin, *Phys. Rev. D* **93**, no. 2, p. 024011. DOI: `10.1103/PhysRevD.93.024011`. arXiv: `1511.01093 [astro-ph.HE]`.

East, William E. et al. (2016a). Equation of state effects and one-arm spiral instability in hypermassive neutron stars formed in eccentric neutron star mergers, *Classical Quantum Gravity* **33**, no. 24, p. 244004. DOI: `10.1088/0264-9381/33/24/244004`. arXiv: `1609.00725 [astro-ph.HE]`.

East, William E. et al. (2019). Binary neutron star mergers: Effects of spin and post-merger dynamics, *Phys. Rev. D* **100**, no. 12, p. 124042. DOI: `10.1103/PhysRevD.100.124042`. arXiv: `1906.05288 [astro-ph.HE]`.

Eichler, David et al. (1989). Nucleosynthesis, Neutrino Bursts and Gamma-Rays from Coalescing Neutron Stars, *Nature* **340**, pp. 126–128. DOI: `10.1038/340126a0`.

Einstein, Albert (1915). The Field Equations of Gravitation, *Sitzungsber. Preuss. Akad. Wiss. Berlin (Math. Phys.)* **1915**, pp. 844–847.

Abbott, Benjamin P. et al. (2017e). Exploring the Sensitivity of Next Generation Gravitational Wave Detectors, *Classical Quantum Gravity* **34**, no. 4, p. 044001. DOI: `10.1088/1361-6382/aa51f4`. arXiv: `1607.08697 [astro-ph.IM]`.

Farr, Will M. et al. (2011). Spin Tilts in the Double Pulsar Reveal Supernova Spin Angular-Momentum Production, *Astrophys. J.* **742**, p. 81. DOI: `10.1088/0004-637X/742/2/81`. arXiv: `1104.5001 [astro-ph.HE]`.

Font, Jose A. et al. (2000). Nonlinear hydrodynamical evolution of rotating relativistic stars: Numerical methods and code tests, *Mon. Not. Roy. Astron. Soc.* **313**, p. 678. DOI: `10.1046/j.1365-8711.2000.03254.x`. arXiv: `gr-qc/9908010`.

Font, Jose A. (2007). Numerical hydrodynamics and magnetohydrodynamics in general relativity, *Living Rev. Rel.* **11**, p. 7.

Gassner, Gregor et al. (2011). A Comparison of the Dispersion and Dissipation Errors of Gauss and Gauss-Lobatto Discontinuous Galerkin Spectral Element Methods, *SIAM J. Sci. Comput.* **33**, no. 5, pp. 2560–2579. ISSN: 1064-8275. DOI: `10.1137/100807211`.

Abbott, B. P. et al. (2017c). Multi-messenger Observations of a Binary Neutron Star Merger, *Astrophys. J. Lett.* **848**, p. L12. DOI: `10.3847/2041-8213/aa91c9`. arXiv: `1710.05833 [astro-ph.HE]`.

Gibbs, J. (1898). Fourier's Series, *Nature* **59**, p. 200. DOI: `10.1038/059200b0`.

Gottlieb, David et al. (1985). "Recovering Pointwise Values of Discontinuous Data within Spectral Accuracy", *Progress and Supercomputing in Computational Fluid Dynamics: Proceedings of U.S.-Israel Workshop, 1984*. Ed. by Earll M. Murman et al. Boston, MA: Birkhäuser Boston, pp. 357–375. ISBN: 978-1-4612-5162-0. DOI: `10.1007/978-1-4612-5162-0_19`.

Gottlieb, David et al. (1992). On the Gibbs phenomenon I: recovering exponential accuracy from the Fourier partial sum of a nonperiodic analytic function, *Journal of Computational and Applied Mathematics* **43**, no. 1, pp. 81 –98. ISSN: 0377-0427. DOI: `10.1016/0377-0427(92)90260-5`.

Gottlieb, Sigal et al. (2011). A Review of David Gottlieb's Work on the Resolution of the Gibbs Phenomenon, *Communications in Computational Physics* **9**, no. 3, pp. 497–519. DOI: `10.4208/cicp.301109.170510s`.

Gourgoulhon, Eric (2012). *3+1 Formalism In General Relativity*. ISBN: 978-3-642-24524-4. DOI: `10.1007/978-3-642-24525-1`.

Grandclément, Philippe et al. (2009). Spectral Methods for Numerical Relativity, *Living Reviews in Relativity* **12**, no. 1, p. 1. ISSN: 1433-8351. DOI: `10.12942/lrr-2009-1`.

Gualtieri, Leonardo et al. (2008). Transformation of the multipolar components of gravitational radiation under rotations and boosts, *Phys. Rev. D* **78**, p. 044024. DOI: `10.1103/PhysRevD.78.044024`. arXiv: `0805.1017 [gr-qc]`.

Guercilena, Federico et al. (2017). Entropy-limited hydrodynamics: a novel approach to relativistic hydrodynamics, *Comput. Astrophys. Cosmol.* **4**, p. 3. DOI: `10.1186/s40668-017-0022-0`. arXiv: `1612.06251 [gr-qc]`.

Guermond, Jean-Luc et al. (2011). Entropy viscosity method for nonlinear conservation laws, *Journal of Computational Physics* **230**, no. 11. Special issue High Order Methods for {CFD} Problems, pp. 4248 –4267. ISSN: 0021-9991. DOI: `http://dx.doi.org/10.1016/j.jcp.2010.11.043`.

Haas, Roland et al. (2016). Simulations of inspiraling and merging double neutron stars using the Spectral Einstein Code, *Phys. Rev. D* **93**, no. 12, p. 124062. DOI: `10.1103/PhysRevD.93.124062`. arXiv: `1604.00782 [gr-qc]`.

Harten, A. et al. (1983). On upstream differencing and Godunov-type schemes for hyperbolic conservation laws, *SIAM Rev.* **25**, pp. 35–61.

Hesthaven, Jan S. et al. (2007). *Nodal Discontinuous Galerkin Methods: Algorithms, Analysis, and Applications*. 1st. Springer Publishing Company, Incorporated. ISBN: 0387720650, 9780387720654.

Hewish, A. et al. (1968). Observation of a rapidly pulsating radio source, *Nature* **217**, pp. 709–713. DOI: `10.1038/217709a0`.

Hild, Stefan et al. (2008). Pushing towards the ET sensitivity using 'conventional' technology, arXiv: `0810.0604 [gr-qc]`.

Hilditch, David et al. (2013). Compact binary evolutions with the Z4c formulation, *Phys. Rev. D* **88**, p. 084057. DOI: `10.1103/PhysRevD.88.084057`. arXiv: `1212.2901 [gr-qc]`.

Hilditch, David et al. (2016). Pseudospectral method for gravitational wave collapse, *Phys. Rev. D* **93**, no. 6, p. 063006. DOI: 10.1103/PhysRevD.93.063006. arXiv: 1504.04732 [gr-qc].

Hinder, Ian et al. (2018). Eccentric binary black hole inspiral-merger-ringdown gravitational waveform model from numerical relativity and post-Newtonian theory, *Phys. Rev. D* **98**, no. 4, p. 044015. DOI: 10.1103/PhysRevD.98.044015. arXiv: 1709.02007 [gr-qc].

Hotokezaka, Kenta et al. (2013b). The mass ejection from the merger of binary neutron stars, *Phys. Rev. D* **87**, p. 024001. DOI: 10.1103/PhysRevD.87.024001. arXiv: 1212.0905 [astro-ph.HE].

Hotokezaka, Kenta et al. (2013a). Remnant massive neutron stars of binary neutron star mergers: Evolution process and gravitational waveform, *Phys. Rev. D* **88**, no. 4, p. 044026. DOI: 10.1103/PhysRevD.88.044026. arXiv: 1307.5888 [astro-ph.HE].

IndIGO. LIGO India. http://www.gw-indigo.org/.

Jiang, G. (June 1996). Efficient Implementation of Weighted ENO Schemes, *J. Comp. Phys.* **126**, pp. 202–228. DOI: 10.1006/jcph.1996.0130.

KAGRA. Large-scale Cryogenic Gravitational Wave Telescope Project. http://gwcenter.icrr.u-tokyo.ac.jp/en/.

Kastaun, Wolfgang et al. (2015). Properties of hypermassive neutron stars formed in mergers of spinning binaries, *Phys. Rev. D* **91**, no. 6, p. 064027. DOI: 10.1103/PhysRevD.91.064027. arXiv: 1411.7975 [gr-qc].

Kastaun, Wolfgang et al. (2017). Structure of Stable Binary Neutron Star Merger Remnants: Role of Initial Spin, *Phys. Rev. D* **96**, no. 4, p. 043019. DOI: 10.1103/PhysRevD.96.043019. arXiv: 1612.03671 [astro-ph.HE].

Kidder, Lawrence E. et al. (1993). Spin effects in the inspiral of coalescing compact binaries, *Phys. Rev. D* **47**, pp. 4183–4187. DOI: 10.1103/PhysRevD.47.R4183. arXiv: gr-qc/9211025 [gr-qc].

Kidder, Lawrence et al. (2000). Black hole evolution by spectral methods, *Physical Review D* **62**, no. 8. ISSN: 1089-4918. DOI: 10.1103/physrevd.62.084032.

Kidder, Lawrence E. et al. (2001). Extending the lifetime of 3-D black hole computations with a new hyperbolic system of evolution equations, *Phys. Rev.* **D64**, p. 064017. DOI: 10.1103/PhysRevD.64.064017. arXiv: gr-qc/0105031 [gr-qc].

Kidder, Lawrence E. et al. (2017). SpECTRE: A Task-based Discontinuous Galerkin Code for Relativistic Astrophysics, *J. Comput. Phys.* **335**, pp. 84–114. DOI: `10.1016/j.jcp.2016.12.059`. arXiv: `1609.00098 [astro-ph.HE]`.

Kiziltan, Bülent et al. (2013). The Neutron Star Mass Distribution, *Astrophys. J.* **778**, p. 66. DOI: `10.1088/0004-637X/778/1/66`. arXiv: `1309.6635 [astro-ph.SR]`.

Kokkotas, Kostas D. et al. (1995). Tidal and tidal resonant effects in coalescing binaries, *Mon. Not. R. Astron. Soc.* **275**, p. 301. DOI: `10.1093/mnras/275.2.301`. arXiv: `gr-qc/9502034 [gr-qc]`.

Kopriva, David (Mar. 2006). Metric Identities and the Discontinuous Spectral Element Method on Curvilinear Meshes, *J. Sci. Comput.* **26**, pp. 301–327. DOI: `10.1007/s10915-005-9070-8`.

— (2009). *Implementing Spectral Methods for Partial Differential Equations*. Springer, Dordrecht. ISBN: 978-90-481-2261-5. DOI: `10.1007/978-90-481-2261-5`.

Kowalska, I. et al. (2011). The eccentricity distribution of compact binaries, *Astron. Astrophys.* **527**, A70. DOI: `10.1051/0004-6361/201015777`. arXiv: `1010.0511 [astro-ph.CO]`.

Krisher, T. P. (1993). Parametrized post-Newtonian gravitational redshift, *Phys. Rev. D* **48**, pp. 4639–4644. DOI: `10.1103/PhysRevD.48.4639`.

Lattimer, James M. (2012). The nuclear equation of state and neutron star masses, *Ann. Rev. Nucl. Part. Sci.* **62**, pp. 485–515. DOI: `10.1146/annurev-nucl-102711-095018`. arXiv: `1305.3510 [nucl-th]`.

Liang, E. P. T. (Jan. 1977). Relativistic simple waves - Shock damping and entropy production, *Astrophys. J.* **211**, pp. 361–376. DOI: `10.1086/154942`.

LIGO. Laser Interferometer Gravitational Wave Observatory. `http://www.ligo.caltech.edu/`.

Lioutas, Georgios et al. (2018). Universal and approximate relations for the gravitational wave damping timescale of f-modes in neutron stars, *Gen. Relativ. Gravit.* **50**, no. 1, p. 12. DOI: `10.1007/s10714-017-2331-7`. arXiv: `1709.10067 [gr-qc]`.

Liu, Yuk Tung et al. (2008). General relativistic simulations of magnetized binary neutron star mergers, *Phys. Rev. D* **78**, p. 024012. DOI: `10.1103/PhysRevD.78.024012`. arXiv: `0803.4193 [astro-ph]`.

Gourgoulhon, Eric et al. LORENE code. `http://www.lorene.obspm.fr/`.

Lorimer, D. R. (2008). Binary and Millisecond Pulsars, *Living Rev. Rel.* **11**, p. 8. arXiv: `0811.0762 [astro-ph]`.

Metzger, Brian D. (2017). Kilonovae, *Living Rev. Rel.* **20**, p. 3. DOI: `10.1007/s41114-017-0006-z`. arXiv: `1610.09381 [astro-ph.HE]`.

Mignone, A. et al. (2010). High-order conservative finite difference GLM-MHD schemes for cell-centered MHD, *J.Comput.Phys.* **229**, pp. 5896–5920. DOI: `10.1016/j.jcp.2010.04.013`. arXiv: `1001.2832 [astro-ph.HE]`.

Misner, Charles W. et al. (1973). *Gravitation*. San Francisco: W. H. Freeman and Company.

Moldenhauer, Niclas et al. (2014). Initial data for binary neutron stars with adjustable eccentricity, *Phys. Rev. D* **90**, no. 8, p. 084043. DOI: `10.1103/PhysRevD.90.084043`. arXiv: `1408.4136 [gr-qc]`.

Abbott, B. P. et al. (2017b). Gravitational Waves and Gamma-Rays from a Binary Neutron Star Merger: GW170817 and GRB 170817A, *Astrophys. J. Lett.* **848**, no. 2, p. L13. DOI: `10.3847/2041-8213/aa920c`. arXiv: `1710.05834 [astro-ph.HE]`.

Montgomery, Colin et al. (2009). Michell, Laplace and the origin of the black hole concept, *Journal of Astronomical History and Heritage* **12**, no. 2, pp. 90–96.

Mora, Thierry et al. (2004). A PostNewtonian diagnostic of quasiequilibrium binary configurations of compact objects, *Phys. Rev. D* **69**. **71**, 129901(E) (2005), p. 104021. DOI: `10.1103/PhysRevD.71.129901,10.1103/PhysRevD.69.104021`. arXiv: `gr-qc/0312082 [gr-qc]`.

Morsink, Sharon M. et al. (1999). Relativistic Precession around Rotating Neutron Stars: Effects Due to Frame Dragging and Stellar Oblateness, *The Astrophysical Journal* **513**, no. 2, pp. 827–844. DOI: `10.1086/306876`.

Most, Elias R. et al. (2019). Impact of high spins on the ejection of mass in GW170817, *Astrophys. J.* **884**, p. 40. DOI: `10.3847/1538-4357/ab3ebb`. arXiv: `1904.04220 [astro-ph.HE]`.

Nakamura, T. et al. (1987). General Relativistic Collapse to Black Holes and Gravitational Waves from Black Holes, *Prog. Theor. Phys. Suppl.* **90**, pp. 1–218.

Oppenheimer, J. R. et al. (1939). On Massive neutron cores, *Phys. Rev.* **55**, pp. 374–381.

Parisi, Alessandro et al. (2018). Gravitational waves from neutron star excitations in a binary inspiral, *Phys. Rev. D* **97**, no. 4, p. 043015. DOI: `10.1103/PhysRevD.97.043015`. arXiv: `1705.04751 [gr-qc]`.

Peters, P. C. (1964). Gravitational Radiation and the Motion of Two Point Masses, *Phys. Rev.* **136**, B1224–B1232. DOI: `10.1103/PhysRev.136.B1224`.

Piotrowska, Joanna et al. (2019). Spectral methods in the presence of discontinuities, *Journal of Computational Physics* **390**, pp. 527 –547. ISSN: 0021-9991. DOI: `https://doi.org/10.1016/j.jcp.2019.03.048`.

Pretorius, Frans (2005). Evolution of binary black hole spacetimes, *Phys. Rev. Lett.* **95**, p. 121101. DOI: `10.1103/PhysRevLett.95.121101`. arXiv: `gr-qc/0507014`.

Punturo, M. et al. (2010). The Einstein Telescope: A third-generation gravitational wave observatory, *Classical Quantum Gravity* **27**, p. 194002. DOI: `10.1088/0264-9381/27/19/194002`.

Radice, David et al. (2012). THC: a new high-order finite-difference high-resolution shock-capturing code for special-relativistic hydrodynamics, arXiv: `1206.6502 [astro-ph.IM]`.

Radice, David et al. (2014). High-Order Fully General-Relativistic Hydrodynamics: new Approaches and Tests, *Class.Quant.Grav.* **31**, p. 075012. DOI: `10.1088/0264-9381/31/7/075012`. arXiv: `1312.5004 [gr-qc]`.

Radice, David et al. (2016). Dynamical Mass Ejection from Binary Neutron Star Mergers, *Mon. Not. R. Astron. Soc.* **460**, no. 3, pp. 3255–3271. DOI: `10.1093/mnras/stw1227`. arXiv: `1601.02426 [astro-ph.HE]`.

Radice, David et al. (2017). Probing Extreme-Density Matter with Gravitational Wave Observations of Binary Neutron Star Merger Remnants, *Astrophys. J. Lett.* **842**, no. 2, p. L10. DOI: `10.3847/2041-8213/aa775f`. arXiv: `1612.06429 [astro-ph.HE]`.

Read, Jocelyn S. et al. (2009a). Constraints on a phenomenologically parameterized neutron- star equation of state, *Phys. Rev. D* **79**, p. 124032. DOI: `10.1103/PhysRevD.79.124032`. arXiv: `0812.2163 [astro-ph]`.

Read, Jocelyn S. et al. (2009b). Measuring the neutron star equation of state with gravitational wave observations, *Phys. Rev. D* **79**, p. 124033. DOI: `10.1103/PhysRevD.79.124033`. arXiv: `0901.3258 [gr-qc]`.

Read, Jocelyn S. et al. (2013). Matter effects on binary neutron star waveforms, *Phys. Rev. D* **88**, p. 044042. DOI: `10.1103/PhysRevD.88.044042`. arXiv: `1306.4065 [gr-qc]`.

Reisswig, Christian et al. (2011). Notes on the integration of numerical relativity waveforms, *Classical Quantum Gravity* **28**, p. 195015. DOI: `10.1088/0264-9381/28/19/195015`. arXiv: `1006.1632 [gr-qc]`.

Rezzolla, Luciano et al. (2013). *Relativistic Hydrodynamics*. Oxford: Oxford University Press.

Roe, P. L. (1981). Approximate Riemann solvers, parameter vectors and difference schemes, *J. Comput. Phy.* **43**, p. 357.

Rosswog, Stephan (2013). Astrophysics: Radioactive glow as a smoking gun, *Nature* **500**, no. 7464, pp. 535–536. DOI: `10.1038/500535a`.

— (2015). The multi-messenger picture of compact binary mergers, *Int.J.Mod.Phys.* **D24**, no. 05, p. 1530012. DOI: `10.1142/S0218271815300128`. arXiv: `1501.02081 [astro-ph.HE]`.

Schutz, Bernard F. (1985). *A First Course In General Relativity*. Cambridge, UK: Cambridge Univ. Pr.

Schwarzschild, Karl (1916). On the gravitational field of a mass point according to Einstein's theory, *Sitzungsber. Preuss. Akad. Wiss. Berlin (Math. Phys.)* **1916**, pp. 189–196. arXiv: `physics/9905030 [physics]`.

Shibata, M. et al. (1995). Evolution of three-dimensional gravitational waves: Harmonic slicing case, *Phys. Rev. D* **52**, pp. 5428–5444. DOI: `10.1103/PhysRevD.52.5428`.

Shibata, Masaru (1999). Fully general relativistic simulation of coalescing binary neutron stars: Preparatory tests, *Phys. Rev. D* **60**, p. 104052. DOI: `10.1103/PhysRevD.60.104052`. arXiv: `gr-qc/9908027`.

Shibata, Masaru et al. (2000). Simulation of merging binary neutron stars in full general relativity: $\Gamma = 2$ case, *Phys. Rev. D* **61**, p. 064001. DOI: `10.1103/PhysRevD.61.064001`. arXiv: `gr-qc/9911058`.

Shibata, Masaru et al. (2005). Merger of binary neutron stars with realistic equations of state in full general relativity, *Phys. Rev. D* **71**, p. 084021. DOI: `10.1103/PhysRevD.71.084021`. arXiv: `gr-qc/0503119`.

Shibata, Masaru (2016). *Numerical Relativity*. Singapore: World Scientific.

Shibata, Masaru et al. (2017). Modeling GW170817 based on numerical relativity and its implications, *Phys. Rev. D* **96**, no. 12, p. 123012. DOI: `10.1103/PhysRevD.96.123012`. arXiv: `1710.07579 [astro-ph.HE]`.

Shipman, H. L. (1975). The Implausible History of Triple Star Models for Cygnus X-1: Evidence for a Black Hole, *Astrophys. Lett.* **16**, p. 9.

Shu, C.W. et al. (1989). Efficient Implementation of Essentially Non-Oscillatory Shock-Capturing Schemes, II, *J. Comput. Phys.* **83**, pp. 32–78.

Steinhoff, Jan et al. (2016). Dynamical Tides in General Relativity: Effective Action and Effective-One-Body Hamiltonian, *Phys. Rev. D* **94**, no. 10, p. 104028. DOI: `10.1103/PhysRevD.94.104028`. arXiv: `1608.01907 [gr-qc]`.

Stephani, Hans et al. (2003). *Exact solutions of Einstein's field equations*. Cambridge Monographs on Mathematical Physics. Cambridge: Cambridge Univ. Press. ISBN: 9780521467025, 0521467020, 9780511059179. DOI: `10.1017/CBO9780511535185`.

Stephens, Branson C. et al. (2011). Eccentric Black Hole-Neutron Star Mergers, *Astrophys. J. Lett.* **737**, p. L5. DOI: `10.1088/2041-8205/737/1/L5`. arXiv: `1105.3175 [astro-ph.HE]`.

Sundqvist, Hilding et al. (1970). A simple finite-difference grid with non-constant intervals, *Tellus* **22**, no. 1, pp. 26–31. DOI: `10.3402/tellusa.v22i1.10155`.

Suresh, A. (Sept. 1997). Accurate Monotonicity-Preserving Schemes with Runge Kutta Time Stepping, *J. Comp. Phys.* **136**, pp. 83–99. DOI: `10.1006/jcph.1997.5745`.

Szilagyi, Bela et al. (2009). Simulations of Binary Black Hole Mergers Using Spectral Methods, *Phys. Rev. D* **80**, p. 124010. DOI: `10.1103/PhysRevD.80.124010`. arXiv: `0909.3557 [gr-qc]`.

Tacik, Nick et al. (2015). Binary Neutron Stars with Arbitrary Spins in Numerical Relativity, *Phys. Rev. D* **92**, no. 12. **94**, 049903(E) (2016), p. 124012. DOI: `10.1103/PhysRevD.94.049903,10.1103/PhysRevD.92.124012`. arXiv: `1508.06986 [gr-qc]`.

Tadmor, Eitan (2007). Filters, mollifiers and the computation of the Gibbs phenomenon, *Acta Numerica* **16**, pp. 305378. DOI: `10.1017/S0962492906320016`.

Takami, Kentaro et al. (2015). Spectral properties of the post-merger gravitational-wave signal from binary neutron stars, *Phys. Rev. D* **91**, no. 6, p. 064001. DOI: `10.1103/PhysRevD.91.064001`. arXiv: `1412.3240 [gr-qc]`.

Taracchini, Andrea et al. (2014). Effective-one-body model for black-hole binaries with generic mass ratios and spins, *Phys. Rev. D* **89**, no. 6, p. 061502. DOI: `10.1103/PhysRevD.89.061502`. arXiv: `1311.2544 [gr-qc]`.

Bernuzzi, S. et al. IHES EOB code. `https://eob.ihes.fr/`.

Teukolsky, Saul A. (2015). Short note on the mass matrix for GaussLobatto grid points, *Journal of Computational Physics* **283**, pp. 408413. ISSN: 0021-9991. DOI: `10.1016/j.jcp.2014.12.012`.

Abbott, Benjamin P. et al. (2017f). GW170817: Observation of Gravitational Waves from a Binary Neutron Star Inspiral, *Phys. Rev. Lett.* **119**, no. 16, p. 161101. DOI: `10.1103/PhysRevLett.119.161101`. arXiv: `1710.05832 [gr-qc]`.

Thierfelder, Marcus et al. (2011). Numerical relativity simulations of binary neutron stars, *Phys. Rev. D* **84**, p. 044012. DOI: `10.1103/PhysRevD.84.044012`. arXiv: `1104.4751 [gr-qc]`.

Thompson, Christopher et al. (1995). The Soft gamma repeaters as very strongly magnetized neutron stars - 1. Radiative mechanism for outbursts, *Mon. Not. R. Astron. Soc.* **275**, pp. 255–300.

Thornburg, Jonathan (2007). Event and apparent horizon finders for 3+1 numerical relativity, *Living Rev. Rel.* **10**, p. 3. arXiv: `gr-qc/0512169 [gr-qc]`.

Tichy, Wolfgang (2006). Black hole evolution with the BSSN system by pseudo-spectral methods, *Phys. Rev. D* **74**, p. 084005. DOI: `10.1103/PhysRevD.74.084005`. arXiv: `gr-qc/0609087 [gr-qc]`.

— (2009a). A New numerical method to construct binary neutron star initial data, *Classical Quantum Gravity* **26**, p. 175018. DOI: `10.1088/0264-9381/26/17/175018`. arXiv: `0908.0620 [gr-qc]`.

— (2009b). Long term black hole evolution with the BSSN system by pseudo-spectral methods, *Phys. Rev. D* **80**, p. 104034. DOI: `10.1103/PhysRevD.80.104034`. arXiv: `0911.0973 [gr-qc]`.

— (2011). Initial data for binary neutron stars with arbitrary spins, *Phys. Rev. D* **84**, p. 024041. DOI: `10.1103/PhysRevD.84.024041`. arXiv: `1107.1440 [gr-qc]`.

— (2012). Constructing quasi-equilibrium initial data for binary neutron stars with arbitrary spins, *Phys. Rev. D* **86**, p. 064024. DOI: `10.1103/PhysRevD.86.064024`. arXiv: `1209.5336 [gr-qc]`.

Tolman, Richard C. (1939). Static solutions of Einstein's field equations for spheres of fluid, *Phys. Rev.* **55**, pp. 364–373.

Troja, Eleonora et al. (2010). Precursors of short gamma-ray bursts, *Astrophys. J.* **723**, pp. 1711–1717. DOI: `10.1088/0004-637X/723/2/1711`. arXiv: `1009.1385 [astro-ph.HE]`.

Tsang, David et al. (2012). Resonant Shattering of Neutron Star Crusts, *Phys. Rev. Lett.* **108**, p. 011102. DOI: `10.1103/PhysRevLett.108.011102`. arXiv: `1110.0467 [astro-ph.HE]`.

Tsokaros, Antonios et al. (2019). Effect of spin on the inspiral of binary neutron stars, *Phys. Rev. D* **100**, no. 2, p. 024061. DOI: `10.1103/PhysRevD.100.024061`. arXiv: `1906.00011 [gr-qc]`.

Turner, M. (Sept. 1977). Tidal generation of gravitational waves from orbiting Newtonian stars. I - General formalism, *Astrophys. J.* **216**, pp. 914–929. DOI: 10.1086/155536.

Meter, James R. van et al. (2006). How to move a black hole without excision: gauge conditions for the numerical evolution of a moving puncture, *Phys. Rev. D* **73**, p. 124011. DOI: 10.1103/PhysRevD.73.124011. arXiv: gr-qc/0605030.

VIRGO. Virgo/EGO, European Gravitational Observatory. http://www.ego-gw.it/.

Wald, Robert M. (1984). *General relativity*. Chicago: The University of Chicago Press. ISBN: 0-226-87032-4 (hardcover), 0-226-87033-2 (paperback).

Wheeler, J. A. (1964). "Geometrodynamics and the issue of final state", *Relativité, Groupes et Topologie: Proceedings, Ecole d'été de Physique Théorique, Session XIII, Les Houches, France, Jul 1 - Aug 24, 1963*, pp. 317–522.

Wilson, J.R. et al. (1995). Instabilities in Close Neutron Star Binaries, *Phys. Rev. Lett.* **75**, pp. 4161–4164. DOI: 10.1103/PhysRevLett.75.4161.

Wilson, J.R. et al. (1996). Relativistic numerical model for close neutron star binaries, *Phys. Rev. D* **54**, pp. 1317–1331. DOI: 10.1103/PhysRevD.54.1317. arXiv: gr-qc/9601017 [gr-qc].

Yamamoto, Tetsuro et al. (2008). Simulating coalescing compact binaries by a new code SACRA, *Phys. Rev. D* **78**, p. 064054. DOI: 10.1103/PhysRevD.78.064054. arXiv: 0806.4007 [gr-qc].

Yang, Huan et al. (2018). Evolution of Highly Eccentric Binary Neutron Stars Including Tidal Effects, *Phys. Rev. D* **98**, no. 4, p. 044007. DOI: 10.1103/PhysRevD.98.044007. arXiv: 1806.00158 [gr-qc].

York, James W. (1979). "Kinematics and Dynamics of General Relativity", *Sources of gravitational radiation*. Ed. by Larry L. Smarr. Cambridge, UK: Cambridge University Press, pp. 83–126. ISBN: 0-521-22778-X.

York Jr., James W. (1999). Conformal 'thin sandwich' data for the initial-value problem, *Phys. Rev. Lett.* **82**, pp. 1350–1353. DOI: 10.1103/PhysRevLett.82.1350. arXiv: gr-qc/9810051 [gr-qc].

Zhao, Jian et al. (2013). RungeKutta discontinuous Galerkin methods with WENO limiter for the special relativistic hydrodynamics, *Journal of Computational Physics* **242**, pp. 138 –168. ISSN: 0021-9991. DOI: https://doi.org/10.1016/j.jcp.2013.02.018.

Zingan, Valentin et al. (2013). Implementation of the entropy viscosity method with the discontinuous Galerkin method, *Computer Methods in Applied Mechanics and Engineering* **253**, pp. 479 –490. ISSN: 0045-7825. DOI: `https://doi.org/10.1016/j.cma.2012.08.018`.

Zink, Burkhard et al. (2010). On the frequency band of the f-mode CFS instability, *Phys. Rev. D* **81**, p. 084055. DOI: `10.1103/PhysRevD.81.084055`. arXiv: `1003.0779 [astro-ph.SR]`.

Publications

Regular Articles

- D. Keitel and others, *The most powerful astrophysical events: gravitational-wave peak luminosity of binary black holes as predicted by numerical relativity*, Phys. Rev. D (96) (2017) 024006, arXiv: 1612.09566 [gr-qc].
- T. Dietrich, D. Radice, S. Bernuzzi, F. Zappa, A. Perego, B. Brügmann, S. V. Chaurasia, R. Dudi, W. Tichy, M. Ujevic, *CoRe database of binary neutron star merger waveforms*, Class. Quant. Grav.(35) (2018) 24LT01, arXiv: 1806.01625 [gr-qc].
- S. V Chaurasia, T. Dietrich, N. K. Johnson-McDaniel, M. Ujevic W. Tichy and B. Brügmann, *Gravitational waves and mass ejecta from binary neutron star mergers: Effect of large eccentricities*, Phys. Rev. D(98) (2018) 104005, arXiv: 1807.06857 [gr-qc].
- S. V Chaurasia, T. Dietrich, M. Ujevic, K. Hendriks R. Dudi, F. M. Fabbri, W. Tichy and B. Brügmann, *Gravitational waves and mass ejecta from binary neutron star mergers: Effect of spin orientation.*, (2020) arXiv: 2003.11901 [gr-qc].

Proceeding without peer-review

- T. Dietrich, S. Bernuzzi, B. Brügmann, S. V. Charausia, R. Dudi, D. Radice, W. Tichy, M. Ujevic, *Binary Neutron Star Merger Simulations*, in P. Bastian, D. Kranzlmüller, H. Brüchle, M. Brehm (Eds.), High Performance Computing in Science and Engineering - Garching/Munich (2018), ISBN 978-3-9816675-2-3.

Acknowledgements

I am very grateful to my supervisor Prof. Bernd Brügmann for giving me the opportunity to write my doctoral thesis in his group and for supporting me from the start. I am pleased to be a part of his numerical relativity group and the TPI community in Jena.

Any amount of appreciation will fall short in expressing my gratitude for Dr. Tim Dietrich, who from the very beginning has endlessly supported me in my endeavors, be it understanding and using the `BAM` code or clarifying many doubts that came along. I am also grateful of him to go through this thesis and give me his valuable suggestions and corrections. Further, I want to thank Dr. Nathan-Kieran Johnson-McDaniel for his very insightful and indispensable discussions during the eccentric project and for being a careful proof reader. I convey my thanks to Prof. Maximiliano Ujevic Tonino who always carefully went through my `BAM` parameter files and also gave his valuable comments during this thesis work. I am grateful for Prof. Wolfgang Tichy's annual visit to TPI for the `BAM` meetings and the numerous insightful discussions about `BAM`, `SGRID` and the spectral methods.

I am very thankful for my office mates, Reetika Dudi, Dr. Marcus Bugner and Dr. Hannes Rüter who from the very beginning inducted me smoothly into the office culture, be it work related or our amazing sessions of playing 'olaf' card game and table tennis. I cannot thank Reetika Dudi enough for being there from the start when I first came to Germany and who gave me valuable suggestions even outside the office. Our discussions about everything, the delicious Indian food that you cooked and all the celebrations we had together with Shiti, Ritika, Lajwanti and others in Jena will be etched in my memory for the times to come. I am grateful to Francesco M. Fabbri, Francesco Zappa, Matteo, Vseva, Alessandro, Sarp, Max, Sarah, Riccardo and Daniela for all the times we hanged out on different occasions. In particular I want thank Dr. Hannes Rüter and Sarah Renkhoff for clarifying most of the technical doubts about the `bamps` code. I also convey my gratitude to Florian Atteneder and Simon Julian Schreyer for helping me write the 'Zusammenfassung'.

I want convey my appreciation and best wishes to SGI-Deutschland through which I met many admirable people, Shiti, Valeria, Pramit and Deepti to name a few, who have supported me in all my struggles from the time I have been in Germany. I am indebted to Valeria Soracco who has always been there for me and took care of me like a mother in all my struggles in Jena.

I am beholden to my family and friends who could not be here physically, nonetheless without whose support none of this would have been possible. I thank all my parents, my siblings and my elders who guided me and supported me through all the years of school, studies and the Ph.D. You all have been the source of everything in my life.

Additional Material

Talks

- *Neutron Stars In Numerical Relativity* (2019) (invited), Department of Astronomy, Stockholm University
- DPG-München (2019), *Eccentric Binary Neutron Stars In Numerical Relativity*, Munich
- PHAROS meeting (2019) (Poster Presentation), Theoretical Physics Institute, University of Jena
- SuperMUC Status and Results Workshop (2018), *Numerical relativity simulations of generic neutron star binaries*, Leibniz-Rechenzentrum, Garching, Munich
- *Neutron Stars In Numerical Relativity: Updates from the Jena group* (2018) (invited), ICTS-Bangalore
- The Physics of Extreme-Gravity Stars Workshop (2017), *Eccentric Binary Neutron Star Mergers*, NORDITA, Stockholm University

Research Visits

- *Introduction to Parallel Programming with MPI and OpenMP* (2018), Jülich Supercomputing Centre, Germany
- Albert-Einstein-Institute (2017), Potsdam, Germany

Curriculum Vitae

Name	Swami Vivekanandji
Surname	Chaurasia
Address	Docentbacken 1B / 1103 11418 Stockholm Sweden
Email	swami.chaurasia@gmail.com
ORCID ID	0000-0003-1312-6924
Telephone	+49 1516 3955691
Date of Birth	20th December 1991
Nationality	Indian

Education

2016-2020	Doctoral Student - Theoretical Physics Institute, University of Jena
2011-2016	Integrated MSc in Physics - Centre For Excellence In Basic Sciences, Mumbai CGPA - 8.23

Professional Experience

2020-	Postdoc in Department of Astronomy, Computational High-Energy Astrophysics, Stockholm University
2016-2020	Research Assistant-Theoretical Physics Institute, University of Jena

Scholarships/Grants

2016-2018	DFG Research Training Group 1523/2 “Quantum and Gravitational Fields”
2014	S. N. Bhatt Memorial Excellence Fellowship, ICTS- Bangalore.
2011-2016	INSPIRE Fellowship of the Department of Science and Technology (DST), Government of India

Teaching

2018-2019	WS: Machine Learning Lab Sessions (Python), SS: Computational Physics Lab Sessions (C)
2017-2018	WS: General Relativity Exercise Sessions, SS: Computational Physics Lab Sessions (C)
2016-2017	WS: General Relativity Exercise Sessions, SS: Computational Physics Lab Sessions (C)

WS: Winter Semester; SS: Summer Semester

January 29, 2020, Jena

Unterschrift

Zusammenfassung

In dieser Arbeit untersuchten wir Neutrone in Binärsystemen, die sich auf stark exzentrischen sowie präzedierenden Orbits bewegen. Im Gegensatz zu früheren Studien nutzten wir für unsere Simulationen Anfangsdaten, die sowohl die Gleichungen der allgemeinen Relativitätstheorie als auch der allgemein relativistischen Hydrodynamik (GRHD) im Gleichgewicht erfüllen. Diese konsistenten Anfangswertdaten erlauben eine detaillierte Untersuchung astrophysikalischen Prozesse, die während der Kollision der Sterne stattfinden. Zusätzlich haben wir, mithilfe des `bamps` Programms, die diskontinuierliche Galerkin Methoden zur Lösung der GRHD in Neutronensternsystemen untersucht.

Ein zentraler Punkt der Arbeit war die Simulation und Studie von binären Neutronensternsysteme auf hoch exzentrischen Bahnen für nicht rotierende und rotierende Neutronensterne. Die verwendeten Anfangsdaten wurden mit dem `SGRID` Programm berechnet. In Abhängigkeit der Exzentrizität wurde die Dynamik während der Fusion untersucht. Es wurde festgestellt, dass die Anzahl der Bahnen signifikant variiert und somit von den gesetzten Anfangswerten abhängig ist. Darüber hinaus haben unsere Simulationen gezeigt, dass die Exzentrizität keinen weiteren Effekt auf die restlichen Eigenschaften des Kollisionsprozesses besitzt.

Insgesamt wird erwartet, dass bei einer Kollision zweier Neutronensterne schätzungsweise $\sim \mathcal{O}(10^{-2})\ M_\odot$ an ungebundener Materie ausgestoSSen wird. Für die betrachteten Fälle mit weicher und steifer Zustandsgleichung (EOS) entspricht dies einer Zunahme von ungefähr einer GröSSenordnung im Vergleich zu quasikreisförmigen Simulationen. Die Simulationen zeigen weiterhin, dass die Gezeitenschweifauswürfe aufgrund der Umverteilung des Drehimpulses zu gröSSeren Materieauswürfen führen als bei MaterieausstöSSe durch Schocks. AuSSerdem wurde ungebundene Materie $\sim \mathcal{O}(10^{-3}) - \mathcal{O}(10^{-2})\ M_\odot$ mit Geschwindigkeiten von $\sim 6 - 15\%$ der Lichtgeschwindigkeit leicht relativistisch und leicht isotrop ausgestoSSen. Im Gegensatz zu nicht-exzentrischen Fusionen konnte berechnet werden, dass ungebundene, neutronenreiche Materie der GröSSenordnung $\sim \mathcal{O}(10^{-4}) - \mathcal{O}(10^{-3})\ M_\odot$

noch vor der Fusion ausgestoSSen werden kann. Dies würde prinzipiell die Beobachtung von elektromagnetischer Strahlung vor der Kollison ermöglichen.

Diese gemessenen MaterieausstöSSe können elektromagnetische Signale hervorrufen, welche mit den Ergebnissen von quasi-kreisförmigen, binären Neutronensternen übereinstimmen. Im Allgemeinen wird erwartet, dass die betrachteten Konfigurationen über einen Zeitraum von wenigen Tagen bis hin zu zwei Wochen nach der Kollision zu einer Kilonovae mit Helligkeiten zwischen $10^{39} - 10^{42}$ erg s^{-1} führen. Die vermutete Radioemission wird nach etwa $t^{\mathrm{radio}}_{\mathrm{peak}} \sim \mathcal{O}(\mathrm{years})$ am stärksten sein, ähnlich wie bei äquivalenten quasi-kreisförmigen Fällen.

Ein charakteristisches Merkmal für binäre Neutronensterne (NS) auf exzentrischen Bahnen ist die Überlagerung von Gravitationswellen mit bestimmten, quasinormalen Moden und dem Gravitationswellensignal, welches durch die Orbitbewegung hervorgerufen wird. Diese quasi-normalen Moden werden durch die zeitveränderlichen Störungen der Sterne während ihrer Periastronpassagen angeregt. Es wurde eine gute Übereinstimmung zwischen den f-Moden in unseren Simulationen für die nicht-rotierenden Sterne und der Abschätzung für äquivalente isolierte NS aus der Störungstheorie gefunden. Das in unseren Simulationen gefundene $(2, 0)$ f-Modensignal wurde vollständig durch die Modenmischung der intrinsischen $(2, \pm 2)$ Moden der Sterne berücksichtigt. Dies ist möglich aufgrund ihrer Verschiebung vom Koordinatenursprung. In unseren Simulationen stieg die in den f-Modenschwingungen gespeicherte Energie mit zunehmender Exzentrizität. Es zeigte sich, dass bei der Verwendung von steifen Zustandsgleichungen, wie z.B. MS1b, im Allgemeinen mehr Energie in den Oszillationen gespeichert wird im Vergleich zu Beispielen mit weichen Zustandsgleichungen. Weiterhin fanden wir, dass die in den Schwingung der Sterne gespeicherte Energie nicht immer monoton mit der Zeit zunimmt. Dies ist insofern zu erwarten, als dass bei einigen Begegnungen die Gezeitenstörung außer Phase mit den schon existierenden Oszillationen ist. Insgesamt können diese Schwingungen $\sim \mathcal{O}(10^{-8}) - \mathcal{O}(10^{-3})\ M_{\odot}$ an Energie speichern, abhängig von der Exzentrizität und der Abfolge der nicht verschmelzenden Begegnungen.

Zusätzlich untersuchten wir Neutronensternsysteme bei der sich die Sterne auf präzedierenden Bahnen bewegen. Um präzedierende Orbits zu erzeugen, wurde die Spinorientierung der Sterne variiert. In einigen Simulationen haben wir eine

Präzession oder ′taumelnde′ Bewegung der gesamten Orbit-Ebene beobachtet. Diese Systeme hatten ihre Spins asymmetrisch zum Drehimpuls des Systems ausgerichtet. Andere Konfigurationen, bei denen die Spins symmetrisch ausgerichtet waren, zeigten eine ′wippende′ Bewegung der Bahnebene, das heißt bei dieser Art von Bewegung schwingte die gesamte Bahnebene während der Evolution in $z-$Richtung.

Der Präzessionskegel des Bahndrehimpulses hatte bei den Konfigurationen mit ′Taumelbewegungen′ den gröSSten Öffnungswinkel, was unsere Resultate bestätigt. Darüber hinaus zeigten solche präzedierenden Simulationen eine deutliche Modulation der (2,1)-Mode des GW-Signals. Für symmetrisch ausgerichteten Systeme wurde keine Präzession des Bahndrehimpulses oder Präzessionseffekte der (2,1)-Mode beobachtet. Abgesehen von der "wackelnden" oder "wippenden" Bewegung waren auch Nutationseffekte zu erkennen. Die Zeitskala dieser Notationseffekte ist im Vergleich zur Zeitskala für die orbitale Präzession kürzer. Die Bewegung der Orbitalebene, das "Wackeln" oder "Wippen", kann aufgrund der Spinausrichtung qualitativ durch den allgemein-relativistischen Frame-Dragging-Effekt oder den Lense-Thirring-Effekt erklärt werden.

Ungebundene Materie mit einer Masse von $\sim \mathcal{O}(10^{-3}) - \mathcal{O}(10^{-2})\ M_\odot$ wurde bei Neutronsternkollisionen auf präzesdierenden Bahnen gemessen. Im Gegensatz zu Systemen mit kreisförmigen Bahnen und mit Neutronensternen gleicher Masse, bei denen ein symmetrischer Auswurf der Materie erwartet wird, konnten in unseren präzedierenden Simulationen assymetrische Materieverteilungen beobachtet werden. Dies ist auf die wackelde und wippende Bewegung des Systems zurückzuführen. Aufgrund der asymmetrische Emission von Materie und der Impulserhaltung wird ein Kick des restlichen Systems erwartet. Zusätzlich zur emittierten Materie spielen Emissionen von Gravitationswellen eine entscheidende Rolle, um die Magnitude und Richtung des Kicks zu bestimmen.

Weiterhin untersuchten wir die diskontinuierliche Galerkin Methode zur Lösung der GRHD im Kontext von spektralen Elementmethoden. Mit reinen diskontinuierlichen Galerkin Methoden konnte für glatte Lösungen die erwartete Konvergenz der N-ten Polynomordnung in einer $hp-$ oder Spektralelementmethode erreicht werden. Sobald sich im System jedoch Diskontinuitäten bildeten, verringerte sich die Genauigkeit und Konvergenzordnung drastisch. Daher kamen wir zu dem Schluss, dass die reine DG-Methode für genaue und stabile numerische Entwicklungen im Zusammenhang mit Neutronsternen, bei denen Schocks und Diskontinuitäten in auftreten können, nicht durchführbar und effizient ist.

Zur Markierung der Regionen mit Diskontinuitäten haben wir einen neuen und robusten Indikator getestet, der auf der Messung der lokalen Entropieerzeugung basiert. Im Vergleich zu konventionellen Indikatoren ist der Entropieindikator vorteilhaft, da er (i) keine Zellmittelwerte aus den benachbarten Gittern benötigt, dies verringert die Datenkommunikation in parallelen Codes und (ii) zellmittelwertbasierte Indikatoren markieren auch die Extrembereiche der Lösungen als kritisch, was bei dem Entropieindikator nicht der Fall ist. Der Indikator wurde bei Shocktube-Problemen in einer und zwei Dimensionen sowie der Simulation von Neutronensternen mit fester Hintergrundmetrik getestet. Diese Tests zeigten, dass der Entropieindikator problematische Regionen markiert. Dies war ein wichtiger Schritt bei der Behandlung der kritischen Regionen für Lösungen mit Diskontinuitäten.

Im Shocktubetest in 1D erprobten wir einen minmod Slope-Limiter und einen WENO3 Limiter, welche die kritischen Regionen bearbeiten konnten, ohne die Diskontinuitäten exakt zu erfassen. Solche Begrenzungsmethoden wurden mit unterschiedlichem Erfolg in astrophysikalischen Simulationen eingesetzt; am natürlichsten jedoch im Rahmen von finiten Differenzen oder finiten Volumen-Methoden. Insgesamt haben HRSC-Methoden Defizite, die die Simulation mit Spektralelementmethoden erschweren. Das bedeutet, dass sich spektrale Methoden der finiten Differenzen und finiten Volumen annähern und aufgrund der Nichtlokalitäten die Kombination von spektralen Methoden mit Limitern zu einer schlechteren Parallelisierung führt. Letzteres setzt die Skalierbarkeit solcher Methoden herab.

In Zukunft ist im Rahmen der Spektralverfahren eine über die herkömmlichen Methoden zur Begrenzung diskontinuierlicher Lösungen durch Filterung und HRSC-Methoden hinausgehende Detailuntersuchung erforderlich. Einige Techniken, welche getestet werden könnten, sind die Methode der entropieresidualen, gewichteten, künstlichen Viskosität, ‘Reprojection und ‘Mollification.

Selbstständigkeitserklärung

Ich erkläre hiermit, dass ich die vorliegende Arbeit selbständig, ohne unzulässige Hilfe Dritter und ohne Benutzung anderer als der angegebenen Hilfsmittel und Literatur angefertigt habe. Die aus anderen Quellen direkt oder indirekt übernommenen Daten und Konzepte sind unter Angabe der Quelle gekennzeichnet.

Bei der Auswahl und Auswertung dieser Arbeit haben mir die nachstehend aufgeführten Personen in beratender Weise unentgeltlich geholfen:

- Prof. Bernd Brügmann
- Dr. Tim Dietrich
- Dr. Nathan K. Johnson-McDaniel
- Prof. Maximiliano Ujevic
- Prof. Wolfgang Tichy
- Dr. Marcus Bugner
- M.Sc. Reetika Dudi
- Dr. Hannes Rüter

In Bereichen bei denen auf Arbeit anderer zurückgegriffen wurde, ist dies ausdrücklich in der Arbeit erwähnt. Weitere Personen waren an der inhaltlich-materiellen Erstellung der vorliegenden Arbeit nicht beteiligt. Insbesondere habe ich hierfür nicht die entgeltliche Hilfe von Vermittlungs- bzw. Beratungsdiensten (Promotionsberater oder andere Personen) in Anspruch genommen. Niemand hat von mir unmittelbar oder mittelbar geldwerte Leistungen für Arbeiten erhalten, die im Zusammenhang mit dem Inhalt der vorgelegten Dissertation stehen. Die Arbeit wurde bisher weder im In- noch im Ausland in gleicher oder ähnlicher Form einer anderen Prüfungsbehörde vorgelegt.

Ich versichere ehrenwörtlich, dass ich nach bestem Wissen die reine Wahrheit gesagt und nichts verschwiegen habe.

January 29, 2020, Jena

Unterschrift